TECHNISCHE UNIVERSITÄT WIEN

UNIVERSITÉ CÔTE D'AZUR

DIPLOMARBEIT

DIPLOMA THESIS

Fisher Information Flow in Wave Scattering

ausgeführt am

executed at

Institut für Theoretische Physik
Technische Universität Wien

&

Institut de Physique de Nice
Université Côte d'Azur

unter der Anleitung von

supervised by

Dipl.-Ing. Jakob Hüpfl BSc
Univ. Prof. Dr. Ulrich Kuhl
Dipl.-Ing. Lukas M. Rachbauer BSc
Univ. Prof. Dr.techn. Stefan Rotter

Autor

Author

Felix Russo
Matrikelnummer 01525563
felix.russo@gmx.at

Vienna, September 12, 2022 [redacted] [redacted]

Felix Russo Stefan Rotter

Abstract

The information-theoretical concept of Fisher information has recently delivered promising results when applied to coherent scattering measurements. Its most remarkable feature is that it allows the identification of the optimal wavefront for probing any parameter that is hidden within an arbitrary complex scattering medium.

To understand Fisher information in wave scattering on a more fundamental level, we introduce a quantity that describes its behavior locally within the scattering medium: the Fisher information flow. The latter constitutes an information flux density that complements the widely-used energy flux density commonly known as the Poynting vector.

In this work, we investigate the Fisher information flow and the corresponding source term for stationary scalar waves. We demonstrate the properties of these novel quantities using numerical simulations, thereby gaining an intuition for the information-transport characteristics of electromagnetic waves. Moreover, we measure the Fisher information flow using microwave technology to show that the latter is not just a theoretical concept but plays a vital role in practical applications.

Contents

1. Introduction

Since the Digital Revolution, information has become one of the most potent resources of humanity. We store vast amounts of it on servers, transmit it to peers worldwide via the internet, and pay with it for supposedly free web services. However, despite the ubiquity of information in our lives, we are still far from exploiting its full potential.

In the early 20th century, researchers started to investigate information quantitatively, aiming to understand how to transmit, extract, and utilize the latter optimally. Their work marked the birth hour of information theory, a field whose findings influenced numerous other disciplines, including computer science, statistics, and the physical sciences. Just recently, scientists achieved promising results by introducing the concept of Fisher information into the field of scattering metrology [1, 2]. They showed that the amount of information an electromagnetic wave can extract from a complex scattering system is determined by the so-called Fisher information operator, which one can compute from far-field measurements. Moreover, they demonstrated that the optimal probing wavefront corresponds to the maximum eigenstate of the Fisher information operator. This discovery gives rise to many possible applications ranging from the detection of defects in nanofabricated samples to biomedical imaging [3–6].

While past research identified the amount of information associated with a probe state, it remained unclear how this information behaves within the scattering system. In this work, we extend the information-theoretical toolbox for scattering metrology by introducing the Fisher information flow, i.e., a vectorial measure of how information travels with an electromagnetic wave at a given position. This new quantity provides insights into the local behavior of information, thus enabling us to gain a deeper understanding of its properties.

First, in Ch. 2, we discuss Fisher information in estimation theory and show how one can apply this concept to coherent scattering measurements. Furthermore, we introduce the Fisher information flow for stationary scalar waves and present how to control the spatial structure of the latter by tuning the incoming state. Next, in Ch. 3, we validate the results from the previous chapter by performing numerical simulations of electromagnetic waves in a 2D slab geometry. Then, in Ch. 4, we discuss the measurement of the Fisher information flow in a quasi-2D rectangular waveguide and compare the results to numerically simulated data. Finally, in Ch. 5, we summarize and conclude.

2. Theory

2.1. Fisher Information in Classical Estimation Theory

The aim of estimation theory is to determine the value of a parameter, which we call θ following the standard notation. We have access to θ via samples that are drawn from a conditional probability distribution $p(X|\theta)$, i.e., the probability distribution of a random variable X for a given value of θ. To quantify how much information a sample contains, we can use the concept of Fisher information, which we introduce in this section following Refs. [7–10]. The definition of Fisher information reads

$$F(\theta) \coloneqq \mathrm{Var}\left[\partial_\theta \ln(p(X|\theta))\right]. \tag{2.1}$$

We require some regularity conditions:

1. $\partial_\theta p(X|\theta)$ exists almost everywhere, i.e., it may only not exist on a null set that does not depend on θ.
2. $\int T(X)\partial_\theta p(X|\theta) = \partial_\theta \int T(X) p(X|\theta)$.
3. $\mathrm{supp}(p(X|\theta)) = \{X|p(X|\theta) \neq 0\}$ does not depend on θ.

Often, it is helpful to express $F(\theta)$ as an expectation value. Recalling

$$\mathrm{Var}[X] = \mathbb{E}\left[X^2\right] - \mathbb{E}[X]^2,$$

and computing

$$\begin{aligned}
\mathbb{E}\left[\partial_\theta \ln(p(X|\theta))\right] &= \int p(X|\theta)\, \partial_\theta \ln(p(X|\theta)) dX \\
&= \int \partial_\theta p(X|\theta)\, dX \\
&= \partial_\theta \int p(X|\theta)\, dX \\
&= \partial_\theta\, 1 = 0,
\end{aligned} \tag{2.2}$$

we find that

$$F(\theta) = \mathbb{E}\left[(\partial_\theta \ln(p(X|\theta)))^2\right]. \tag{2.3}$$

Note that $[F(\theta)] = [\theta]^{-2}$. To motivate why $F(\theta)$ is a measure of information, we list some of its properties.

- **Non-Negativity**

  From Eq. (2.3) we see that

  $$F(\theta) \geq 0.$$

- **Additivity**

  Consider n independent and identically distributed (i.i.d.) samples from $p(X|\theta)$. We can write the joint probability distribution as $p(X_1, \ldots, X_n|\theta) = \prod_{i=1}^{n} p(X_i|\theta)$. The Fisher information contained in those n samples is then

  $$\begin{aligned} F_n(\theta) &= \mathrm{Var}\left[\partial_\theta \ln\left(\prod_{i=1}^{n} p(X_i|\theta)\right)\right] \\ &= \mathrm{Var}\left[\sum_{i=1}^{n} \partial_\theta \ln(p(X_i|\theta))\right] \\ &\overset{(*)}{=} \sum_{i=1}^{n} \mathrm{Var}\left[\partial_\theta \ln(p(X_i|\theta))\right] \\ &= n\,\mathrm{Var}\left[\partial_\theta \ln(p(X|\theta))\right] \\ &= nF(\theta), \end{aligned}$$

  where we used in $(*)$ that $\mathrm{Var}\left[\sum_i Y_i\right] = \sum_i \mathrm{Var}\left[Y_i\right] + \sum_{i \neq j} \mathrm{Cov}\left[Y_i, Y_j\right]$ and $\mathrm{Cov}\left[Y_i, Y_j\right] = 0$ for independent Y_i and Y_j.

- **Cramér-Rao Inequality**

  The Fisher information gives a lower bound on the variance of any unbiased estimator $\hat{\theta}(X)$, where $X \sim p(X|\theta)$:

  $$\mathrm{Var}\left[\hat{\theta}(X)\right] \geq \frac{1}{F(\theta)}.$$

  Using the additivity of the Fisher information, we obtain the result for an estimator that uses n samples $\hat{\theta}(X_1, ..., X_n)$, where all $X_i \sim p(X|\theta)$:

  $$\mathrm{Var}\left[\hat{\theta}(X_1, ..., X_n)\right] \geq \frac{1}{nF(\theta)}.$$

  For a higher Fisher information $F(\theta)$, the estimator $\hat{\theta}(X_1, ..., X_n)$ fluctuates less around its expectation value, which corresponds to the true value of θ since we assumed that $\hat{\theta}$ is an unbiased estimator. Therefore, fewer samples are necessary to estimate θ with a given precision. Equivalently, one could say that a sample contains more information if $F(\theta)$ is high.

To conclude this section, we prove the Cramér-Rao inequality. We start by using the Cauchy-Schwarz inequality, i.e.,

$$|\,(Y,Z)\,|^2 \leq (Y,Y)\,(Z,Z)\,, \tag{2.4}$$

where Y and Z are elements of the vector space of random variables and $(\cdot,\cdot)$ denotes an inner product. If we now define the latter as[1]

$$(Y,Z) \coloneqq \mathbb{E}\left[YZ\right],$$

we find that

$$\begin{aligned}
\left|\mathrm{Cov}\left[Y,Z\right]\right|^2 &= \left|\mathbb{E}\left[(Y-\mathbb{E}\left[Y\right])(Z-\mathbb{E}\left[Z\right])\right]\right|^2 \\
&\leq \mathbb{E}\left[(Y-\mathbb{E}\left[Y\right])^2\right]\mathbb{E}\left[(Z-\mathbb{E}\left[Z\right])^2\right] \\
&= \mathrm{Var}\left[Y\right]\mathrm{Var}\left[Z\right].
\end{aligned}$$

We set $Y=\hat{\theta}(X)$ and $Z=\partial_\theta \ln(p\,(X|\theta))$. Then, we notice from Eq. (2.2) that $\mathbb{E}\left[Z\right]=0$ and from Eq. (2.1) that $\mathrm{Var}\left[Z\right]=F(\theta)$. Using

$$\begin{aligned}
\mathrm{Cov}\left[Y,Z\right] &= \mathbb{E}\left[(Y-\mathbb{E}\left[Y\right])(Z-\mathbb{E}\left[Z\right])\right] \\
&= \mathbb{E}\left[YZ\right]-\mathbb{E}\left[Y\right]\mathbb{E}\left[Z\right] \\
&= \mathbb{E}\left[YZ\right],
\end{aligned}$$

we obtain the desired bound on the estimator $\hat{\theta}(X)$:

$$\begin{aligned}
\mathrm{Var}\left[\hat{\theta}(X)\right] &= \mathrm{Var}\left[Y\right] \\
&\geq \frac{1}{\mathrm{Var}\left[Z\right]}\left|\mathrm{Cov}\left[Y,Z\right]\right|^2 \\
&= \frac{1}{\mathrm{Var}\left[Z\right]}\left|\mathbb{E}\left[YZ\right]\right|^2 \\
&= \frac{1}{F(\theta)}\left|\int \hat{\theta}(X)\partial_\theta \ln(p\,(X|\theta))p\,(X|\theta)\,dX\right|^2 \\
&= \frac{1}{F(\theta)}\left|\int \hat{\theta}(X)\partial_\theta p\,(X|\theta)\,dX\right|^2 \\
&= \frac{1}{F(\theta)}\left|\partial_\theta \int \hat{\theta}(X)p\,(X|\theta)\,dX\right|^2 \\
&= \frac{1}{F(\theta)}\left|\partial_\theta \mathbb{E}\left[\hat{\theta}\right]\right|^2 \\
&= \frac{1}{F(\theta)},
\end{aligned}$$

where we used that $\hat{\theta}$ is an unbiased estimator, i.e., $\mathbb{E}\left[\hat{\theta}\right]=\theta$, in the last equality.

[1] One can easily check that this definition fulfills all requirements for an inner product, i.e., (conjugate) symmetry, linearity in the first argument, and positive definiteness.

2.2. Quantum Fisher Information

In this section, we discuss Fisher information in the case of quantum metrology, i.e., the estimation of a parameter θ that is enclosed within a quantum system. We require some concepts of linear algebra, functional analysis, and quantum mechanics, which we review briefly in Sec. A of the appendix. With these tools, we can identify the so-called quantum Fisher information by finding an upper bound of the classical Fisher information that does not depend on the choice of the quantum measurement.

2.2.1. Quantum Cramér-Rao Bound

In quantum metrology, one needs to identify a suitable quantum measure $\{\Pi_X\}$ in addition to finding a good (i.e., unbiased and low-variance) classical estimator $\hat{\theta} = \hat{\theta}(X)$. Equivalently, one can say that a quantum estimator is a Hermitian operator that describes a measurement followed by some classical data processing of the measurement outcomes. The quantum Fisher information determines the maximum amount of information about θ that one can extract when choosing the best positive operator-valued measure (POVM) and performing the optimal classical data processing. For the derivation of the quantum Cramér-Rao bound, we will follow Ref. [9], where the results of Ref. [11] are shown in greater detail.

We denote the density operator of the system of interest as ρ_θ. The conditional probability distribution, which depends on the choice of the POVM, can then be written as

$$p\left(X|\theta\right) = \mathrm{Tr}\left[\Pi_X \rho_\theta\right].$$

We introduce the symmetric logarithmic derivative, i.e., a Hermitian operator L_θ that satisfies

$$\frac{1}{2}(L_\theta \rho_\theta + \rho_\theta L_\theta) = \partial_\theta \rho_\theta. \tag{2.5}$$

Then, we can calculate the derivative of the conditional probability,

$$\begin{aligned}
\partial_\theta p\left(X|\theta\right) &= \partial_\theta \,\mathrm{Tr}\left[\Pi_X \rho_\theta\right] \\
&= \mathrm{Tr}\left[\Pi_X \partial_\theta \rho_\theta\right] \\
&= \frac{1}{2}\,\mathrm{Tr}\left[\Pi_X L_\theta \rho_\theta\right] + \frac{1}{2}\,\mathrm{Tr}\left[\Pi_X \rho_\theta L_\theta\right] \\
&= \frac{1}{2}\,\mathrm{Tr}\left[\Pi_X L_\theta \rho_\theta\right] + \frac{1}{2}\,\mathrm{Tr}\left[(\Pi_X \rho_\theta L_\theta)^\dagger\right]^*,
\end{aligned}$$

where we used that

$$\begin{aligned}\mathrm{Tr}\left[O\right] &= \int db\, \langle b|O|b\rangle \\ &= \int db\, \langle O^\dagger b|b\rangle \\ &= \int db (\langle b|O^\dagger b\rangle)^* \\ &= \left(\int db\, \langle b|O^\dagger|b\rangle\right)^* \\ &= \mathrm{Tr}\left[O^\dagger\right]^*.\end{aligned}$$

Since Π_X, ρ_θ, and L_θ are Hermitian, we find

$$\begin{aligned}\partial_\theta p\left(X|\theta\right) &= \frac{1}{2}\mathrm{Tr}\left[\Pi_X L_\theta \rho_\theta\right] + \frac{1}{2}\mathrm{Tr}\left[L_\theta \rho_\theta \Pi_X\right]^* \\ &= \frac{1}{2}\mathrm{Tr}\left[\rho_\theta \Pi_X L_\theta\right] + \frac{1}{2}\mathrm{Tr}\left[\rho_\theta \Pi_X L_\theta\right]^* \\ &= \Re\left\{\mathrm{Tr}\left[\rho_\theta \Pi_X L_\theta\right]\right\},\end{aligned}$$

where we used the cyclic property of the trace and $\Re\{\cdot\}$ denotes the real part. Using Eq. (2.3), we find an expression for the classical Fisher information in the quantum framework:

$$\begin{aligned}F(\theta) &= \mathbb{E}\left[\left(\partial_\theta \ln(p\left(X|\theta\right))\right)^2\right] \\ &= \int dX \frac{1}{p\left(X|\theta\right)}\left(\partial_\theta p\left(X|\theta\right)\right)^2 \\ &= \int dX \frac{\Re\left\{\mathrm{Tr}\left[\rho_\theta \Pi_X L_\theta\right]\right\}^2}{\mathrm{Tr}\left[\rho_\theta \Pi_X\right]}.\end{aligned}$$

Using $\Re\{\cdot\}^2 \leq |\cdot|^2$, we can find an upper bound for the Fisher information:

$$\begin{aligned}F(\theta) &\leq \int dX \frac{\left|\mathrm{Tr}\left[\rho_\theta \Pi_X L_\theta\right]\right|^2}{\mathrm{Tr}\left[\rho_\theta \Pi_X\right]} \\ &= \int dX \frac{\left|\mathrm{Tr}\left[(\sqrt{\rho_\theta}\sqrt{\Pi_X})(\sqrt{\Pi_X} L_\theta \sqrt{\rho_\theta})\right]\right|^2}{\mathrm{Tr}\left[\rho_\theta \Pi_X\right]},\end{aligned}$$

where we used Thm. 1 and the cyclic property of the trace in the last step. If we define a scalar product over the space of operators as[2]

$$(B, A) = \mathrm{Tr}\left[A^\dagger B\right],$$

the Cauchy-Schwarz inequality (see Eq. (2.4)) becomes

$$\left|\mathrm{Tr}\left[A^\dagger B\right]\right|^2 \leq \mathrm{Tr}\left[A^\dagger A\right]\mathrm{Tr}\left[B^\dagger B\right].$$

[2]Again, one can check that this definition of an inner product fulfills all requirements.

We can use this identity to bound $F(\theta)$ further:

$$\begin{aligned}
&\left|\mathrm{Tr}\left[\left(\sqrt{\rho_\theta}\sqrt{\Pi_X}\right)\left(\sqrt{\Pi_X}L_\theta\sqrt{\rho_\theta}\right)\right]\right|^2 \\
&= \left|\mathrm{Tr}\left[\left(\sqrt{\Pi_X}\sqrt{\rho_\theta}\right)^\dagger\left(\sqrt{\Pi_X}L_\theta\sqrt{\rho_\theta}\right)\right]\right|^2 \\
&\leq \mathrm{Tr}\left[\left(\sqrt{\Pi_X}\sqrt{\rho_\theta}\right)^\dagger\sqrt{\Pi_X}\sqrt{\rho_\theta}\right]\mathrm{Tr}\left[\left(\sqrt{\Pi_X}L_\theta\sqrt{\rho_\theta}\right)^\dagger\left(\sqrt{\Pi_X}L_\theta\sqrt{\rho_\theta}\right)\right] \\
&= \mathrm{Tr}\left[\rho_\theta\Pi_X\right]\mathrm{Tr}\left[L_\theta\Pi_X L_\theta\rho_\theta\right],
\end{aligned}$$

and thus

$$F(\theta) \leq \int dX \;\; \mathrm{Tr}\left[L_\theta\Pi_X L_\theta\rho_\theta\right] = \mathrm{Tr}\left[L_\theta^2\rho_\theta\right],$$

where we used the linearity of the trace and $\int \Pi_X dX = \mathbb{1}$. One can rewrite the last expression by remembering the definition of the symmetric logarithmic derivative (see Eq. (2.5)):

$$\begin{aligned}
(L_\theta\rho_\theta + \rho_\theta L_\theta) &= 2\partial_\theta\rho_\theta \\
\implies (L_\theta\rho_\theta + \rho_\theta L_\theta)L_\theta &= 2(\partial_\theta\rho_\theta)L_\theta \\
\implies \mathrm{Tr}\left[L_\theta^2\rho_\theta\right] &= \frac{1}{2}\mathrm{Tr}\left[(L_\theta\rho_\theta + \rho_\theta L_\theta)L_\theta\right] \\
&= \mathrm{Tr}\left[(\partial_\theta\rho_\theta)L_\theta\right].
\end{aligned}$$

We define the quantum Fisher information as

$$H(\theta) \coloneqq \mathrm{Tr}\left[L_\theta^2\rho_\theta\right] = \mathrm{Tr}\left[(\partial_\theta\rho_\theta)L_\theta\right]$$

and see that, unlike $F(\theta)$, it does not depend on the POVM, i.e., it provides an ultimate bound. Moreover, we note that

$$F(\theta) \leq H(\theta),$$

where equality is achieved if we choose an optimal POVM. The quantum Cramér-Rao bound then becomes

$$\mathrm{Var}\left[\hat{\theta}(X)\right] \geq \frac{1}{F(\theta)} \geq \frac{1}{H(\theta)}.$$

One can show that an optimal POVM is given by the set of projectors on the eigenstates of the symmetric logarithmic derivative, see Refs. [9, 11].

Quantum Fisher Information for Pure States

For pure states $|\psi\rangle = |\psi(\theta)\rangle$, we can write the quantum Fisher information in a more convenient form. The density matrix for a pure state is $\rho_\theta = |\psi\rangle\langle\psi|$. Consequently, $\rho_\theta = \rho_\theta^2$, and we find that $\partial_\theta\rho_\theta = (\partial_\theta\rho_\theta)\rho_\theta + \rho_\theta(\partial_\theta\rho_\theta)$. Comparing this

expression to Eq. (2.5), we deduce that $L_\theta = 2\partial_\theta \rho_\theta$ and thus $H(\theta) = 2\,\mathrm{Tr}\,[(\partial_\theta \rho_\theta)^2]$. Then,

$$\begin{aligned} H(\theta) &= 2\,\mathrm{Tr}\left[(\partial_\theta \rho_\theta)^2\right] \\ &= 2\,\mathrm{Tr}\left[(|\partial_\theta\psi\rangle\langle\psi| + |\psi\rangle\langle\partial_\theta\psi|)^2\right] \\ &= 2\,\mathrm{Tr}\left[\,|\partial_\theta\psi\rangle\langle\psi|\partial_\theta\psi\rangle\langle\psi| + |\partial_\theta\psi\rangle\langle\partial_\theta\psi| \right. \\ &\qquad \left. + |\psi\rangle\langle\partial_\theta\psi|\psi\rangle\langle\partial_\theta\psi| + |\psi\rangle\langle\partial_\theta\psi|\partial_\theta\psi\rangle\langle\psi|\,\right] \\ &= 2\left(\langle\psi|\partial_\theta\psi\rangle^2 + 2\langle\partial_\theta\psi|\partial_\theta\psi\rangle + \langle\partial_\theta\psi|\psi\rangle^2\right) \\ &\overset{*}{=} 4\left(\langle\partial_\theta\psi|\partial_\theta\psi\rangle + \langle\partial_\theta\psi|\psi\rangle^2\right) \\ &\overset{*}{=} 4\left(\langle\partial_\theta\psi|\partial_\theta\psi\rangle - |\langle\partial_\theta\psi|\psi\rangle|^2\right), \end{aligned} \tag{2.6}$$

where we used the cyclic property of the trace and $\mathrm{Tr}\,[z] = z$ for any complex scalar z. In the equations that we marked by an asterisk, we used that

$$\begin{aligned} \partial_\theta \langle\psi|\psi\rangle &= 0 \\ \implies \langle\partial_\theta\psi|\psi\rangle &= -\langle\psi|\partial_\theta\psi\rangle \\ &= -\langle\partial_\theta\psi|\psi\rangle^*, \end{aligned}$$

and thus

$$\begin{aligned} \langle\partial_\theta\psi|\psi\rangle^2 &= \langle\psi|\partial_\theta\psi\rangle^2 \\ &= -|\langle\partial_\theta\psi|\psi\rangle|^2. \end{aligned}$$

2.3. Fisher Information in Scattering Measurements

2.3.1. Fisher Information Operator

Using the concept of quantum Fisher information, one can determine the optimal coherent state for estimating a parameter hidden within a linear scattering system[3]. This result was first shown in Ref. [1]. In this section, we will present the main findings from the paper, following the derivations in the corresponding supplemental material and some unpublished notes of Lukas Rachbauer.

Definition. *A coherent state $|\alpha\rangle$ is an eigenstate of the annihilation operator of the harmonic oscillator, i.e., $\hat{a}\,|\alpha\rangle = \alpha\,|\alpha\rangle$. Using the Fock basis $\{|n\rangle\}_{n=0}^{\infty}$, it can be written like*

$$|\alpha\rangle = \mathrm{e}^{-|\alpha|^2/2} \sum_{n=0}^{\infty} \frac{\alpha^n}{\sqrt{n!}}\,|n\rangle\,. \tag{2.7}$$

[3] As our ongoing research shows, one can extract more information using states that feature quantum phenomena like entanglement.

A coherent state is a quantum state with minimal uncertainty that most resembles a classical field. From Eq. (2.7), one can see that for a coherent state, the probability of measuring n photons follows a Poisson distribution with an expectation value of $|\alpha|^2$.

Plugging a θ-dependent coherent state into Eq. (2.6), we obtain the corresponding quantum Fisher information after a tedious (but straight-forward) calculation:

$$
\begin{aligned}
|\partial_\theta \alpha(\theta)\rangle &= -\frac{1}{2}\mathrm{e}^{-\frac{|\alpha(\theta)|^2}{2}}\left(\partial_\theta |\alpha(\theta)|^2\right)\sum_{n=0}^{\infty}\frac{\alpha^n(\theta)}{\sqrt{n!}}|n\rangle \\
&\quad + \mathrm{e}^{-\frac{|\alpha(\theta)|^2}{2}}\left(\partial_\theta \alpha(\theta)\right)\sum_{n=1}^{\infty}\frac{n\alpha^{n-1}(\theta)}{\sqrt{n!}}|n\rangle\,, \\
\langle\partial_\theta\alpha(\theta)|\partial_\theta\alpha(\theta)\rangle &= \frac{1}{4}\mathrm{e}^{-|\alpha(\theta)|^2}\left(\partial_\theta |\alpha(\theta)|^2\right)^2\sum_{n=0}^{\infty}\frac{|\alpha(\theta)|^{2n}}{n!} \\
&\quad + \mathrm{e}^{-|\alpha(\theta)|^2}|\partial_\theta\alpha(\theta)|^2\sum_{n=1}^{\infty}\frac{n^2|\alpha(\theta)|^{2(n-1)}}{n!} \\
&\quad - \frac{1}{2}\mathrm{e}^{-|\alpha(\theta)|^2}\left(\partial_\theta |\alpha(\theta)|^2\right)\left(\frac{\partial_\theta\alpha(\theta)}{\alpha(\theta)}+\frac{\partial_\theta\alpha^*(\theta)}{\alpha^*(\theta)}\right)\sum_{n=1}^{\infty}\frac{n|\alpha(\theta)|^{2n}}{n!} \\
&= \frac{1}{4}\left(\partial_\theta |\alpha(\theta)|^2\right)^2 + \left(1+|\alpha(\theta)|^2\right)|\partial_\theta\alpha(\theta)|^2 \\
&\quad - \frac{1}{2}|\alpha(\theta)|^2\left(\partial_\theta |\alpha(\theta)|^2\right)\left(\frac{\partial_\theta\alpha(\theta)}{\alpha(\theta)}+\frac{\partial_\theta\alpha^*(\theta)}{\alpha^*(\theta)}\right), \\
\langle\alpha(\theta)|\partial_\theta\alpha(\theta)\rangle &= -\frac{1}{2}\mathrm{e}^{-|\alpha(\theta)|^2}\left(\partial_\theta |\alpha(\theta)|^2\right)\sum_{n=0}^{\infty}\frac{|\alpha(\theta)|^{2n}}{n!} \\
&\quad + \mathrm{e}^{-|\alpha(\theta)|^2}\frac{\partial_\theta\alpha(\theta)}{\alpha(\theta)}\sum_{n=1}^{\infty}\frac{n|\alpha(\theta)|^{2n}}{n!} \\
&= -\frac{1}{2}\left(\partial_\theta |\alpha(\theta)|^2\right) + |\alpha(\theta)|^2\frac{\partial_\theta\alpha(\theta)}{\alpha(\theta)}, \\
|\langle\alpha(\theta)|\partial_\theta\alpha(\theta)\rangle|^2 &= \frac{1}{4}\left(\partial_\theta |\alpha(\theta)|^2\right)^2 + |\alpha(\theta)|^2|\partial_\theta\alpha(\theta)|^2 \\
&\quad - \frac{1}{2}|\alpha(\theta)|^2\left(\partial_\theta |\alpha(\theta)|^2\right)\left(\frac{\partial_\theta\alpha(\theta)}{\alpha(\theta)}+\frac{\partial_\theta\alpha^*(\theta)}{\alpha^*(\theta)}\right), \\
\implies H(\theta) &= 4\left(\langle\partial_\theta\alpha(\theta)|\partial_\theta\alpha(\theta)\rangle - |\langle\alpha(\theta)|\partial_\theta\alpha(\theta)\rangle|^2\right) \\
&= 4|\partial_\theta\alpha(\theta)|^2
\end{aligned}
$$

Using this result, we can find the quantum Fisher information for multi-mode

coherent states $|\boldsymbol{\alpha}(\theta)\rangle = |\alpha_1(\theta)\rangle \dots |\alpha_N(\theta)\rangle$:[4]

$$
\begin{aligned}
|\partial_\theta \boldsymbol{\alpha}(\theta)\rangle &= \sum_{i=1}^{N} \dots |\alpha_{i-1}(\theta)\rangle\, |\partial_\theta \alpha_i(\theta)\rangle\, |\alpha_{i+1}(\theta)\rangle \dots \\
\langle \partial_\theta \boldsymbol{\alpha}(\theta) | \partial_\theta \boldsymbol{\alpha}(\theta)\rangle &= \sum_{i=1}^{N} \langle \partial_\theta \alpha_i(\theta) | \partial_\theta \alpha_i(\theta)\rangle \\
&\quad + \sum_{i=1}^{N} \sum_{\substack{j=1 \\ j\neq i}}^{N} \langle \partial_\theta \alpha_i(\theta) | \alpha_i(\theta)\rangle\, \langle \alpha_j(\theta) | \partial_\theta \alpha_j(\theta)\rangle \\
\langle \partial_\theta \boldsymbol{\alpha}(\theta) | \boldsymbol{\alpha}(\theta)\rangle &= \sum_{i=1}^{N} \langle \partial_\theta \alpha_i(\theta) | \alpha_i(\theta)\rangle \\
|\, \langle \partial_\theta \boldsymbol{\alpha}(\theta) | \boldsymbol{\alpha}(\theta)\rangle\, |^2 &= \sum_{i=1}^{N} \sum_{j=1}^{N} \langle \partial_\theta \alpha_i(\theta) | \alpha_i(\theta)\rangle\, \langle \alpha_j(\theta) | \partial_\theta \alpha_j(\theta)\rangle \\
\implies H_{\mathrm{MM}}(\theta) &= 4 \left(\langle \partial_\theta \boldsymbol{\alpha}(\theta) | \partial_\theta \boldsymbol{\alpha}(\theta)\rangle - |\, \langle \partial_\theta \boldsymbol{\alpha}(\theta) | \boldsymbol{\alpha}(\theta)\rangle\, |^2 \right) \\
&= 4 \sum_{i=1}^{N} \left(\langle \partial_\theta \alpha_i(\theta) | \partial_\theta \alpha_i(\theta)\rangle - \langle \partial_\theta \alpha_i(\theta) | \alpha_i(\theta)\rangle\, \langle \alpha_i(\theta) | \partial_\theta \alpha_i(\theta)\rangle \right) \\
&= 4 \sum_{i=1}^{N} \left(\langle \partial_\theta \alpha_i(\theta) | \partial_\theta \alpha_i(\theta)\rangle - |\, \langle \partial_\theta \alpha_i(\theta) | \alpha_i(\theta)\rangle\, |^2 \right) \\
&= \sum_{i=1}^{N} H_i(\theta) \\
&= 4 \sum_{i=1}^{N} |\partial_\theta \alpha_i(\theta)|^2 \\
&= 4 \|\partial_\theta \boldsymbol{\alpha}(\theta)\|^2. \qquad (2.8)
\end{aligned}
$$

Here, $H_{\mathrm{MM}}(\theta)$ denotes the quantum Fisher information for a multi-mode coherent state. We conclude that we can compute the latter as the sum of the quantum Fisher information contained in each mode, which we expected due to the additivity of Fisher information for independent variables. In Ref. [1], the authors show that the homodyne detection scheme constitutes an optimal POVM since it maximizes the classical Fisher information to yield the quantum Fisher information for coherent states from Eq. (2.8).

We can write Eq. (2.8) in terms of the scattering matrix $\mathbf{S}$, which relates the wavefront going into a linear scattering system $\mathbf{c}^{\mathrm{in}}$ with the wavefront coming out of it $\mathbf{c}^{\mathrm{out}}(\theta)$:

$$\mathbf{c}^{\mathrm{out}}(\theta) = \mathbf{S}(\theta)\mathbf{c}^{\mathrm{in}}. \qquad (2.9)$$

[4] Here, the α_i are independent complex parameters.

Since the annihilation operator of the ith channel $\hat{a}_i$ is also the complex amplitude operator for classical fields (see Ref. [12]), we can identify

$$\alpha_i(\theta) = \langle \boldsymbol{\alpha}(\theta) | \hat{a}_i | \boldsymbol{\alpha}(\theta) \rangle = c_i^{\text{out}}(\theta).$$

From Eqs. (2.8) and (2.9), we thus obtain:

$$\begin{aligned} H_{\text{MM}}(\theta) &= 4\|\partial_\theta \boldsymbol{\alpha}(\theta)\|^2 \\ &= 4\|\partial_\theta \mathbf{c}^{\text{out}}(\theta)\|^2 \\ &= 4\| \left(\partial_\theta \mathbf{S}(\theta)\right) \mathbf{c}^{\text{in}}\|^2 \\ &= 4 \left(\mathbf{c}^{\text{in}}\right)^\dagger \left(\partial_\theta \mathbf{S}(\theta)\right)^\dagger \left(\partial_\theta \mathbf{S}(\theta)\right) \mathbf{c}^{\text{in}} \\ &= 4 \left(\mathbf{c}^{\text{in}}\right)^\dagger \mathbf{F}(\theta) \mathbf{c}^{\text{in}}. \end{aligned} \tag{2.10}$$

In the last equality, we introduced the Hermitian matrix

$$\mathbf{F}(\theta) = \left(\partial_\theta \mathbf{S}(\theta)\right)^\dagger \left(\partial_\theta \mathbf{S}(\theta)\right), \tag{2.11}$$

which we call Fisher information operator.[5] The eigenstate corresponding to its largest eigenvalue constitutes the wavefront that extracts the most quantum (!) Fisher information from the system for a fixed mean number of incoming photons/input intensity and N open channels. This result is remarkable: it provides a simple algorithm to engineer an optimal coherent probe state only having access to the far field.

2.3.2. Fisher Information Flow

In addition to knowing how much information we can extract in the far field, we are interested in how this information behaves locally within a complex scattering medium. We want to understand where it is created, whether it is conserved, and how it is transported by an electromagnetic wave. We can answer all these questions using the concept of the Fisher information flow, which is the main topic of this work. In this section, we will derive it and discuss its mathematical properties following unpublished ideas and notes of Jakob Hüpfl, Lukas Rachbauer, and Stefan Rotter.

Quantum Mechanical Waves

The Schrödinger equation governs the time evolution of a quantum mechanical state $\psi(\mathbf{r}, t)$ in a system characterized by a potential $V(\mathbf{r}, t)$:

$$\begin{aligned} \mathrm{i}\hbar\partial_t \psi(\mathbf{r}, t) &= \hat{H}\psi(\mathbf{r}, t) \\ &= \left(-\frac{\hbar^2}{2m}\Delta + V(\mathbf{r}, t)\right) \psi(\mathbf{r}, t), \end{aligned} \tag{2.12}$$

[5] Strictly speaking, we should call $\mathbf{F}(\theta)$ Fisher information matrix since it acts on the vector space of mode compositions rather than on the Hilbert space. However, to avoid confusion, we follow the literature convention and refer to $\mathbf{F}(\theta)$ as Fisher information operator.

where $\hat{H}$ denotes the Hamiltonian of the system. One can define a continuity equation

$$\partial_t \rho(\mathbf{r}, t) + \nabla \cdot \mathbf{j}(\mathbf{r}, \mathbf{t}) = \sigma(\mathbf{r}, t) \tag{2.13}$$

corresponding to a charge $Q = \int \rho(\mathbf{r}, t) d^3r$. The interpretation of the three terms is:

- $\rho(\mathbf{r}, t)$ is the charge per volume at position $\mathbf{r}$ and time t
- $\mathbf{j}(\mathbf{r}, t)$ is the flux density or flow of the charge, i.e., the charge per surface and per time that flows in the direction of $\mathbf{j}(\mathbf{r}, t)$ at position $\mathbf{r}$ and time t
- $\sigma(\mathbf{r}, t)$ is the charge that is created ($\sigma(\mathbf{r}, t) > 0$) or destroyed ($\sigma(\mathbf{r}, t) < 0$) at position $\mathbf{r}$ and time t

If we identify the charge density as the probability density of finding the particle at position $\mathbf{r}$ and time t, we find

$$\begin{aligned}
\rho(\mathbf{r}, t) &= |\psi(\mathbf{r}, t)|^2, \\
\mathbf{j}(\mathbf{r}, t) &= \frac{\hbar}{2\mathrm{i}m}(\psi(\mathbf{r}, t)^* \nabla \psi(\mathbf{r}, t) - \psi(\mathbf{r}, t) \nabla \psi(\mathbf{r}, t)^*) \\
&= \frac{\hbar}{m} \Im \left\{ \psi(\mathbf{r}, t)^* \nabla \psi(\mathbf{r}, t) \right\}, \\
\sigma(\mathbf{r}, t) &= 0,
\end{aligned}$$

where $\Im\{\cdot\}$ denotes the imaginary part. The source term is zero since probability can be neither created nor destroyed locally.

Similarly, we can identify a charge related to the Fisher information in systems that depend on an arbitrary parameter θ. Differentiating the Schrödinger equation with respect to θ, we find:[6]

$$\mathrm{i}\hbar \partial_t \partial_\theta \psi = -\frac{\hbar^2}{2m} \Delta \partial_\theta \psi + \partial_\theta V \psi + V \partial_\theta \psi$$

Multiplying with $\partial_\theta \psi^*$ and complex conjugation furnishes:

$$\mathrm{i}\hbar \partial_\theta \psi^* \partial_t \partial_\theta \psi = -\frac{\hbar^2}{2m} \partial_\theta \psi^* \Delta \partial_\theta \psi + \partial_\theta V \partial_\theta \psi^* \psi + V \partial_\theta \psi^* \partial_\theta \psi \tag{2.14}$$

$$-\mathrm{i}\hbar \partial_\theta \psi \partial_t \partial_\theta \psi^* = -\frac{\hbar^2}{2m} \partial_\theta \psi \Delta \partial_\theta \psi^* + \partial_\theta V^* \partial_\theta \psi \psi^* + V^* \partial_\theta \psi \partial_\theta \psi^* \tag{2.15}$$

Subtracting Eq. (2.15) from Eq. (2.14), we obtain on the left-hand side:

$$\begin{aligned}
LHS &= \mathrm{i}\hbar(\partial_\theta \psi^* \partial_t \partial_\theta \psi + \partial_\theta \psi \partial_t \partial_\theta \psi^*) \\
&= \mathrm{i}\hbar \partial_t (\partial_\theta \psi^* \partial_\theta \psi) \\
&= \mathrm{i}\hbar \partial_t |\partial_\theta \psi|^2.
\end{aligned}$$

[6] To save some space, we do not write the explicit dependence on position, time, and the parameter of interest.

The right-hand side reads:

$$\begin{aligned} RHS &= -\frac{\hbar^2}{2m}(\partial_\theta\psi^*\Delta\partial_\theta\psi - \partial_\theta\psi\Delta\partial_\theta\psi^*) + 2\mathrm{i}\Im\left\{\partial_\theta V\partial_\theta\psi^*\psi + V\partial_\theta\psi^*\partial_\theta\psi\right\} \\ &= -\frac{\hbar^2}{2m}\nabla\cdot(\partial_\theta\psi^*\nabla\partial_\theta\psi - \partial_\theta\psi\nabla\partial_\theta\psi^*) + 2\mathrm{i}\Im\left\{\partial_\theta V\partial_\theta\psi^*\psi + V\partial_\theta\psi^*\partial_\theta\psi\right\} \\ &= -\frac{\mathrm{i}\hbar^2}{m}\nabla\cdot(\Im\left\{\partial_\theta\psi^*\nabla\partial_\theta\psi\right\}) + 2\mathrm{i}\Im\left\{\partial_\theta V\partial_\theta\psi^*\psi + V\partial_\theta\psi^*\partial_\theta\psi\right\}. \end{aligned}$$

Setting $LHS = RHS$, we find

$$\begin{aligned} \mathrm{i}\hbar\partial_t|\partial_\theta\psi|^2 + \frac{\mathrm{i}\hbar^2}{m}\nabla\cdot(\Im\left\{\partial_\theta\psi^*\nabla\partial_\theta\psi\right\}) \\ = 2\mathrm{i}\Im\left\{\partial_\theta V\partial_\theta\psi^*\psi + V\partial_\theta\psi^*\partial_\theta\psi\right\}. \end{aligned} \tag{2.16}$$

By comparing Eq. (2.16) to the continuity equation (Eq. (2.13)), we can identify the Fisher information charge density ρ^{FI}, the Fisher information flow $\mathbf{j}^{\mathrm{FI}}$, and the Fisher information source term σ^{FI}:

$$\begin{aligned} \rho^{\mathrm{FI}} &= |\partial_\theta\psi|^2, \\ \mathbf{j}^{\mathrm{FI}} &= \frac{\hbar}{m}\Im\left\{\partial_\theta\psi^*\nabla\partial_\theta\psi\right\}, \\ \sigma^{\mathrm{FI}} &= \frac{2}{\hbar}\Im\left\{\partial_\theta V\partial_\theta\psi^*\psi + V\partial_\theta\psi^*\partial_\theta\psi\right\}. \end{aligned} \tag{2.17}$$

Let us list some properties of these quantities:

- All quantities are real by construction.

- For a real potential V (i.e., for a system without gain or loss), the source term simplifies to $\sigma^{\mathrm{FI}} = \frac{2}{\hbar}\partial_\theta V\Im\left\{\partial_\theta\psi^*\psi\right\}$. We deduce that information can only be created at positions where the potential changes with the parameter of interest ($\partial_\theta V \neq 0$), which is intuitive. To extract a lot of information, the wave should have a high intensity in regions where the potential changes with θ.

- In the stationary case, we have $\partial_t\rho^{\mathrm{FI}} = 0$, and thus $\nabla\cdot\mathbf{j}^{\mathrm{FI}} = \sigma^{\mathrm{FI}}$. Integrating over a region D with boundary ∂D, we find using Gauss's theorem

  $$\int_{\partial D}\mathbf{j}^{\mathrm{FI}}\cdot d\mathbf{A} = \int_D \sigma^{\mathrm{FI}}dV = \int_{\mathrm{supp}(\sigma^{\mathrm{FI}})}\sigma^{\mathrm{FI}}dV.$$

  The Fisher information flowing through any closed surface is thus equal to the integrated sources (i.e., $\sigma^{\mathrm{FI}} > 0$)/sinks (i.e., $\sigma^{\mathrm{FI}} < 0$) within that surface.

Scalar Classical Waves

In this section, we will show that the classical scalar wave equation and the Schrödinger equation are equivalent in the stationary case. We have to take into account that classical electromagnetic waves and massive Schrödinger particles follow different dispersion relations:

$$\begin{aligned}\omega_H &= ck_H \\ E_S = \hbar\omega_S &= \frac{\hbar^2 k_S^2}{2m},\end{aligned}$$

where we use the sub-index H ("Helmholtz") for the classical dispersion relation and the sub-index S ("Schrödinger") for the quantum mechanical dispersion relation. The equivalence between Helmholtz and stationary Schrödinger equation only holds for a fixed value of frequency or wave number. We choose to fix the wave number $k = k_H = k_S$. The corresponding frequencies $\omega_H \neq \omega_S$ can be computed using the different dispersion relations.

- Scalar electromagnetic waves $\psi(\mathbf{r}, t)$ are governed by the following wave equation:

$$\left(\Delta - \frac{n(\mathbf{r},t)^2}{c^2}\partial_t^2\right)\psi(\mathbf{r},t) = 0,$$

  where we defined the refractive index as $n(\mathbf{r},t) = \sqrt{\epsilon(\mathbf{r},t)\mu(\mathbf{r},t)}$. In the stationary case, $n(\mathbf{r},t) = n(\mathbf{r})$. Assuming harmonic time-dependency $\psi(\mathbf{r},t) = \mathrm{e}^{-\mathrm{i}\omega_H t}\psi(\mathbf{r})$, we retrieve the stationary wave equation, i.e., the Helmholtz equation:

$$\left(\Delta + n(\mathbf{r})^2 k^2\right)\psi(\mathbf{r}) = 0 \tag{2.18}$$

- For the Schrödinger equation (Eq. (2.12)), we obtain in the stationary case (i.e., $V(\mathbf{r},t) = V(\mathbf{r})$) and assuming harmonic time-dependence $\psi(\mathbf{r},t) = \mathrm{e}^{-\mathrm{i}\omega_S t}\psi(\mathbf{r})$:

$$\begin{aligned}&\left(-\frac{\hbar^2}{2m}\Delta + V(\mathbf{r})\right)\psi(\mathbf{r}) = E_S\psi(\mathbf{r}) \\ \Longrightarrow\ &\left(\Delta + \frac{2m}{\hbar^2}\left(E_S - V(\mathbf{r})\right)\right)\psi(\mathbf{r}) = 0 \\ \Longrightarrow\ &\left(\Delta + \left(k^2 - \frac{2m}{\hbar^2}V(\mathbf{r})\right)\right)\psi(\mathbf{r}) = 0.\end{aligned} \tag{2.19}$$

Comparing Eq. (2.18) and Eq. (2.19), we find that they have the same form if we identify

$$\begin{aligned} V(\mathbf{r}) &= \frac{\hbar^2 k^2}{2m}(1 - n(\mathbf{r})^2) \\ &\Updownarrow \\ n(\mathbf{r}) &= \sqrt{1 - \frac{2m}{\hbar^2 k^2} V(\mathbf{r})} = \sqrt{1 - \frac{V(\mathbf{r})}{E_S}}. \end{aligned} \tag{2.20}$$

Replacing the potential $V(\mathbf{r})$ by a refractive index $n(\mathbf{r})$ in Eq. (2.17) and dividing by the common prefactor $\frac{\hbar}{m}$, we obtain:

$$\begin{aligned} \mathbf{j}^{\mathrm{FI}} &= \Im\left\{\partial_\theta \psi^* \nabla \partial_\theta \psi\right\}, \\ \sigma^{\mathrm{FI}} &= \frac{2m}{\hbar^2} \Im\left\{\partial_\theta V \partial_\theta \psi^* \psi + V \partial_\theta \psi^* \partial_\theta \psi\right\} \\ &= k^2 \Im\left\{\partial_\theta (1 - n^2) \partial_\theta \psi^* \psi + (1 - n^2) \partial_\theta \psi^* \partial_\theta \psi\right\} \\ &= -k^2 \Im\left\{2n \partial_\theta n \partial_\theta \psi^* \psi + (n^2 - 1) \partial_\theta \psi^* \partial_\theta \psi\right\}. \end{aligned} \tag{2.21}$$

It is useful to keep the units of these quantities in mind:

$$\begin{aligned} \left[\mathbf{j}^{\mathrm{FI}}\right] &= [\theta]^{-2} \cdot [\psi]^2 \cdot [L]^{-1}, \\ \left[\sigma^{\mathrm{FI}}\right] &= [\theta]^{-2} \cdot [\psi]^2 \cdot [k]^2 \\ &= [\theta]^{-2} \cdot [\psi]^2 \cdot [L]^{-2}, \end{aligned} \tag{2.22}$$

where $[L]$ denotes a unit of length.

We conclude that we can also define the Fisher information flow $\mathbf{j}^{\mathrm{FI}}$ and the Fisher information source term σ^{FI} for stationary scalar classical waves. In Sec. 2.5, we will show that the Fisher information flow from Eq. (2.21) is a local representation of the Fisher information operator from Eq. (2.11).

2.3.3. Finite-Difference Fisher Information Flow

In experiments, it is often hard to determine the change of the wavefunction for small perturbations of the parameter of interest θ due to the small signal-to-noise ratio. As a consequence, we cannot compute the derivative with respect to θ. Nonetheless, we can define a modified Fisher information flow replacing the derivatives with finite differences. Let $V(\theta_1) \equiv V_1$ and $V(\theta_2) \equiv V_2$ be two arbitrarily different potentials. We denote the solutions of the corresponding Schrödinger equations as $\psi(\theta_1) \equiv \psi_1$ and $\psi(\theta_2) \equiv \psi_2$. We further write the difference quotient between the potentials/wavefunctions as

$$\begin{aligned} \mathcal{D}V &\coloneqq \frac{V_2 - V_1}{\theta_2 - \theta_1}, \\ \mathcal{D}\psi &\coloneqq \frac{\psi_2 - \psi_1}{\theta_2 - \theta_1}, \end{aligned}$$

and the average as

$$\overline{V} \coloneqq \frac{V_1 + V_2}{2},$$
$$\overline{\psi} \coloneqq \frac{\psi_1 + \psi_2}{2}.$$

Then, we can define the Fisher information charge density/flow/source term as:

$$\begin{aligned}
\rho^{\mathrm{FI}} &= |\mathcal{D}\psi|^2, \\
\mathbf{j}^{\mathrm{FI}} &= \frac{\hbar}{m} \Im \left\{ \mathcal{D}\psi^* \nabla \mathcal{D}\psi \right\}, \\
\sigma^{\mathrm{FI}} &= \frac{2}{\hbar} \Im \left\{ \mathcal{D}V \mathcal{D}\psi^* \overline{\psi} + \overline{V} \mathcal{D}\psi^* \mathcal{D}\psi \right\},
\end{aligned} \tag{2.23}$$

Note that we do not distinguish between the Fisher information charge density/flow/source term for infinitesimal and finite perturbations in the notation. Eq. (2.23) can be derived by realizing that

$$\mathcal{D}(V\psi) \coloneqq \frac{V_2\psi_2 - V_1\psi_1}{\theta_2 - \theta_1} = \mathcal{D}V\overline{\psi} + \overline{V}\mathcal{D}\psi,$$

similar to the product rule. From the difference quotient of the Schrödinger equation

$$\mathrm{i}\hbar\partial_t \mathcal{D}\psi = -\frac{\hbar^2}{2m}\Delta\mathcal{D}\psi + \mathcal{D}(V\psi),$$

we then find

$$\begin{aligned}
\partial_t \rho^{\mathrm{FI}} &= \partial_t(\mathcal{D}\psi^*\mathcal{D}\psi) \\
&= \partial_t \mathcal{D}\psi^* \mathcal{D}\psi + \mathcal{D}\psi^* \partial_t \mathcal{D}\psi \\
&= \left(+\frac{\hbar}{2\mathrm{i}m}\Delta\mathcal{D}\psi^* - \frac{1}{\mathrm{i}\hbar}\mathcal{D}(V^*\psi^*) \right) \mathcal{D}\psi + \mathcal{D}\psi^* \left(-\frac{\hbar}{2\mathrm{i}m}\Delta\mathcal{D}\psi + \frac{1}{\mathrm{i}\hbar}\mathcal{D}(V\psi) \right) \\
&= \left(+\frac{\hbar}{2\mathrm{i}m}\Delta\mathcal{D}\psi^* - \frac{1}{\mathrm{i}\hbar}\mathcal{D}V^*\overline{\psi}^* - \frac{1}{\mathrm{i}\hbar}\overline{V}^*\mathcal{D}\psi^* \right) \mathcal{D}\psi \\
&\quad + \mathcal{D}\psi^* \left(-\frac{\hbar}{2\mathrm{i}m}\Delta\mathcal{D}\psi + \frac{1}{\mathrm{i}\hbar}\mathcal{D}V\overline{\psi} + \frac{1}{\mathrm{i}\hbar}\overline{V}\mathcal{D}\psi \right) \\
&= \frac{\hbar}{2\mathrm{i}m} \left(\Delta\mathcal{D}\psi^*\mathcal{D}\psi - \mathcal{D}\psi^*\Delta\mathcal{D}\psi \right) \\
&\quad + \frac{1}{\mathrm{i}\hbar} \left(\mathcal{D}\psi^*\mathcal{D}V\overline{\psi} + \mathcal{D}\psi^*\overline{V}\mathcal{D}\psi - \mathcal{D}V^*\overline{\psi}^*\mathcal{D}\psi - \overline{V}^*\mathcal{D}\psi^*\mathcal{D}\psi \right) \\
&= -\frac{\hbar}{2\mathrm{i}m}\nabla \cdot \left(\mathcal{D}\psi^*\nabla\mathcal{D}\psi - \nabla\mathcal{D}\psi^*\mathcal{D}\psi \right) \\
&\quad + \frac{1}{\mathrm{i}\hbar} \left(\mathcal{D}\psi^*\mathcal{D}V\overline{\psi} - \mathcal{D}V^*\overline{\psi}^*\mathcal{D}\psi + \mathcal{D}\psi^*\overline{V}\mathcal{D}\psi - \overline{V}^*\mathcal{D}\psi^*\mathcal{D}\psi \right)
\end{aligned}$$

$$
\begin{aligned}
&= -\frac{\hbar}{m}\nabla\cdot\left(\Im\left\{\mathcal{D}\psi^*\nabla\mathcal{D}\psi\right\}\right)\\
&\quad+\frac{2}{\hbar}\left(\Im\left\{\mathcal{D}\psi^*\mathcal{D}V\overline{\psi}+\mathcal{D}\psi^*\overline{V}\mathcal{D}\psi\right\}\right)\\
&= -\nabla\cdot\mathbf{j}^{\mathrm{FI}}+\sigma^{\mathrm{FI}},
\end{aligned}
$$

i.e., the continuity equation. As in Sec. 2.3.2, we can define the finite-difference Fisher information flow for stationary scalar classical waves by replacing the potentials with refractive indices following Eq. (2.20). We find:

$$
\begin{aligned}
\mathbf{j}^{\mathrm{FI}} &= \Im\left\{\mathcal{D}\psi^*\nabla\mathcal{D}\psi\right\},\\
\sigma^{\mathrm{FI}} &= -k^2\Im\left\{\mathcal{D}n^2\mathcal{D}\psi^*\psi+\left(\overline{n^2}-1\right)\mathcal{D}\psi^*\mathcal{D}\psi\right\},
\end{aligned}
\tag{2.24}
$$

where we discarded the prefactor $\frac{\hbar}{m}$. In the limit of $\theta_2-\theta_1\to 0$, we retrieve the infinitesimal expressions from Eq. (2.21). Remarkably, all the properties of the Fisher information flow also hold in the finite-difference case, as we will see in Sec. 2.5. Therefore, we will often not distinguish between the infinitesimal and the finite-difference Fisher information flow/source term in the following sections.

2.4. Electromagnetic Waves in Waveguides

This section introduces the theoretical tools to describe electromagnetic (EM) waves in the simulation (Ch. 3) and the experiment (Ch. 4) from this work. We will use this framework to continue our discussion of the Fisher information in the following section, where we relate the Fisher information flow to the Fisher information operator and present methods to control the flow of information in a complex scattering system.

Electromagnetic waves are prone to high loss when propagating through cables due to the Skin effect. Therefore, one generally uses waveguides to transmit them. In the following, we first discuss general results for EM waves in a perfectly conducting waveguide of constant cross-section, which is infinitely long in x-direction. Then, we study the case of a rectangular waveguide in greater detail. Our discussions follow Refs. [13, 14]. Note that we use a different coordinate system than the literature. We have

$$
\begin{aligned}
x &= \tilde{z},\\
y &= \tilde{y},\\
z &= -\tilde{x},
\end{aligned}
$$

where the quantities without tilde denote the coordinate system used in this work and the tilded quantities denote the coordinate system used in the literature.

We state without a proof that all waves in a waveguide can be written as a linear combination of the following types of modes:

- Transverse electromagnetic (TEM) modes: **E**- and **H**-field transverse to the direction of propagation (i.e., the x-direction),
- Transverse electric (TE) modes: **E**-field transverse to the direction of propagation, **H**-field has a longitudinal component,
- Transverse magnetic (TM) modes: **H**-field transverse to the direction of propagation, **E**-field has a longitudinal component.

To obtain the wave equations that govern these types of modes, we start by listing the macroscopic Maxwell equations in Gaussian units:

$$\begin{aligned} \nabla \cdot \mathbf{D} &= 4\pi\rho_\mathrm{f}, \\ \nabla \times \mathbf{E} &= -\frac{1}{c}\partial_t \mathbf{B}, \\ \nabla \cdot \mathbf{B} &= 0, \\ \nabla \times \mathbf{H} &= \frac{4\pi}{c}\mathbf{j}_\mathrm{f} + \frac{1}{c}\partial_t \mathbf{D}. \end{aligned}$$

We assume that the medium within the waveguide does not carry any free charges ($\rho_\mathrm{f} = 0$) nor any free currents ($\mathbf{j}_\mathrm{f} = \mathbf{0}$). Furthermore, we consider a linear medium with constant permittivity and permeability, i.e., $\mathbf{D} = \epsilon\mathbf{E}$ and $\mathbf{B} = \mu\mathbf{H}$. With these simplifications, we arrive at:

$$\begin{aligned} \nabla \cdot \mathbf{E} &= 0, \\ \nabla \times \mathbf{E} &= -\frac{\mu}{c}\partial_t \mathbf{H}, \\ \nabla \cdot \mathbf{H} &= 0, \\ \nabla \times \mathbf{H} &= \frac{\epsilon}{c}\partial_t \mathbf{E}. \end{aligned} \tag{2.25}$$

Applying the curl operator to the second and the fourth equation of Eq. (2.25) and using $\nabla \times (\nabla \times \mathbf{A}) = \nabla(\nabla \cdot \mathbf{A}) - \nabla^2\mathbf{A}$, we retrieve the 3D Helmholtz equations for **E** and **H**:

$$\begin{aligned} \left(\frac{\epsilon\mu}{c^2}\partial_t^2 - \nabla^2\right)\mathbf{E} &= \mathbf{0}, \\ \left(\frac{\epsilon\mu}{c^2}\partial_t^2 - \nabla^2\right)\mathbf{H} &= \mathbf{0}. \end{aligned} \tag{2.26}$$

Since the waves propagate freely in x-direction we write[7]:

$$\begin{aligned} \mathbf{E} &= \hat{\mathbf{E}}(y,z)\ \mathrm{e}^{\mathrm{i}(k_x x - \omega t)}, \\ \mathbf{H} &= \hat{\mathbf{H}}(y,z)\ \mathrm{e}^{\mathrm{i}(k_x x - \omega t)}. \end{aligned} \tag{2.27}$$

Furthermore, we separate all vector quantities into a component which is longitudinal and a component which is transverse to the x-direction ($\mathbf{v} = \mathbf{v}_\mathrm{t} + \mathbf{v}_x$ for an arbitrary vector/vector-valued operator $\mathbf{v}$).

[7] Here, we work with waves that propagate in positive x-direction. To retrieve the results for waves propagating in negative x-direction, one can substitute $k_x \to -k_x$.

2.4.1. TEM Modes

For TEM modes, we have $E_x = H_x = 0$. From Gauss's law it follows that

$$\nabla_\mathrm{t} \cdot \hat{\mathbf{E}}_\mathrm{t} = 0,$$

and from Faraday's law we deduce that

$$\hat{\mathbf{e}}_x \cdot \nabla \times \hat{\mathbf{E}} = \mathrm{i}\frac{\omega\mu}{c}\hat{H}_x \implies \nabla_\mathrm{t} \times \hat{\mathbf{E}}_\mathrm{t} = \mathbf{0}.$$

We can thus obtain $\hat{\mathbf{E}}_\mathrm{t}$ by solving a 2D electrostatic problem. Since the boundary of a conducting waveguide is an equipotential surface and there are no charges within the waveguide, TEM modes can not exist in a waveguide that consists of only one connected surface. Only if there are two or more connected surfaces contained within each other (e.g., a coaxial cable) do we observe TEM modes in the regions between the surfaces. For our use case, i.e., a single rectangular waveguide, TEM modes thus do not arise, and we can focus on TE and TM modes.

2.4.2. TE and TM Modes

Plugging Eq. (2.27) into Faraday's equation we obtain:

$$\begin{aligned}\nabla \times \mathbf{E} &= -\frac{\mu}{c}\partial_t \mathbf{H} \\ &= \mathrm{i}\omega\frac{\mu}{c}\mathbf{H}\end{aligned} \tag{2.28}$$

Using $\hat{\mathbf{e}}_x \times (\nabla \times \mathbf{v}) = \nabla_\mathrm{t} v_x - \partial_x \mathbf{v}_\mathrm{t}$ and $\hat{\mathbf{e}}_x \times \mathbf{v} = \hat{\mathbf{e}}_x \times \mathbf{v}_\mathrm{t}$, we can rewrite Eq. (2.28) like

$$\nabla_\mathrm{t} E_x = \mathrm{i}k_x \mathbf{E}_\mathrm{t} + \mathrm{i}\omega\frac{\mu}{c}\hat{\mathbf{e}}_x \times \mathbf{H}_\mathrm{t}. \tag{2.29}$$

Similarly, we find

$$\nabla_\mathrm{t} H_x = \mathrm{i}k_x \mathbf{H}_\mathrm{t} - \mathrm{i}\omega\frac{\epsilon}{c}\hat{\mathbf{e}}_x \times \mathbf{E}_\mathrm{t}. \tag{2.30}$$

Applying $\hat{\mathbf{e}}_x\times$ to both equations and noting $\hat{\mathbf{e}}_x \times (\hat{\mathbf{e}}_x \times \mathbf{v}_\mathrm{t}) = -\mathbf{v}_\mathrm{t}$ leads to

$$\hat{\mathbf{e}}_x \times \nabla_\mathrm{t} E_x = \mathrm{i}k_x \hat{\mathbf{e}}_x \times \mathbf{E}_\mathrm{t} - \mathrm{i}\omega\frac{\mu}{c}\mathbf{H}_\mathrm{t}, \tag{2.31}$$

$$\hat{\mathbf{e}}_x \times \nabla_\mathrm{t} H_x = \mathrm{i}k_x \hat{\mathbf{e}}_x \times \mathbf{H}_\mathrm{t} + \mathrm{i}\omega\frac{\epsilon}{c}\mathbf{E}_\mathrm{t}. \tag{2.32}$$

Plugging Eq. (2.31) into Eq. (2.30) and Eq. (2.32) into Eq. (2.29) we find:

$$\begin{aligned}\mathbf{E}_\mathrm{t} &= \frac{\mathrm{i}}{\frac{\omega^2\epsilon\mu}{c^2} - k_x^2}\left(k_x \nabla_\mathrm{t} E_x - \frac{\omega\mu}{c}\hat{\mathbf{e}}_x \times \nabla_\mathrm{t} H_x\right), \\ \mathbf{H}_\mathrm{t} &= \frac{\mathrm{i}}{\frac{\omega^2\epsilon\mu}{c^2} - k_x^2}\left(k_x \nabla_\mathrm{t} H_x + \frac{\omega\epsilon}{c}\hat{\mathbf{e}}_x \times \nabla_\mathrm{t} E_x\right).\end{aligned} \tag{2.33}$$

Those equations imply that the transverse components of the fields are fixed by their x-components. The x-components are, in turn, fixed by the 2D Helmholtz equation, which we obtain by plugging Eq. (2.27) into the 3D Helmholtz equation (Eq. (2.26)):

$$\left(-\frac{\epsilon\mu\omega^2}{c^2} + k_x^2 - \partial_y^2 - \partial_z^2\right)\Psi(y,z) = 0, \tag{2.34}$$

where $\Psi = \hat{E}_x$ or $\Psi = \hat{H}_x$.

2.4.3. TE and TM Modes in a Rectangular Waveguide

In this section, we solve Eq. (2.34) for a waveguide of rectangular cross-section, which is placed parallel to the x-, y-, and z-direction. The waveguide is assumed to be infinitely long in x-direction, and it has side lengths of d_y in y-direction, and d_z in z-direction. Since the corresponding boundary conditions can be expressed independently for the y- and the z-direction, we can make a separation ansatz: $\Psi(y,z) = f(y)g(z)$. Inserting this ansatz into Eq. (2.34), we arrive at:

$$-\frac{\epsilon\mu\omega^2}{c^2} + k_x^2 - \frac{f''(y)}{f(y)} - \frac{g''(z)}{g(z)} = 0. \tag{2.35}$$

This implies that $\frac{f''(y)}{f(y)}$ and $\frac{g''(z)}{g(z)}$ are constant. The solution to such differential equations is a linear combination of sine and cosine functions, and the problem reduces to imposing boundary conditions on the walls of the waveguide, which read:

$$\mathbf{n} \times \mathbf{E} = \mathbf{0}, \tag{2.36}$$
$$\mathbf{n} \cdot \mathbf{H} = 0, \tag{2.37}$$

where $\mathbf{n}$ is a vector that is perpendicular to the waveguide wall. From Eq. (2.36), we note that the boundary condition for the x-component of the electric field reads $E_x|_S = 0$, where S denotes the boundary of the waveguide. Projecting Eq. (2.30) on $\mathbf{n}$ and using Eq. (2.37), we obtain the boundary condition for the x-component of the magnetic field $\frac{\partial}{\partial n}H_x|_S = 0$, where $\frac{\partial}{\partial n} = \mathbf{n} \cdot \nabla_\mathrm{t}$.

For TE modes, we set $E_x = 0$ and solve Eq. (2.35) for H_x. The boundary conditions impose that $f(y) = C_n \cos(\frac{n\pi y}{d_y})$ and $g(z) = C_m \cos(\frac{m\pi z}{d_z})$, where m and n are integers and C_m and C_n are constants. This leads to the x-component of the magnetic field for TE modes:

$$\hat{H}_x = H_{mn} \cos\left(\frac{n\pi y}{d_y}\right) \cos\left(\frac{m\pi z}{d_z}\right) \tag{2.38}$$

From this equation, we can compute all other fields using Eq. (2.33).

Analogously, we find the x-component of the electric field for TM modes:

$$\hat{E}_x = E_{mn} \sin\left(\frac{n\pi y}{d_y}\right) \sin\left(\frac{m\pi z}{d_z}\right) \tag{2.39}$$

Since we can label TE and TM modes using the two integers m and n, we denote them as $\mathrm{TE}_{m,n}$ and $\mathrm{TM}_{m,n}$ respectively.

For both TE and TM modes, we obtain the same dispersion relation by plugging either Eq. (2.38) or Eq. (2.39) into the 2D Helmholtz equation:

$$\begin{aligned} k_x^2 &\equiv (k_{m,n}^x)^2 \\ &= \frac{\epsilon\mu\omega^2}{c^2} - \left(\frac{n\pi}{d_y}\right)^2 - \left(\frac{m\pi}{d_z}\right)^2 \\ &\equiv k^2 - (k_n^y)^2 - (k_m^z)^2. \end{aligned} \tag{2.40}$$

Waves can only propagate freely if $k_x^2 > 0$; otherwise, k_x becomes complex, and they get damped exponentially (see Eq. (2.27)). Consequently, they only exist on length scales that are short compared to $1/\Im\{k_x\}$. We call modes with a real/complex k_x open/evanescent. For each mode (characterized by m and n), there is a cut-off frequency below which it becomes evanescent:

$$\omega_{\text{cut-off}}^2(m,n) = \frac{c^2}{\epsilon\mu}\left(\left(\frac{n\pi}{d_y}\right)^2 + \left(\frac{m\pi}{d_z}\right)^2\right). \tag{2.41}$$

While $\mathrm{TE}_{m,n}$ modes exist for $m = 0$, $n \geq 1$ or $m \geq 1$ and $n = 0$, $\mathrm{TM}_{m,n}$ modes require $m \geq 1$ and $n \geq 1$ (otherwise $\hat{E}_x = 0$ and consequently all other fields vanish as well). Therefore, only $\mathrm{TE}_{m,n}$ modes are present at low frequencies $\omega < \omega_{\text{cut-off}}(1,1)$.

$\mathrm{TE}_{0,n}$ modes

Finally, let us compute the explicit form of the $\mathrm{TE}_{0,n}$ modes, which are the only propagating modes if $d_y > \lambda/2 > d_z$, i.e., at low frequencies in a waveguide whose extent in z-direction is small compared to its extent in y-direction. Using Eq. (2.38), we find the x-components of the electromagnetic fields for those types of waves:

$$\begin{aligned} E_x &= 0, \\ H_x &= H_{0n} \cos\left(\frac{n\pi y}{d_y}\right) \mathrm{e}^{\mathrm{i}(k_n^x x - \omega t)}. \end{aligned}$$

From Eqs. (2.33) and (2.40), we obtain the remaining components:

$$\begin{aligned}
\mathbf{E} &= \mathbf{E}_\mathrm{t} \\
&= -\frac{\mathrm{i}}{\frac{\omega^2\epsilon\mu}{c^2} - (k_n^x)^2}\left(\frac{\omega\mu}{c}\hat{\mathbf{e}}_x \times \nabla_\mathrm{t} H_x\right) \\
&= \frac{\mathrm{i}}{\frac{\omega^2\epsilon\mu}{c^2} - (k_n^x)^2}\frac{\omega\mu}{c} H_{0n}\frac{n\pi}{d_y}\sin\left(\frac{n\pi y}{d_y}\right)\mathrm{e}^{\mathrm{i}(k_n^x x-\omega t)}\hat{\mathbf{e}}_x \times \hat{\mathbf{e}}_y \\
&= \frac{\mathrm{i}}{(k_n^y)^2}\frac{\omega\mu}{c} k_n^y H_{0n}\sin\left(\frac{n\pi y}{d_y}\right)\mathrm{e}^{\mathrm{i}(k_n^x x-\omega t)}\hat{\mathbf{e}}_z \\
&= \frac{\mathrm{i}k}{k_n^y}\sqrt{\frac{\mu}{\epsilon}} H_{0n}\sin\left(\frac{n\pi y}{d_y}\right)\mathrm{e}^{\mathrm{i}(k_n^x x-\omega t)}\hat{\mathbf{e}}_z, \qquad (2.42)
\end{aligned}$$

and

$$\begin{aligned}
\mathbf{H}_\mathrm{t} &= \frac{\mathrm{i}}{\frac{\omega^2\epsilon\mu}{c^2} - (k_n^x)^2}\left(k_n^x \nabla_\mathrm{t} H_x\right) \\
&= \frac{\mathrm{i}k_n^x}{(k_n^y)^2}\partial_y H_x \hat{\mathbf{e}}_y \\
&= -\frac{\mathrm{i}k_n^x}{(k_n^y)^2} H_{0n}\frac{n\pi}{d_y}\sin\left(\frac{n\pi y}{d_y}\right)\mathrm{e}^{\mathrm{i}(k_n^x x-\omega t)}\hat{\mathbf{e}}_y \\
&= -\frac{\mathrm{i}k_n^x}{k_n^y} H_{0n}\sin\left(\frac{n\pi y}{d_y}\right)\mathrm{e}^{\mathrm{i}(k_n^x x-\omega t)}\hat{\mathbf{e}}_y \\
\Longrightarrow\ \mathbf{H} &= \left(\cos\left(\frac{n\pi y}{d_y}\right)\hat{\mathbf{e}}_x - \frac{\mathrm{i}k_n^x}{k_n^y}\sin\left(\frac{n\pi y}{d_y}\right)\hat{\mathbf{e}}_y\right) H_{0n}\mathrm{e}^{\mathrm{i}(k_n^x x-\omega t)}, \qquad (2.43)
\end{aligned}$$

where we used $\omega = ck/\sqrt{\epsilon\mu}$ and

$$k_n^x = \sqrt{k^2 - (k_n^y)^2} = \sqrt{\frac{\omega^2\epsilon\mu}{c^2} - \left(\frac{n\pi}{d_y}\right)^2}. \qquad (2.44)$$

2.5. Wavefunctions in Simulation and Experiment

In this section, we discuss the equivalence between the numerical solution of the 2D Helmholtz equation in a slab geometry described in Ch. 3 and the measurement of the transmission spectra in a 3D rectangular waveguide described in Ch. 4. We show that we can compare the simulated and the measured data by identifying the (scalar) wavefunction as the z-component of the electric field in both cases. Moreover, we find an explicit expression for the latter in the asymptotic region following the theoretical framework from Sec. 2.4. Then, we use this wavefunction to relate the Fisher information flow with the Fisher information operator and show how to control the flow structure within a complex scattering system.

2.5.1. Equivalence between Simulation and Experiment

In the experiment, the probe antenna is oriented parallel to the z-axis, see Fig. 4.3. Consequently, we measure the z-component of the electric field (note that the magnetic field exerts a force perpendicular to the probe antenna). As opposed to Sec. 2.4.3, where we consider a slab system of constant refractive index, we add a region of variable refractive index $\sqrt{\epsilon\mu} = \sqrt{\epsilon\mu}(x, y)$ in the simulation and the experiment. Since we use a piecewise constant function of space for the refractive index, E_z still follows the Helmholtz equation except at the boundaries between two regions of constant $\sqrt{\epsilon\mu}$:

$$
\begin{aligned}
\nabla \times \mathbf{E} &= -\frac{\mu}{c}\partial_t \mathbf{H} \\
\nabla \times \mathbf{H} &= \frac{\epsilon}{c}\partial_t \mathbf{E} \\
&\Downarrow \\
\nabla \times (\nabla \times \mathbf{E}) &= -\frac{1}{c}\partial_t (\nabla \times \mu \mathbf{H}) \\
\nabla (\nabla \cdot \mathbf{E}) - \Delta \mathbf{E} &= -\frac{1}{c}\partial_t (\nabla \mu \times \mathbf{H}) - \frac{\mu}{c}\partial_t \nabla \times \mathbf{H} \\
\nabla \left(\nabla \cdot \left(\epsilon^{-1}\mathbf{D}\right)\right) - \Delta \mathbf{E} &= -\frac{1}{c}\partial_t (\nabla \mu \times \mathbf{H}) - \frac{\epsilon\mu}{c^2}\partial_t^2 \mathbf{E} \\
\nabla \left(\epsilon \left(\nabla \epsilon^{-1}\right) \cdot \mathbf{E}\right) - \Delta \mathbf{E} &= -\frac{1}{c}\partial_t (\nabla \mu \times \mathbf{H}) - \frac{\epsilon\mu}{c^2}\partial_t^2 \mathbf{E} \\
\left(\frac{\epsilon\mu}{c^2}\partial_t^2 - \Delta\right) \mathbf{E} &= -\nabla \left(\epsilon \left(\nabla \epsilon^{-1}\right) \cdot \mathbf{E}\right) - \frac{1}{c}\partial_t (\nabla \mu \times \mathbf{H}) \\
&\Downarrow \\
\left(\frac{\epsilon\mu}{c^2}\partial_t^2 - \Delta\right) E_z &= -\partial_z \left(\epsilon \left(\nabla \epsilon^{-1}\right) \cdot \mathbf{E}\right) + \frac{1}{c}\partial_t \left(\partial_y \mu H_x - \partial_x \mu H_y\right), \qquad (2.45)
\end{aligned}
$$

where the right side is only non-zero at the said boundaries. Since the refractive index does not depend on the z-coordinate, we have $E_z = E_z(x, y)$ and Eq. (2.45) simplifies to a 2D problem. Therefore, we can simulate E_z (except at the boundaries between regions of different refractive index) by solving the 2D Helmholtz

equation and imposing homogeneous Dirichlet boundary conditions at the waveguide walls.

2.5.2. Far-Field Wavefunctions and Scattering Matrix

Let us now derive the wavefunctions in the far field, i.e., far away from the region where the refractive index varies spatially. On the one hand, we do not allow any z-dependence of the wavefunction in the simulation. Therefore, only $\mathrm{TE}_{0,n}$ modes are possible. On the other hand, we have $d_z \ll d_y$ in the experiment and thus only $\mathrm{TE}_{0,n}$ modes are open at low frequencies. In the far field, the refractive index is not a function of space, and the wave propagates freely. Consequently, we can use the results from Sec. 2.4.3 and we obtain for the nth open mode (see Eq. (2.42)):

$$\psi_n \equiv E_z|_{\mathrm{TE}_{0,n}} = A_n \sin\left(\frac{n\pi y}{d_y}\right) \mathrm{e}^{\mathrm{i}(k_n^x x - \omega t)}, \tag{2.46}$$

where we set $A_n = \frac{\mathrm{i}k}{k_n^y}\sqrt{\frac{\mu}{\epsilon}}H_{0n}$. We fix the constant prefactor by normalizing the probability flux through a transverse section of the waveguide[8]:

$$\begin{aligned}
\int \Im\left\{\psi_n^* \nabla\psi_n\right\} \cdot d\mathbf{A} &= \int_0^{d_z} dz \int_0^{d_y} dy\ \Im\left\{\psi_n^* \partial_x \psi_n\right\} \\
&= |A_n|^2 \int_0^{d_z} dz \int_0^{d_y} dy\ \Im\left\{\sin^2\left(\frac{n\pi y}{d_y}\right) \mathrm{i}k_n^x\right\} \\
&= |A_n|^2 k_n^x \int_0^{d_z} dz \int_0^{d_y} dy\ \sin^2\left(\frac{n\pi y}{d_y}\right) \\
&= |A_n|^2 k_n^x \frac{d_y d_z}{2} \\
&\stackrel{!}{=} \tilde{A} \\
\implies A_n &= \sqrt{\frac{2}{d_y k_n^x}}\sqrt{\frac{\tilde{A}}{d_z}} \\
&= \sqrt{\frac{2}{d_y k_n^x}} A,
\end{aligned}$$

where we discarded the physically irrelevant phase factor and redefined the constant as $A = \sqrt{\frac{\tilde{A}}{d_z}}$. Here, A is a real constant factor that depends on how strongly we illuminate the injection antennas in the experiment. In the simulation, we choose $A = 1$. This so-called flux normalization ensures that the probability flux is the same for each open mode.

To consider the most general case, we discuss an arbitrary scattering region that is connected to the asymptotic (i.e., the far-field) region via M straight,

[8] Note that the evanescent modes do not contribute in the asymptotic region and thus $k_n^x \in \mathbb{R}$.

semi-infinite, and rectangular leads of width d_{y_i} (cf. Ref. [15]). Note that we have $M \in \{1, 2\}$ in the simulation from Ch. 3 and $M = 1$ in the experiment from Ch. 4. We introduce a coordinate system in each lead $x_i \in [0, \infty)$, $y_i \in [0, d_{y_i}]$, where x_i is the longitudinal coordinate, and y_i is the transverse coordinate. Choosing that $x_i \to \infty$ corresponds to the boundary between the scattering region and the lead and $x_i = 0$ corresponds to the asymptotic region, we can write the scalar wavefunction in the ith lead as:

$$\psi(x_i, y_i) = \sum_{n=1}^{N_i} \frac{1}{\sqrt{k_{i,n}^x}} \chi_{i,n}(y_i) \left[c_{i,n}^{\text{in}} \mathrm{e}^{\mathrm{i}k_{i,n}^x x_i} + c_{i,n}^{\text{out}} \mathrm{e}^{-\mathrm{i}k_{i,n}^x x_i} \right], \tag{2.47}$$

where we also considered waves propagating in negative x_i-direction.[9] $N_i = \left\lfloor \frac{d_{y_i} k}{\pi} \right\rfloor$ denotes the number of open (flux carrying) modes, and $c_{i,n}^{\text{in}}/c_{i,n}^{\text{out}}$ denote the coefficients of the wavefront going in/coming out of the system. We further defined the transverse mode profiles as:

$$\begin{aligned} \chi_{i,n}(y_i) &= \sqrt{\frac{2}{d_{y_i}}} \sin\left(\frac{n\pi y_i}{d_{y_i}}\right), \\ \int_0^{d_{y_i}} \chi_{i,n}(y_i) \chi_{i,n'}(y_i) dy_i &= \delta_{nn'}. \end{aligned} \tag{2.48}$$

For linear scattering media, the coefficients of the incoming waves $\mathbf{c}^{\text{in}}$ are related to the coefficients of the outgoing waves $\mathbf{c}^{\text{out}}$ via the scattering matrix:

$$\begin{aligned} \mathbf{c}^{\text{in}} &= \begin{pmatrix} \mathbf{c}_1^{\text{in}} \\ \mathbf{c}_2^{\text{in}} \\ \dots \\ \mathbf{c}_M^{\text{in}} \end{pmatrix}, \quad \mathbf{c}_i^{\text{in}} = \begin{pmatrix} c_{i,1}^{\text{in}} \\ c_{i,2}^{\text{in}} \\ \dots \\ c_{i,N_i}^{\text{in}} \end{pmatrix}, \\ \mathbf{c}^{\text{out}} &= \begin{pmatrix} \mathbf{c}_1^{\text{out}} \\ \mathbf{c}_2^{\text{out}} \\ \dots \\ \mathbf{c}_M^{\text{out}} \end{pmatrix}, \quad \mathbf{c}_i^{\text{out}} = \begin{pmatrix} c_{i,1}^{\text{out}} \\ c_{i,2}^{\text{out}} \\ \dots \\ c_{i,N_i}^{\text{out}} \end{pmatrix}, \\ \mathbf{c}^{\text{out}} &= \mathbf{S}\mathbf{c}^{\text{in}} = \begin{pmatrix} \mathbf{S}_{1,1} & \cdots & \mathbf{S}_{1,M} \\ \vdots & \ddots & \vdots \\ \mathbf{S}_{M,1} & \cdots & \mathbf{S}_{M,M} \end{pmatrix} \mathbf{c}^{\text{in}}, \\ \mathbf{c}_i^{\text{out}} &= \sum_{j=1}^{M} \mathbf{S}_{i,j} \mathbf{c}_j^{\text{in}}, \end{aligned} \tag{2.49}$$

[9] In the experiment, the signs in the exponents of the wavefunction are flipped. This is only a different convention, since the physical fields correspond to the real part of the complex fields. To avoid confusion, we will stick to the convention we used until now in the entire text.

where the $\mathbf{S}_{i,j}$ are $N_i \times N_j$ transmission matrices from the jth to the ith lead, and $\mathbf{S}_{i,i}$ is the $N_i \times N_i$ reflection matrix for the ith lead. The vectors and matrices in Eq. (2.49) are written in the so-called mode basis, whose basis functions are the transverse mode profiles from Eq. (2.48). We call $\mathbf{c}^{\text{in}}/\mathbf{c}^{\text{out}}$ the mode composition of the incoming/outgoing wavefront. Note that, because we normalize $\mathbf{c}^{\text{in}} \to \mathbf{c}^{\text{in}}/\|\mathbf{c}^{\text{in}}\|$ and $\mathbf{c}^{\text{out}} \to \mathbf{c}^{\text{out}}/\|\mathbf{c}^{\text{in}}\|$, the wavefunction from Eq. (2.47) is a dimensionless quantity.

2.5.3. Fisher Information Flux in the Asymptotic Region

Using the theoretical framework from the last sections, we can finally show the relation between the Fisher information flow from Eq. (2.21) and the Fisher information operator for the wave from Eq. (2.47). For this, we compute the Fisher information flux, i.e., the integral of the Fisher information flow over a closed surface. Let us start with a small auxiliary calculation:

$$\partial_\theta \psi(x_i, y_i) = \sum_{n=1}^{N_i} \frac{1}{\sqrt{k_{i,n}^x}} \chi_{i,n}(y_i) \partial_\theta c_{i,n}^{\text{out}} \mathrm{e}^{-\mathrm{i}k_{i,n}^x x_i},$$

$$\partial_{x_i}\partial_\theta \psi(x_i, y_i) = -\mathrm{i} \sum_{n=1}^{N_i} \sqrt{k_{i,n}^x} \chi_{i,n}(y_i) \partial_\theta c_{i,n}^{\text{out}} \mathrm{e}^{-\mathrm{i}k_{i,n}^x x_i},$$

where we used that the incoming wave does not depend on θ in the first equality. Since we integrate in the asymptotic region, we can set $x_i = 0$. For convenience, we choose a surface ∂D for the integration which is perpendicular to the x_i-axis in each lead (cf. Fig. 3.4 for $M = 1$). Then:

$$\begin{aligned}
&\int_D \nabla \cdot \mathbf{j}^{\text{FI}} dV \\
&= \int_{\partial D} \mathbf{j}^{\text{FI}} \cdot d\mathbf{A} \\
&= \sum_{i=1}^{M} \int_0^{d_{y_i}} \mathbf{j}^{\text{FI}}(x_i = 0, y_i) \cdot (-\hat{\mathbf{e}}_{x_i}) dy_i \\
&= -\sum_{i=1}^{M} \int_0^{d_{y_i}} \Im \left\{ \partial_\theta \psi(x_i, y_i)^* \nabla \partial_\theta \psi(x_i, y_i) \right\}|_{x_i=0} \cdot -\hat{\mathbf{e}}_{x_i} dy_i \\
&= -\sum_{i=1}^{M} \int_0^{d_{y_i}} \Im \left\{ \partial_\theta \psi(x_i, y_i)^* \partial_{x_i}\partial_\theta \psi(x_i, y_i)) \right\}|_{x_i=0} \, dy_i \\
&= -\sum_{i=1}^{M} \int_0^{d_{y_i}} \Im \left\{ \sum_{n=1}^{N_i} \frac{1}{\sqrt{k_{i,n}^x}} \chi_{i,n}(y_i) \left(\partial_\theta c_{i,n}^{\text{out}}\right)^* \, (-\mathrm{i}) \sum_{n'=1}^{N_i} \sqrt{k_{i,n'}^x} \chi_{i,n'}(y_i) \partial_\theta c_{i,n'}^{\text{out}} \right\} dy_i \\
&= -\sum_{i=1}^{M} \sum_{n=1}^{N_i} \sum_{n'=1}^{N_i} \sqrt{\frac{k_{i,n'}^x}{k_{i,n}^x}} \Im \left\{ -\mathrm{i} \left(\partial_\theta c_{i,n}^{\text{out}}\right)^* \partial_\theta c_{i,n'}^{\text{out}} \right\} \int_0^{d_{y_i}} \chi_{i,n}(y_i) \chi_{i,n'}(y_i) dy_i
\end{aligned}$$

$$
\begin{aligned}
&= -\sum_{i=1}^{M}\sum_{n=1}^{N_i}\sum_{n'=1}^{N_i}\sqrt{\frac{k^x_{i,n'}}{k^x_{i,n}}}\Im\left\{-\mathrm{i}\left(\partial_\theta c^{\mathrm{out}}_{i,n}\right)^* \partial_\theta c^{\mathrm{out}}_{i,n'}\right\}\delta_{nn'} \\
&= \sum_{i=1}^{M}\sum_{n=1}^{N_i}\left(\partial_\theta c^{\mathrm{out}}_{i,n}\right)^* \partial_\theta c^{\mathrm{out}}_{i,n} \\
&= \left(\partial_\theta \mathbf{c}^{\mathrm{out}}\right)^\dagger \partial_\theta \mathbf{c}^{\mathrm{out}} \\
&= \left(\mathbf{c}^{\mathrm{in}}\right)^\dagger \partial_\theta \mathbf{S}^\dagger \partial_\theta \mathbf{S}\mathbf{c}^{\mathrm{in}} \\
&= \left(\mathbf{c}^{\mathrm{in}}\right)^\dagger \mathbf{F}(\theta)\mathbf{c}^{\mathrm{in}},
\end{aligned}
\tag{2.50}
$$

where $\mathbf{F}(\theta)$ is the Fisher information operator in mode basis. By comparison to Eq. (2.10)[10], we deduce that the Fisher information flow describes the information associated to a coherent incoming state locally (up to a trivial factor of 4, which we could easily include in the expression for the Fisher information flow). While we only showed Eq. (2.50) in the far field, it also holds in the near field: from the stationary continuity equation, we have

$$
\int_V \sigma^{\mathrm{FI}} dV = \int_{\partial V} \mathbf{j}^{\mathrm{FI}} \cdot d\mathbf{A} \overset{\text{far field}}{=} \left(\mathbf{c}^{\mathrm{in}}\right)^\dagger \mathbf{F}\mathbf{c}^{\mathrm{in}}.
$$

The first term, and thus the second term, are the same for all volumes containing the entire source term. Since the last term is constant, we deduce that the second equality must also hold in the near field, as long as we choose an integration volumes that contains the entire region where $\sigma^{\mathrm{FI}} \neq 0$. In Fig. 3.5, we visualize this result by plotting the Fisher information flux for different choices of the integration region V.

To obtain the analogous result for the finite-difference Fisher information flow from Sec. 2.3.3, we can replace $\partial_\theta \to \mathcal{D}$ and repeat the derivation leading to Eq. (2.50). We find that

$$
\int_D \nabla \cdot \mathbf{j}^{\mathrm{FI}} dV = \left(\mathbf{c}^{\mathrm{in}}\right)^\dagger \mathbf{F}(\theta_1, \theta_2)\mathbf{c}^{\mathrm{in}},
\tag{2.51}
$$

where

$$
\mathbf{F}(\theta_1, \theta_2) := (\mathcal{D}\mathbf{S})^\dagger \mathcal{D}\mathbf{S}
\tag{2.52}
$$

is the finite-difference Fisher information operator, which is closely related to the discrimination operator introduced in Ref. [2]. Note that, as before,

$$
\mathcal{D}\mathbf{S} = \frac{(\mathbf{S}_2 - \mathbf{S}_1)}{\theta_2 - \theta_1}.
$$

[10] Note that we work in a convenient basis (the mode basis), whereas in Eq. (2.10) we use abstract notation.

2.5.4. Spatial Control of Information

To conclude the discussion in this chapter, we demonstrate how one can control the flow of information within a complex scattering system by tuning the incoming wavefront. Remarkably, we compute the wavefront of interest solely from the scattering matrix and its dependence on the parameter of interest θ, thus not requiring any knowledge of the near field. While we show the calculations for infinitesimal perturbations of θ, they are also valid for the finite-difference case when replacing $\partial_\theta \to \mathcal{D}$.

Controlling the Flow of Information in y-Direction

First, we show how to maximize the amount of information that flows into a desired region at $x_i = 0$, which is where we would place the detector in a technical application. This practice is of interest when using a detector whose sensitivity varies as a function of space. Our approach is inspired by the techniques used in Ref. [16]. For simplicity, we consider a one-leaded geometry ($M = 1$) and omit the indices that label the leads.

To find the optimal wavefront, we transform the scattering matrices corresponding to the unperturbed and the perturbed system from mode into position space. We find the transformation matrices by noting that we can represent an incoming/outgoing wave that consists of N modes either by its (complex) mode composition or by its amplitude and phase at N y-positions. Denoting the state corresponding to the nth incoming/outgoing mode as $|n_{\text{in}}\rangle/|n_{\text{out}}\rangle$ and the state corresponding to a y-coordinate at some fixed x-position as $|y_x\rangle$, we have (see Eq. 2.47):

$$\langle y_x|n_{\text{in}}\rangle = \frac{1}{\sqrt{k^x_{n_{\text{in}}}}}\sqrt{\frac{2}{d_y}}\sin\left(\frac{n_{\text{in}}\pi y}{d_y}\right)e^{ik^x_{n_{in}}x},$$
$$\langle y_x|n_{\text{out}}\rangle = \frac{1}{\sqrt{k^x_{n_{\text{out}}}}}\sqrt{\frac{2}{d_y}}\sin\left(\frac{n_{\text{out}}\pi y}{d_y}\right)e^{-ik^x_{n_{out}}x},$$

where d_y is the waveguide width, and we can compute k^x_n using Eq. 2.44. Since scattering matrices relate the space of incoming mode compositions to the space of outgoing mode compositions, we need to transform their indices differently:

$$\begin{aligned} S_{\tilde{y}_0 y_0} &= \langle \tilde{y}_0|S|y_0\rangle \\ &= \sum_{n_{\text{out}},n_{\text{in}}=0}^{N} \langle \tilde{y}_0|n_{\text{out}}\rangle \langle n_{\text{out}}|S|n_{\text{in}}\rangle \langle n_{\text{in}}|y_0\rangle \\ &= \left(\mathbf{A^{out}}\mathbf{S}\left(\mathbf{A^{in}}\right)^\dagger\right)_{\tilde{y}_0 y_0}, \end{aligned}$$

where $\mathbf{S}$ is the scattering matrix in mode basis at $x = 0$, and we defined the transformation matrices from mode to position space for outgoing/incoming waves

as

$$A^{\text{out}}_{\tilde{y}_0 n_{\text{out}}} = \langle \tilde{y}_0 | n_{\text{out}} \rangle = \frac{1}{\sqrt{k^x_{n_{\text{out}}}}} \sqrt{\frac{2}{d_y}} \sin\left(\frac{n_{\text{out}} \pi \tilde{y}}{d_y}\right),$$
$$A^{\text{in}}_{y_0 n_{\text{in}}} = \langle y_0 | n_{\text{in}} \rangle = \frac{1}{\sqrt{k^x_{n_{\text{in}}}}} \sqrt{\frac{2}{d_y}} \sin\left(\frac{n_{\text{in}} \pi y}{d_y}\right).$$

We use N equally spaced y-positions within the waveguide at $x = 0$ to represent $\mathbf{S}$ in position space, i.e., $y_0, \tilde{y}_0 \in \left\{\frac{1}{N+1} d_y, \frac{2}{N+1} d_y, ..., \frac{N}{N+1} d_y\right\}$. Since we use the same y-coordinates for the dimensions corresponding to the incoming and outgoing waves, we have $\mathbf{A}^{\text{out}} = \mathbf{A}^{\text{in}}$. To maximize the Fisher information flux to a certain subset of these y-coordinates B_y, we define

$$\tilde{S}_{\tilde{y}_0 y_0} \coloneqq \begin{cases} 0 \text{ if } \tilde{y}_0 \notin B_y \\ S_{\tilde{y}_0 y_0} \text{ otherwise} \end{cases}.$$

$\tilde{\mathbf{S}}$ is a scattering matrix in position space of a system, where we only have access to the outgoing wave (and thus to the Fisher information it carries) at the y-coordinates in B_y. We can easily retrieve the corresponding scattering matrix in mode space:

$$\mathbf{S}^{\text{RSA}} \coloneqq \left(\mathbf{A}^{\mathbf{out}}\right)^{-1} \tilde{\mathbf{S}} \left(\left(\mathbf{A}^{\mathbf{in}}\right)^{\dagger}\right)^{-1},$$

from which we can compute the so-called "restricted spatial access (RSA) Fisher information operator":

$$\mathbf{F}^{\text{RSA}} \coloneqq \left(\partial_\theta \mathbf{S}^{\text{RSA}}\right)^{\dagger} \partial_\theta \mathbf{S}^{\text{RSA}}.$$

The maximum eigenstate corresponding to this operator defines the wavefront that yields the maximal Fisher information flux to B_y. We show and discuss the Fisher information flow/source term that results from such a wavefront in Sec. 3.3.1.

Controlling the Flow of Information to a Set of Leads

In this section, we introduce the relative Fisher information operator, which one can use to maximize the percentage of information flowing into a subset of leads $J \subset L$, where we denoted the set of all leads as $L = \{1, 2, ..., M\}$. We use this practice when we only want to communicate with peers at the leads in J while avoiding eavesdroppers at the leads in $L \setminus J$. For simplicity, we assume that we can only send in waves from the ith lead. An example of such a setup is shown in Fig. 2.1 for $|L| = 4$ and $|J| = 1$.

Applying the same reasoning as in Sec. 2.5.3, the Fisher information flowing into the jth lead is

$$\Phi_j = \int_0^{d_{y_j}} \mathbf{j}^{\text{FI}}(x_j = 0, y_j) \cdot (-\hat{\mathbf{e}}_{x_j}) dy_j. \tag{2.53}$$

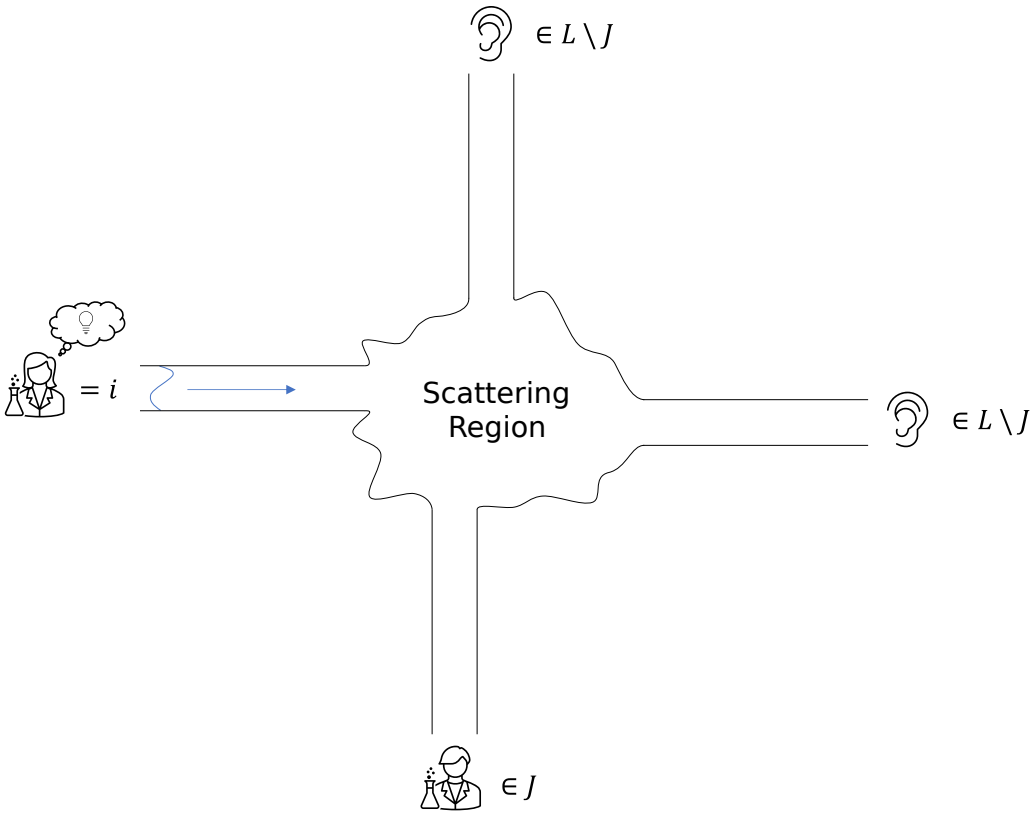

Figure 2.1.: Alice, who sits at the left lead, wants to pass some information to her friend Bob, who sits at the bottom lead. She can only reach him by injecting a wavefront into her waveguide, as indicated by a blue arrow. Unfortunately, the wave needs to pass through a scattering region, which is connected to three more leads. While Bob sits at one of these leads, the other two leads are occupied by eavesdroppers. Using the relative Fisher information operator, Alice can ensure that Bob obtains a maximum percentage of the information.

Similar to the calculation leading to Eq. (2.50), we can simplify this expression:

$$\Phi_j = \sum_{n=1}^{N_j} (\partial_\theta c_{j,n}^{\text{out}})^* \partial_\theta c_{j,n}^{\text{out}}.$$

As for the conventional Fisher information operator, we can rewrite the last identity using the scattering matrix formalism from Eq. (2.49):

$$\begin{aligned}\Phi_j &= \left(\partial_\theta \mathbf{c}_j^{\text{out}}\right)^\dagger \partial_\theta \mathbf{c}_j^{\text{out}} \\ &= \sum_{k\in L} \sum_{k'\in L} \left(\mathbf{c}_{k'}^{\text{in}}\right)^\dagger \left(\partial_\theta \mathbf{S}_{j,k'}\right)^\dagger \partial_\theta \mathbf{S}_{j,k} \mathbf{c}_k^{\text{in}}.\end{aligned}$$

If we assume that we only have access to the ith lead, i.e., we can only send in waves there, we have $\mathbf{c}^{\text{in}}_{k\neq i} = \mathbf{0}$ and thus

$$\begin{aligned}\Phi_{j|i} &= \left(\mathbf{c}^{\text{in}}_i\right)^\dagger \left(\partial_\theta \mathbf{S}_{j,i}\right)^\dagger \partial_\theta \mathbf{S}_{j,i} \mathbf{c}^{\text{in}}_i, \\ &=: \left(\mathbf{c}^{\text{in}}_i\right)^\dagger \mathbf{Q}_{j|i} \mathbf{c}^{\text{in}}_i\end{aligned}$$

where the subscript $j|i$ denotes the Fisher information flowing into the jth lead when we only send in waves from the ith lead. In the second step, we introduced the reduced Fisher information operator in mode space for the jth lead $\mathbf{Q}_{j|i}$. We aim to maximize the relative Fisher information flux to a subset of leads J, i.e.,

$$\max \frac{\sum_{j\in J} \Phi_{j|i}}{\sum_{l\in L} \Phi_{l|i}} = \max_{\mathbf{c}^{\text{in}}_i} \frac{\left(\mathbf{c}^{\text{in}}_i\right)^\dagger \left(\sum_{j\in J} \mathbf{Q}_{j|i}\right) \mathbf{c}^{\text{in}}_i}{\left(\mathbf{c}^{\text{in}}_i\right)^\dagger \left(\sum_{l\in L} \mathbf{Q}_{l|i}\right) \mathbf{c}^{\text{in}}_i}.$$

Note that one could add weights in the last expression to customize the optimization. Since the $\mathbf{Q}_{l|i}$ are non-negative, they have a non-negative square root (see Thm. 1), and we can rewrite the sum in the denominator as[11]

$$\begin{aligned}\left(\mathbf{c}^{\text{in}}_i\right)^\dagger \left(\sum_{l\in L} \mathbf{Q}_{l|i}\right) \mathbf{c}^{\text{in}}_i &= \left(\mathbf{c}^{\text{in}}_i\right)^\dagger \sqrt{\sum_{l'\in L} \mathbf{Q}_{l'|i}} \sqrt{\sum_{l\in L} \mathbf{Q}_{l|i}} \mathbf{c}^{\text{in}}_i \\ &= \mathbf{d}_i^\dagger \mathbf{d}_i,\end{aligned}$$

where we introduced the auxiliary quantity $\mathbf{d}_i \coloneqq \sqrt{\sum_{l\in L} \mathbf{Q}_{l|i}} \mathbf{c}^{\text{in}}_i$ in the second equation. Assuming that the square root is invertible, we can write the relative flux as

$$\max \frac{\sum_{j\in J} \Phi_{j|i}}{\sum_{l\in L} \Phi_{l|i}} = \max_{\mathbf{d}_i} \frac{\mathbf{d}_i^\dagger \sqrt{\sum_{l'\in L} \mathbf{Q}_{l'|i}}^{-1} \left(\sum_{j\in J} \mathbf{Q}_{j|i}\right) \sqrt{\sum_{l\in L} \mathbf{Q}_{l|i}}^{-1} \mathbf{d}_i}{\mathbf{d}_i^\dagger \mathbf{d}_i},$$

which is maximized by the eigenvalue problem

$$\left(\sqrt{\sum_{l'\in L} \mathbf{Q}_{l'|i}}^{-1} \left(\sum_{j\in J} \mathbf{Q}_{j|i}\right) \sqrt{\sum_{l\in L} \mathbf{Q}_{l|i}}^{-1}\right) \mathbf{d}_i = \lambda \mathbf{d}_i. \tag{2.54}$$

[11] Remember that non-negative operators are Hermitian, see Sec. 2.2.

Rewriting the last expression in terms of $\mathbf{c}_i^{\text{in}}$, we find

$$\begin{aligned}
\left(\sqrt{\sum_{l'\in L}\mathbf{Q}_{l'|i}}^{-1}\left(\sum_{j\in J}\mathbf{Q}_{j|i}\right)\right)\mathbf{c}_i^{\text{in}} &= \lambda\sqrt{\sum_{l\in L}\mathbf{Q}_{l|i}}\mathbf{c}_i^{\text{in}} \\
\left(\sqrt{\sum_{l\in L}\mathbf{Q}_{l|i}}^{-1}\sqrt{\sum_{l'\in L}\mathbf{Q}_{l'|i}}^{-1}\left(\sum_{j\in J}\mathbf{Q}_{j|i}\right)\right)\mathbf{c}_i^{\text{in}} &= \lambda\mathbf{c}_i^{\text{in}} \\
\left(\left(\sqrt{\sum_{l\in L}\mathbf{Q}_{l|i}}\sqrt{\sum_{l'\in L}\mathbf{Q}_{l'|i}}\right)^{-1}\left(\sum_{j\in J}\mathbf{Q}_{j|i}\right)\right)\mathbf{c}_i^{\text{in}} &= \lambda\mathbf{c}_i^{\text{in}} \\
\left(\left(\sum_{l\in L}\mathbf{Q}_{l|i}\right)^{-1}\left(\sum_{j\in J}\mathbf{Q}_{j|i}\right)\right)\mathbf{c}_i^{\text{in}} &= \lambda\mathbf{c}_i^{\text{in}} \\
\mathbf{F}_{J|i}\mathbf{c}_i^{\text{in}} &= \lambda\mathbf{c}_i^{\text{in}},
\end{aligned}$$

where we introduced the relative Fisher information operator $\mathbf{F}_{J|i}$ in the last line, whose maximum eigenstate maximizes the relative flux of Fisher information into the leads in J when probing the system from the ith lead. We show the Fisher information flow/source term that results from the wavefront corresponding to such a state in Sec. 3.3.2.

3. Simulation

In this chapter, we discuss the behavior of the Fisher information flow in some interesting 2D scattering geometries using numerical techniques. We treat scalar classical waves, i.e., waves that are solutions of the Helmholtz equation (Eq. (2.18)). For these waves, we can define the Fisher information flow and charge density as in Eq. (2.21)/Eq. (2.24) for infinitesimal/finite perturbations of a parameter of interest θ. In the following, we evaluate the expressions in the finite-difference case by solving the Helmholtz equation for both the unperturbed and the perturbed system numerically. The code for the solution of the Helmholtz equation and the computation of the scattering matrix was written by Matthias Kühmayer based on the finite element software NGSolve, see Refs. [17, 18]. To handle several perturbed versions of the same geometry more conveniently, his code was made object-oriented in the course of this work.

Fig. 3.1 shows the 2D scattering geometry that we investigate in the following. We simulate a system that is infinitely long in x-direction by using perfectly matched layers (see Ref. [19] for details). Since we use hard boundary conditions to border the system in y-direction, we identify the scalar wave with the z-component of the electric field (see Sec. 2.5). In this way, we can compare the simulation data directly to the experimental data from the next chapter, see Sec. 4.5.2. Within the system, we place 60 circular scatterers of radius 2.55 mm and refractive index $n = 1.44$, which corresponds to the refractive index of Teflon. Amidst the resulting complex scattering layer, we place a square-shaped scatterer of side length 2 cm and refractive index $n = 1.44$. We call this scatterer "target scatterer", since we choose the parameter of interest θ as either its x-/y-position or its refractive index.[1] For the ambient material, we use $n = 1$, which corresponds to the refractive index of air. To model global loss in the system, we can add a complex refractive index $n_{\text{glob}}^{\text{add}}$ to the entire scattering region. For the most part of the discussion, we discard the left part of the scattering geometry by closing the system with a hard wall at the dotted line. Then, we retrieve a geometry with one open lead (cf. Fig. 3.4), which suffices to discuss most properties of the Fisher information flow. If we further replace the Teflon target scatterer with a metallic one, we retrieve the 2D projection of the experimental scattering geometry from Fig. 4.2.

Using the scattering system from Fig. 3.1, we discuss where information is created and how waves transport it through a complex system. We demonstrate that information is conserved in Hermitian scattering geometries and discuss the effect

[1] Note that we did not choose a circular target scatterer to better distinguish between the Fisher information source term when estimating the target scatterer's x- and y-position, see Fig. 3.2.

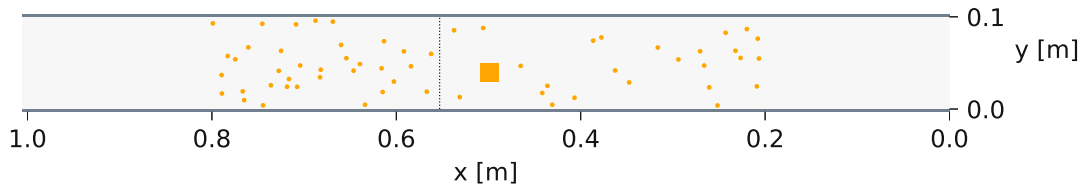

Figure 3.1.: 2D scattering geometry in the simulation. While the system is subject to hard boundary conditions at the top and the bottom side (slate gray lines), it is infinitely long in x-direction. The orange shapes, which we call scatterers, are regions of refractive index $n = 1.44 + n_{\text{glob}}^{\text{add}}$. The large square in the middle of the system corresponds to the target scatterer. We assign $n = 1.0 + n_{\text{glob}}^{\text{add}}$ to the ambient material. Often, we close the system at the dotted line and investigate the resulting one-leaded geometry on the right (cf. Fig. 3.4).

of a global loss term. Then, we show how we can control the flow of information within the system under the constraint that we can only access the far field. Finally, we demonstrate that the Fisher information flow is an entirely new quantity by comparing it to the Poynting vector for a specific example.

We emphasize that we do not perturb the parameter of interest infinitesimally: when estimating the target scatterer's x-/y-position, we shift it for 4.5 mm in positive x-/y-direction. Also, when estimating the target scatterer's refractive index, we increase it by 0.1. Consequently, all figures show the finite-difference Fisher information flow/source term. To keep the text concise, we refer to these quantities as Fisher information flow/source term without explicitly mentioning that we computed them using finite differences.

3.1. Creation of Information

Let us start by investigating the creation of Fisher information. We recall the equations for the Fisher information flow/source term in the scalar classical case (see Eq. (2.24)):

$$\mathbf{j}^{\text{FI}} = \Im\left\{\mathcal{D}\psi^* \nabla \mathcal{D}\psi\right\},$$
$$\sigma^{\text{FI}} = -k^2 \Im\left\{\mathcal{D}n^2 \mathcal{D}\psi^* \psi + \left(\overline{n^2} - 1\right) \mathcal{D}\psi^* \mathcal{D}\psi\right\}.$$

From the stationary continuity equation $\nabla \cdot \mathbf{j}^{\text{FI}} = \sigma^{\text{FI}}$, we see that information can only be created/destroyed in regions where $\sigma^{\text{FI}} > 0 / \sigma^{\text{FI}} < 0$. The source term[2] consists of two contributions:

- The first term is only non-zero at regions where $\mathcal{D}n \neq 0$, i.e., at regions where the system changes with θ. This contribution makes sense intuitively:

[2]Note that we call σ^{FI} source term even though it can also act as a sink when $\sigma^{\text{FI}} < 0$.

we cannot extract information about θ from a system if it does not depend on θ.

- The second term is only non-zero if $\Im\left\{\left(\overline{n^2}-1\right)\right\} \neq 0$. This contribution corresponds to regions where the refractive index has an imaginary part, i.e., regions where the system exhibits gain/loss. In these areas, information that is encoded in the wavefunction via a θ-dependence can be augmented/reduced.

In the following, we visualize the flow and the source term for different parameters of interest and local absorption/gain. For the plots, we choose a frequency of $f = 9.4$ GHz, which corresponds to 6 open modes, i.e., $\mathrm{TE}_{0,n}$, $n \leq 6$ (see Eq. (2.41) for $d_y = 0.1$ m).

3.1.1. Hermitian Systems

First, we investigate systems without gain or loss. In these geometries, only the first term of σ^{FI} contributes. We consider three different parameters: the x-/y-position of the target scatterer and its refractive index. For the corresponding perturbations, we have $\mathcal{D}n \neq 0$ at

- the left and the right boundary of the target scatterer when $\theta = x_{\mathrm{scat}}$.
- the top and the bottom boundary of the target scatterer when $\theta = y_{\mathrm{scat}}$.
- within the target scatterer when $\theta = n_{\mathrm{scat}}$.

Here $x_{\mathrm{scat}}/y_{\mathrm{scat}}$ denotes the x-/y-position of the target scatterer, and n_{scat} denotes its refractive index. In Fig. 3.2, we show the Fisher information flow/source term corresponding to the minimum and maximum eigenstates of the Fisher information operator for these three choices of θ. From the relative scale of the vector plots, we deduce that the flows corresponding to the minimum eigenstates are about three orders of magnitude smaller than the flows corresponding to the maximum eigenstates.

As expected, we observe that information originates at the target scatterer's boundaries when estimating its position (Figs. 3.2a and 3.2b) and in the target scatterer's interior when estimating its refractive index (Fig. 3.2c). Note that information can also be destroyed in these areas ($\sigma^{\mathrm{FI}} < 0$). Consequently, not all information reaches the asymptotic region, even when injecting the optimal probe state. This is due to the low frequency, which leads to a low number of degrees of freedom; therefore, we cannot control the wave perfectly in the areas of variable refractive index, and negative contributions to the source term occur.

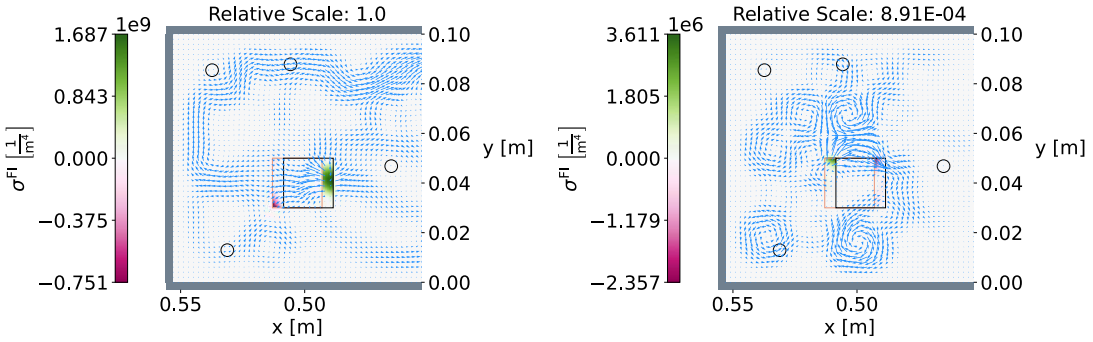

(a) $\theta = x_{\mathrm{scat}}$

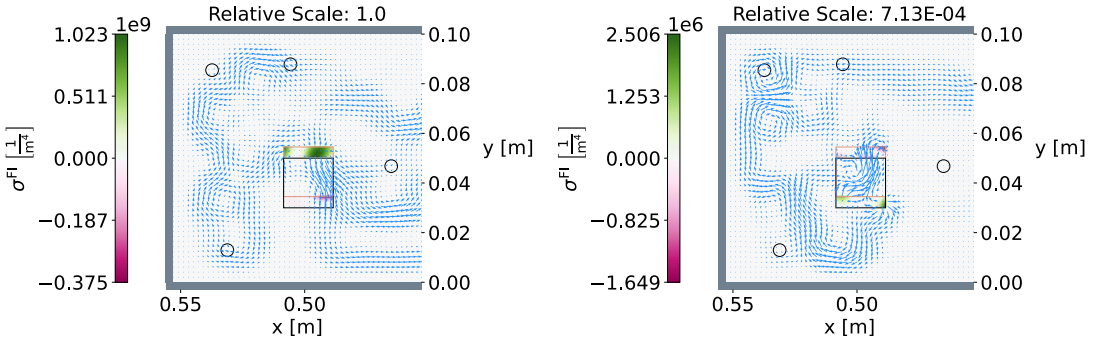

(b) $\theta = y_{\mathrm{scat}}$

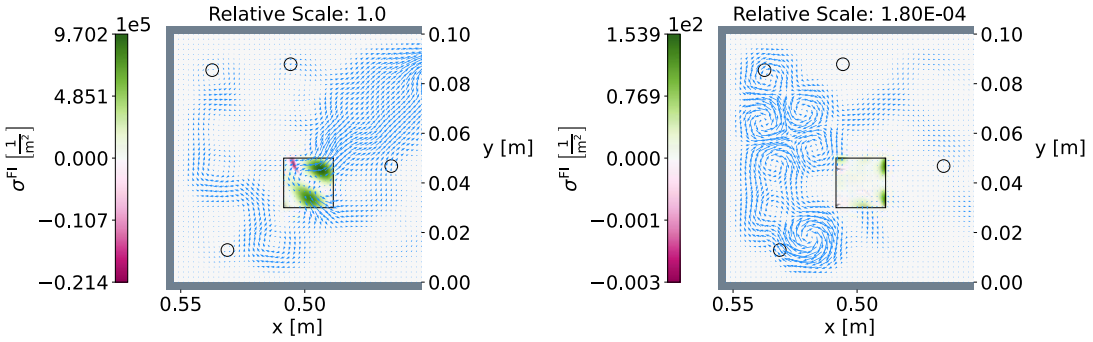

(c) $\theta = n_{\mathrm{scat}}$

Figure 3.2.: Simulated Fisher information flow (blue arrows) and source term (green/pink colors in the background) in the scattering geometry from Fig. 3.4 for three different parameters of interest (no absorption/gain). We choose $f = 9.4$ GHz and show the flow and the source term corresponding to the maximum/minimum eigenvalue of the Fisher information operator on the left/right. Above the figures, we denote the relative scale of the vector plots. In (a)/(b) we estimate the target scatterer's x-/y-coordinate. The position of the target scatterer in the perturbed geometry is indicated by a salmon-colored square. In (c), we estimate the target scatterer's refractive index. We observe that information originates where the refractive index changes upon perturbation, i.e., at the target scatterer's boundaries when estimating its position and in its interior when estimating its refractive index. Note that the unit of σ^{FI} depends on the unit of θ, see Eq. (2.22).

3.1.2. Non-Hermitian Systems

In this section, we analyze the behavior of information in systems that exhibit local gain or loss. We add a square region of refractive index $n_{\text{loc}} = \pm 5 \cdot 10^{-2}$ i at $x = 0.31$ m in the scattering layer of the one-leaded geometry from Fig. 3.4. Note that a negative imaginary part corresponds to gain, and a positive imaginary part corresponds to loss. Figure 3.3 shows the maximum Fisher information flows/source terms for the two systems when estimating the target scatterer's refractive index. We see that both terms of σ^{FI} contribute: information originates within the target scatterer and is amplified/reduced in the region where we added the gain/loss. Since we inject the maximum information state into the system, the flow aims to pass through/avoid the area of gain/loss. If we were to increase the frequency such that there are more open modes and thus more degrees of freedom, we would observe that the flow passes through/avoids the square entirely.

Integrating the data from Fig. 3.3, we can validate the stationary continuity equation numerically, i.e., we can check the relation

$$\int_V \sigma^{\text{FI}} dV = \int_{\partial V} \mathbf{j}^{\text{FI}} \cdot d\mathbf{A}.$$

Since the system is two-dimensional, the volume integral of the source term becomes a surface integral and the surface integral of the flow becomes a line integral. We choose an integration path $\partial V_{x=0.28\text{ m}}$ that is parallel to the y-axis when passing through the waveguide at $x = 0.28$ m, cf. Fig. 3.4. Then, the integral of the Fisher information flow is given by Eq. 3.1, and we evaluate the latter numerically using 7500 equally spaced points in y-direction. To check the continuity equation, we must integrate σ^{FI} over the region that is enclosed by $\partial V_{x=0.28\text{ m}}$. Since the source term is 0 on the outside of the waveguide, we only need to consider $\{(x, y) | 0.28\text{ m} \leq x \leq 0.553\text{ m} \wedge 0.0\text{ m} \leq y \leq 0.1\text{ m}\}$. To evaluate the integral of the source term numerically, we discretize this region using a grid of 20500 equally spaced points in x-direction and 7500 equally spaced points in y-direction. We find:

Fig. 3.3a :

$$\frac{\left| \int_{V_{x=0.28\text{ m}}} \sigma^{\text{FI}} dV - \int_{\partial V_{x=0.28\text{ m}}} \mathbf{j}^{\text{FI}} \cdot d\mathbf{A} \right|}{\int_{V_{x=0.28\text{ m}}} \sigma^{\text{FI}} dV} \approx 1.1 \cdot 10^{-4},$$

Fig. 3.3b :

$$\frac{\left| \int_{V_{x=0.28\text{ m}}} \sigma^{\text{FI}} dV - \int_{\partial V_{x=0.28\text{ m}}} \mathbf{j}^{\text{FI}} \cdot d\mathbf{A} \right|}{\int_{V_{x=0.28\text{ m}}} \sigma^{\text{FI}} dV} \approx 1.3 \cdot 10^{-4}.$$

The relative deviation could be decreased further by evaluating the quantities on a finer grid.

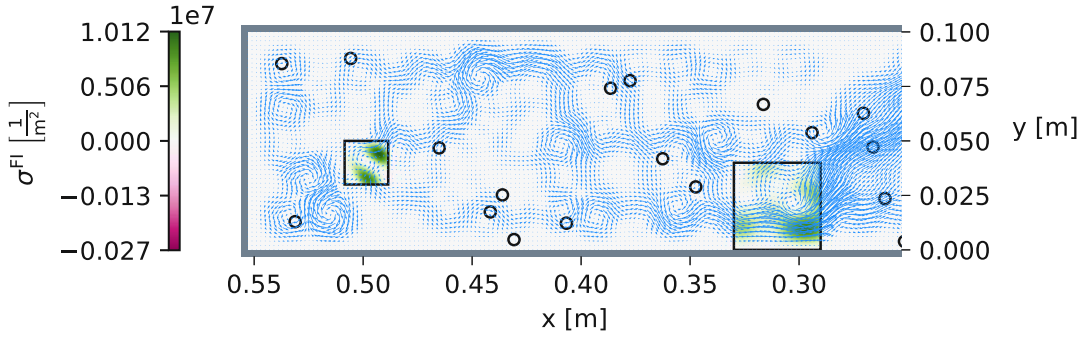

(a) System with local gain $n_{\mathrm{loc}} = -5 \cdot 10^{-2}$ i

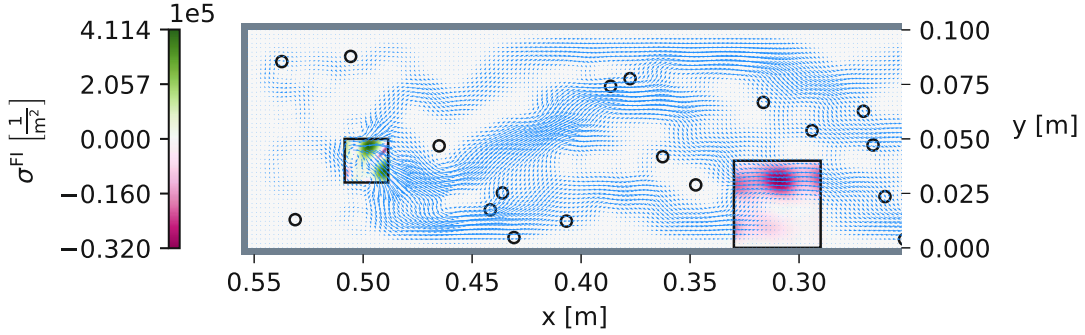

(b) System with local loss $n_{\mathrm{loc}} = 5 \cdot 10^{-2}$ i

Figure 3.3.: Simulated Fisher information flow (blue arrows) and source term (green/pink colors in the background) when adding a square region of local gain (a)/loss (b) at $x = 0.31$ m to the scattering geometry from Fig. 3.4. We show the flow/source term corresponding to the maximum eigenvalue of the Fisher information operator at $f = 9.4$ GHz when estimating the target scatterer's refractive index. Information is created within the target scatterer (i.e., where the system changes when perturbing the parameter of interest) and amplified (a)/reduced (b) in the region of local gain/loss. While the flow accurately passes through the region of gain, it does not avoid the region of loss entirely due to the low number of open modes.

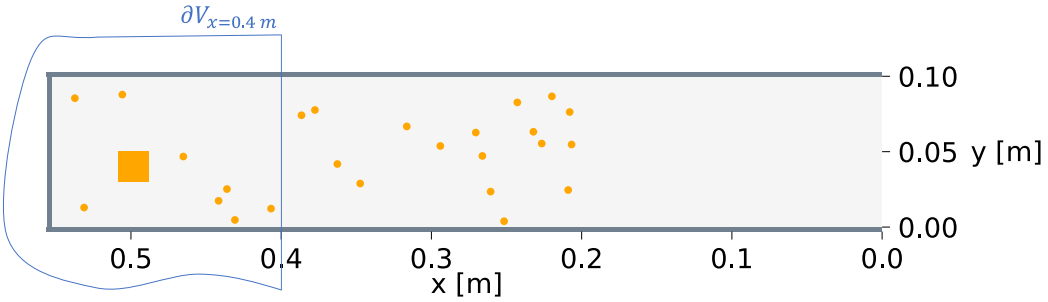

Figure 3.4.: Integration path when evaluating the surface integral of the Fisher information flow at $x = 0.4$ m (blue curve). The scattering geometry corresponds to the one from Fig. 3.1 when we close the latter at the dotted line. Note that we inject waves on the right side (i.e., at $x = 0$ m) of the geometry.

3.2. Global Absorption Effects

In this section, we discuss how global loss affects Fisher information. We show that the latter is conserved in Hermitian (i.e., lossless) geometries and demonstrate how loss can influence the optimal path of information through a complex scattering system. This discussion is of particular interest to us since the experimental setup from Ch. 4 is prone to a global loss term, see Sec. 4.2.3.

To quantify the amount of information created in a region, we use the Fisher information flux, i.e., the surface integral of the Fisher information flow $\int_{\partial V} \mathbf{j}^{\mathrm{FI}} \cdot d\mathbf{A}$. In 2D, the surface integral becomes a line integral. We choose an integration path ∂V_x that is parallel to the y-axis when passing through the waveguide to determine the amount of information at a given x-position, see Fig. 3.4. Note that the wavefunctions (and thus the flows) are 0 outside the waveguide. Therefore, we only need to evaluate the part of the integral that intersects the system, and the surface integral simplifies to

$$\int_{\partial V_{\tilde{x}}} \mathbf{j}^{\mathrm{FI}}(x, y) \cdot d\mathbf{A} = -\int_{y=0}^{0.1} j_x^{\mathrm{FI}}(\tilde{x}, y) dy, \tag{3.1}$$

where j_x^{FI} denotes the x-component of the Fisher information flow.

In the following, we evaluate these integrals at different x-positions to show the relation between the Fisher information flow and the Fisher information operator, i.e. (see Sec. 2.5.3):

$$\int_V \sigma^{\mathrm{FI}} dV = \int_{\partial V} \mathbf{j}^{\mathrm{FI}} \cdot d\mathbf{A} = \left(\mathbf{c}^{\mathrm{in}}\right)^{\dagger} \mathbf{F} \mathbf{c}^{\mathrm{in}},$$

where the last equality holds as long as we choose an integration path that encompasses the entire region where $\sigma^{\mathrm{FI}} \neq 0$. We use the scattering geometry from Fig. 3.4 and estimate the target scatterer's refractive index at $f = 9.4$ GHz.

Figure 3.5a/Figure 3.5b shows the flow and the logarithmic source term for a Hermitian/absorptive system. To simulate the absorptive case, we add a refractive index of $n_{\mathrm{glob}}^{\mathrm{add}} = 10^{-3}$ i to the entire system. We depict the logarithmic source term, i.e.,[3]

$$\mathrm{f}\left(\left\{\sigma^{\mathrm{FI}}\right\}\right) = \mathrm{sgn}\left(\left\{\sigma^{\mathrm{FI}}\right\}\right) \ln\left(\left|\left\{\sigma^{\mathrm{FI}}\right\}\right| + 1\right),$$

since the contribution to σ^{FI} from the global loss is several orders of magnitude smaller than the contribution from within the target scatterer. Figure 3.5c shows the fluxes for both the Hermitian and the absorptive geometry as a function of x. We normalize the flux with respect to the expectation value of the Fisher information operator.[4] Note that the Fisher information operator, and thus the normalization factor, changes when adding a global loss. In Fig. 3.5a, $\sigma^{\mathrm{FI}} \neq 0$ only within the target scatterer. Therefore, the corresponding flux is equal to the expectation value of the Fisher information operator at x-coordinates on the right of the target scatterer. In Fig. 3.5b, $\sigma^{\mathrm{FI}} \neq 0$ in the entire system and we observe a decrease of the corresponding flux towards the expectation value of the Fisher information operator at $x = 0$ m.

Since we only add a small loss term in Fig. 3.5, the flow structure does not change significantly compared to the Hermitian case. For larger absorptions, however, we observe an interesting feature of the maximum information flow: it tends to reduce its path length when traveling to the asymptotic region, entailing that the information it carries is less prone to loss. This can nicely be seen when using a metallic target scatterer like in the experiment from Ch. 4 and choosing $\theta = x_{\mathrm{scat}}$. In Fig. 3.6, we show the maximum information flows for different absorption strengths at $f = 6.9$ GHz, which corresponds to one of the frequencies we used in the experiment. Note that we do not show the source term since it is ill-defined for metallic target scatterers due to their infinite refractive index. At low values of the loss, the wave mainly extracts information at the rear (i.e., left) side of the target scatterer. However, once we increase the loss above a certain threshold, information originates primarily on the front (i.e., right) side of the target scatterer to avoid being subject to absorption when traveling around it.

[3] Here, $\left\{\sigma^{\mathrm{FI}}\right\} := \sigma^{\mathrm{FI}} / \left[\sigma^{\mathrm{FI}}\right]$ denotes the dimensionless source term.

[4] Note that the expectation value of a Fisher information eigenstate is the corresponding eigenvalue.

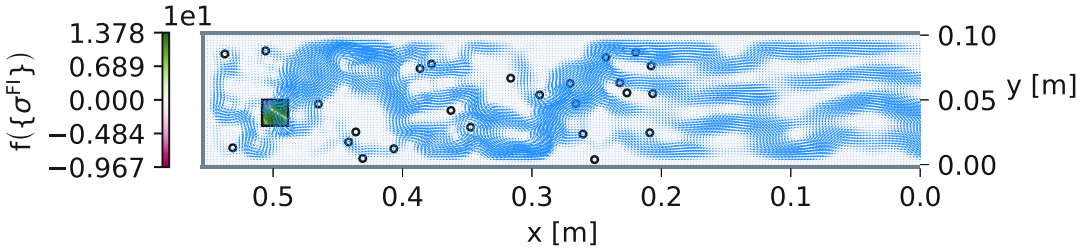

(a) Flow/source term for the Hermitian system

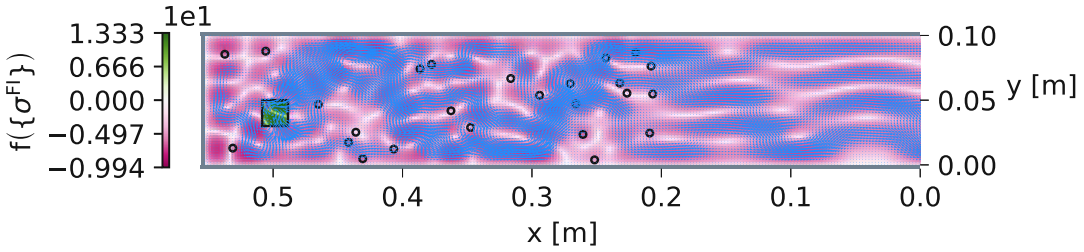

(b) Flow/source term for the system with global loss

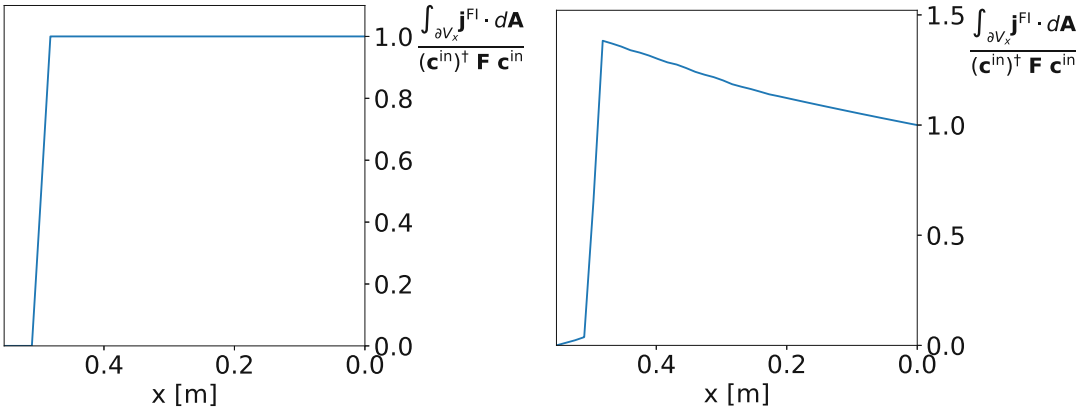

(c) Fluxes for the system without (left) and with (right) global loss

Figure 3.5.: Simulated Fisher information flow/source term/flux corresponding to the maximum eigenstate of the Fisher information operator in the scattering geometry from Fig. 3.4 for $f = 9.4$ GHz and $\theta = n_{\text{scat}}$. The plots in (a) and (b) show the flow (blue arrows) and the logarithmic source term (green/pink colors in the background). While we use a Hermitian geometry in (a), we add a complex refractive index of $n_{\text{glob}}^{\text{add}} = 10^{-3}$ i to the entire system in (b). In (c), we show the normalized Fisher information flux as a function of x for both systems. Since we only add a small loss term, the structure of the flow does not change significantly when going from (a) to (b). However, the corresponding fluxes deviate in the two cases: while we observe a constant flux in the Hermitian geometry, we find a decrease of the flux towards the expectation value of the Fisher information operator in the absorptive geometry.

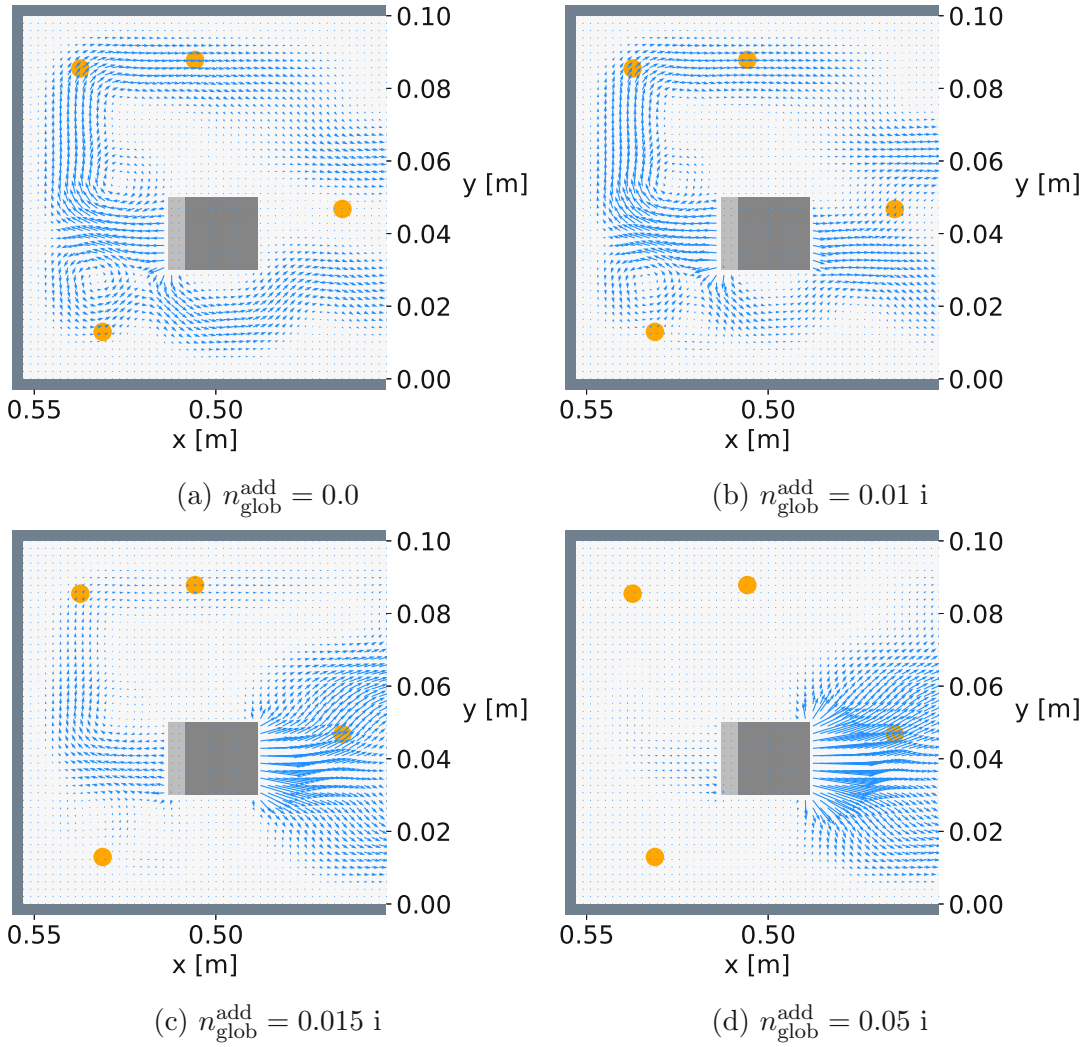

(a) $n_{\text{glob}}^{\text{add}} = 0.0$

(b) $n_{\text{glob}}^{\text{add}} = 0.01$ i

(c) $n_{\text{glob}}^{\text{add}} = 0.015$ i

(d) $n_{\text{glob}}^{\text{add}} = 0.05$ i

Figure 3.6.: Transition of the simulated maximum information flow (blue arrows) when varying $n_{\text{glob}}^{\text{add}}$ at $f = 6.9$ GHz. We use a metallic target scatterer (dark gray square) and choose $\theta = x_{\text{scat}}$. The gray rectangle indicates the shift of the target scatterer when we perturb the system. As before, we assign a refractive index of $n = 1.44$ to the other scatterers (orange circles). Going from (a)-(d), we increase the global absorption strength and observe that information originates more and more on the target scatterer's right side. Since this side is closer to the asymptotic region, the length of the information's path through the lossy system is reduced. Consequently, less information is absorbed, and we can retrieve more of it in the asymptotic region.

3.3. Spatial Control of Information

To conclude this chapter, we implement the techniques from Sec. 2.5.4. There, we showed how to control the flow of information within a scattering system by tuning the incoming wavefront. We emphasize that we do not require any knowledge of the near field for the design of the incoming state. Rather, we compute the latter from the scattering matrix and its dependence on the parameter of interest θ. To attain a satisfactory level of control over the wave, we require more degrees of freedom than in the previous sections. Therefore, we work at higher frequencies.

3.3.1. Controlling the Flow of Information in y-Direction

First, we show how to focus the flow of information in a desired part of the asymptotic region. In Sec. 2.5.4, we showed that the wavefront that maximizes the flow of information to a subset of y-coordinates $B_y \subset \{\frac{1}{N+1}d_y, \frac{2}{N+1}d_y, ..., \frac{N}{N+1}d_y\}$ corresponds to the maximum eigenstate of the restricted spatial access Fisher information operator $\mathbf{F}^{\mathrm{RSA}}$. Note that increasing the number of open modes N not only gives us more freedom in designing the incoming wavefront but also improves the spatial resolution of the target region B_y.

For the demonstration of the techniques, we use the geometry with one open lead from Fig. 3.4 and $\theta = n_{\mathrm{scat}}$. We choose $f = 30.4$ GHz, which corresponds to 20 open modes, i.e., $\mathrm{TE}_{0,n}$, $n \leq 20$.[5] Fig. 3.7a/3.7b shows the flow corresponding to the maximum eigenstate of $\mathbf{F}^{\mathrm{RSA}}$ when choosing $B_y = \{y|y \geq 0.05 \text{ m}\}/B_y = \{y|y \leq 0.05 \text{ m}\}$, where d_y is the waveguide width. As desired, most Fisher information flows to the top/bottom half of the waveguide at $x = 0$ m in the first/second case. When comparing the information flowing up/down of the RSA and the conventional maximum information flows, we see that the flux to the target region is significantly higher for the RSA states:

$$\frac{\int_{y=0.05}^{0.1} j_x^{\mathrm{FI}\uparrow}(x=0,y)dy}{\int_{y=0.05}^{0.1} j_x^{\mathrm{FI}}(x=0,y)dy} \approx 1.56,$$
$$\frac{\int_{y=0}^{0.05} j_x^{\mathrm{FI}\downarrow}(x=0,y)dy}{\int_{y=0}^{0.05} j_x^{\mathrm{FI}}(x=0,y)dy} \approx 1.42.$$

Here, j_x^{FI} denotes the flow corresponding to the maximum eigenstate of $\mathbf{F}$, and $j_x^{\mathrm{FI}\uparrow}/j_x^{\mathrm{FI}\downarrow}$ denotes the flow corresponding to the maximum eigenstate of $\mathbf{F}^{\mathrm{RSA}}$ for $B_y = \{y|y \geq 0.05 \text{ m}\}/B_y = \{y|y \leq 0.05 \text{ m}\}$.

[5] In the experiment from Ch. 4, $\mathrm{TM}_{m,n}$ and $\mathrm{TE}_{m,n}$ modes would also be possible for $m \geq 0$ at this frequency. Consequently, one could not use the theoretical framework from Sec. 2.5 to find the optimal wavefront. To implement the methods we present in this section experimentally, one would have to either adapt the theory or decrease the height of the waveguide to maintain a quasi-2D system.

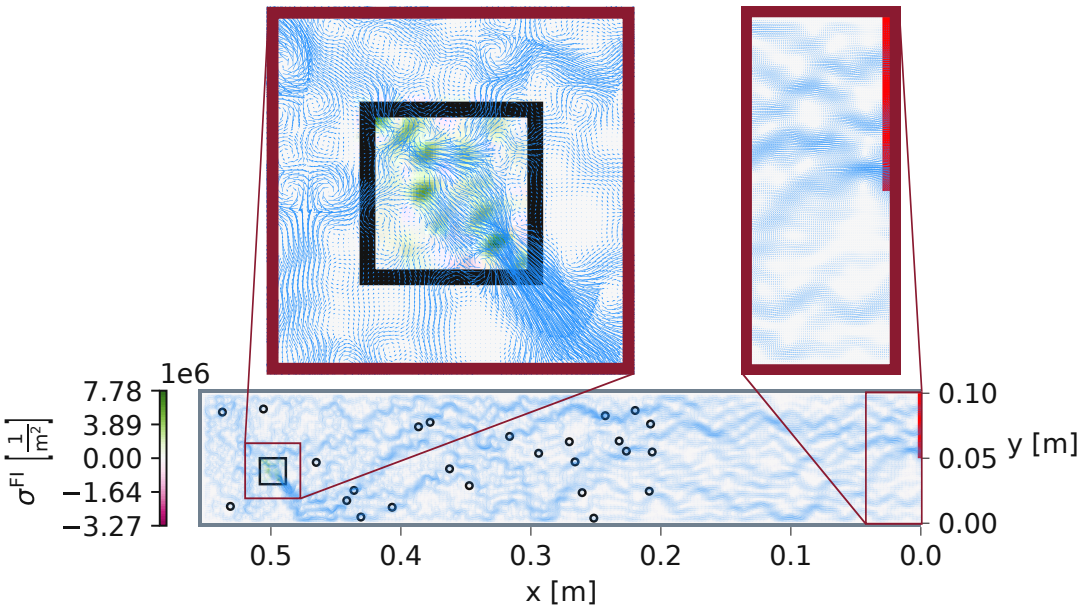

(a) $B_y = \{y | y \geq 0.05 \text{ m}\}$

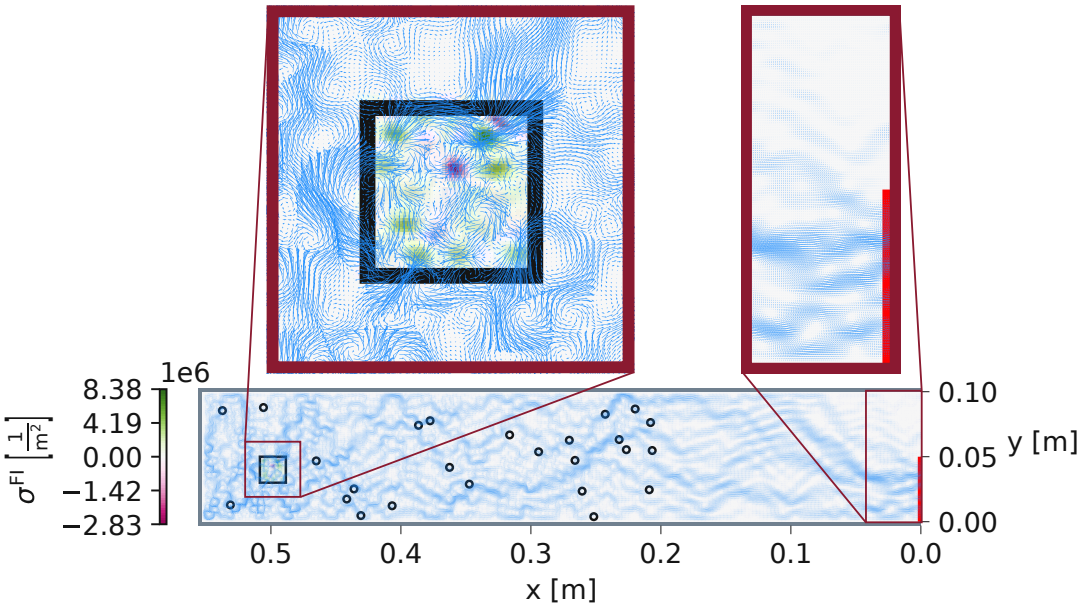

(b) $B_y = \{y | y \leq 0.05 \text{ m}\}$

Figure 3.7.: Simulated Fisher information flow (blue arrows) and source term (green/pink colors in the background) corresponding to the maximum eigenstate of the restricted access Fisher information operator $\mathbf{F}^{\mathrm{RSA}}$ at $f = 30.4$ GHz. We use a Hermitian system and estimate the refractive index of the target scatterer. Since the frequency is higher than for the previous plots, the flow changes on a smaller length scale. In (a)/(b), we choose the target region (bright red bar) as the upper/lower half of the waveguide and observe that the Fisher information flow gets focused in these areas at $x = 0$ m. The flow/source term around the target scatterer and in the far field is shown in greater detail in the dark red boxes.

3.3.2. Controlling the Flow of Information to a Set of Leads

In this section, we use the scattering geometry with two open leads from Fig. 3.1 and choose $\theta = n_{\text{scat}}$. We constrain our access to the right lead and imagine that a spy sits at the left lead, eager to collect all Fisher information that comes his way. When probing the system, we want to reveal as little as possible to the spy while learning as much as we can about θ. To achieve this task, we can use the relative Fisher information operator from Sec. 2.5.4, i.e.:

$$\mathbf{F}_{J|i} = \left(\sum_{l\in L} \mathbf{Q}_{l|i}\right)^{-1} \left(\sum_{j\in J} \mathbf{Q}_{j|i}\right),$$

where

$$\mathbf{Q}_{j|i} = (\partial_\theta \mathbf{S}_{j,i})^\dagger \, \partial_\theta \mathbf{S}_{j,i},$$

and L denotes the set of all leads. The maximum eigenstate of this operator maximizes the relative flux of Fisher information to a subset J of leads, when we probe the system from the ith lead. If we label the leads with l for the left and r for the right lead, we have

$$\begin{aligned} L &= \{l, r\}, \\ J &= \{r\}, \\ i &= r, \end{aligned}$$

and the relative Fisher information operator simplifies to

$$\mathbf{F}_{\{r\}|r} = \left((\partial_\theta \mathbf{S}_{r,r})^\dagger \, \partial_\theta \mathbf{S}_{r,r} + (\partial_\theta \mathbf{S}_{l,r})^\dagger \, \partial_\theta \mathbf{S}_{l,r}\right)^{-1} \left((\partial_\theta \mathbf{S}_{r,r})^\dagger \, \partial_\theta \mathbf{S}_{r,r}\right),$$

where $\mathbf{S}_{r,r}$ denotes the reflection matrix of the right lead and $\mathbf{S}_{l,r}$ denotes the transmission matrix from the right to the left lead. Figure 3.8a shows the Fisher information flow corresponding to the maximum eigenstate of $\mathbf{F}_{\{r\}|r}$. We choose $f = 11.8$ GHz, which corresponds to 7 open modes, i.e. $\text{TE}_{0,n}$, $n \leq 7$. Note that we do not require as many degrees of freedom as in Sec. 3.3.1. We see that the relative Fisher information operator enables us to design an incoming state that penetrates the system from the right and transports almost all information back to where it came from. More concretely, we have

$$\frac{\Phi_r}{\Phi_l + \Phi_r} \approx 98.41\%,$$

where Φ_r/Φ_l denotes the flux of information to the right/left lead, see Eq. (2.53).

Fisher Information Flow and Poynting Vector

To conclude this section, we use the maximum eigenstate of $\mathbf{F}_{\{r\}|r}$ to show that the flow of energy (described by the Poynting vector) and the flow of information (described by the Fisher information flow) are fundamentally distinct quantities. For completeness, let us state the definition of the Poynting vector for scalar classical waves:

$$\mathbf{j}^{\mathrm{P}} = \Re\left\{\mathrm{i}\psi\nabla\psi^{*}\right\}.$$

Since most of the information returns to the right lead, it seems intuitive that most of the energy should follow a similar path. However, the Poynting vector, which we plot in Fig. 3.8b, has an entirely different structure than the Fisher information flow from Fig. 3.8a: while most of the information flows back to our lead, a large part of the energy passes through the system and reaches the spy. We conclude that, while the spy knows that we probe the system, he can only deduce very little about the value of θ from his measurements. This comparison shows that the Fisher information flow is a new quantity that enables us to understand electromagnetic waves on a more fundamental level.

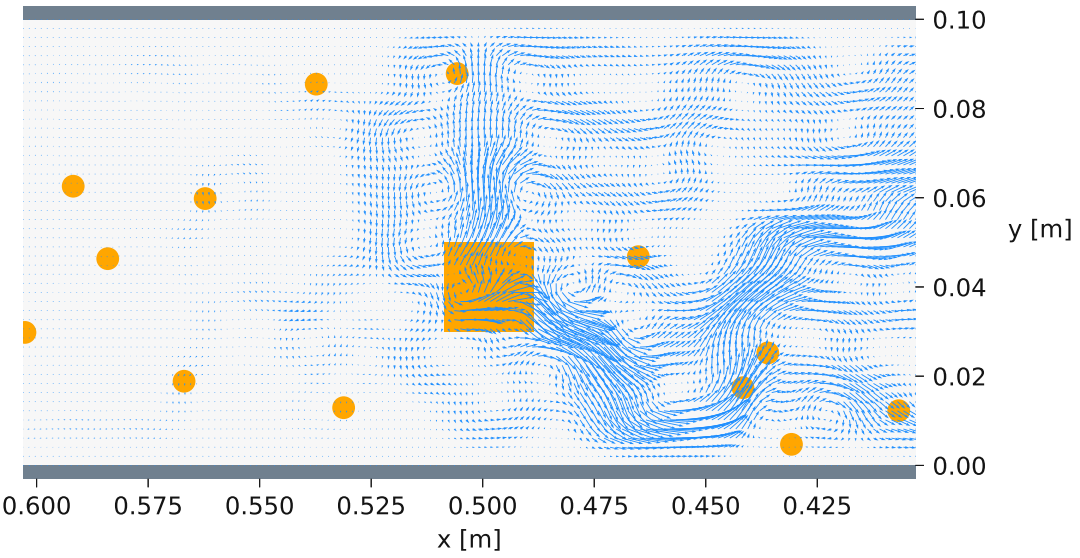

(a) Fisher information flow

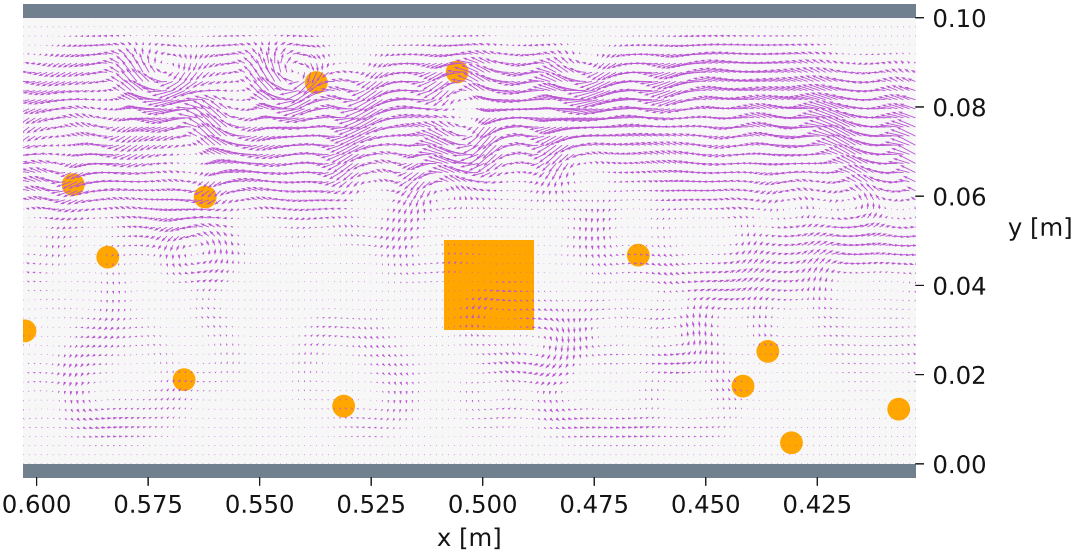

(b) Poynting vector

Figure 3.8.: Simulated Fisher information flow (blue arrows in (a)) and Poynting vector (orchid arrows in (b)) for the maximum eigenstate of the relative Fisher information operator $\mathbf{F}_{\{r\}|r}$ at $f = 11.8$ GHz. We use the scattering system with two open leads from Fig. 3.1 and estimate the target scatterer's refractive index. Note that we probe the system from the right side. While most of the wave's energy is transmitted to the spy lead in the left (b), almost no information reaches the latter (a).

4. Experiment

In this chapter, we discuss the measurements of the Fisher information flow, which were performed at Université Côte d'Azur in the course of this work. We present the experimental setup, explain the data processing, and discuss the measurement results. The experimental/data processing techniques that we use are inspired by Ref. [20]. Although the derivatives with respect to space and the parameter of interest in the expression for the Fisher information flow complicate the experiment (see Sec. 4.4), we achieve remarkable precision in our measurements. Our results show that the Fisher information flow is accessible in practical applications, which makes it an even more powerful tool.

4.1. Experimental Setup

To give the reader as much insight as possible, we show the experimental setup from three different perspectives: Fig. 4.1 shows a photo, Fig. 4.2 shows a sketch of the top view with and without the top plate, and Fig. 4.3 compares the cross section in the x-z-plane for the two types of measurements we perform (i.e., far-field and near-field measurement). In the following, we gradually discuss all components of the setup and reference the figures that show them the most clearly.

We work with a rectangular aluminum waveguide of length 1.1 m (x-direction) and inner width 0.1 m (y-direction). While we close the system on the left at $x = 0.553$ m with a piece of aluminum, we place absorbing material on the right to imitate an infinitely long waveguide, see Fig. 4.2. Due to our choice of one of the probe antennas, which we discuss in more detail later in the text, the system is slightly higher on the left (i.e., 11 mm for $0.553\ \text{m} \geq x \geq 0.453$ m) than on the right (i.e., 8 mm for $x \leq 0.453$ m), see Fig. 4.3.

Within the waveguide, we place 1 cuboid aluminum and 25 cylindrical Teflon scatterers, see Fig. 4.2b for their arrangement. We call the metallic scatterer "target scatterer" since we choose the parameter of interest θ as either its x-position ($\theta = x_{\text{scat}}$) or its y-position ($\theta = y_{\text{scat}}$). Note that this scatterer is higher (11 mm) than the Teflon scatterers (8 mm), see Fig. 4.3. To create a perturbation of θ, we shift the target scatterer in positive x- or y-direction for 4.5 mm. This shift can be executed precisely since we fix the scatterer's position with a pin in the bottom plate of the waveguide.

To determine the microwave field for a given incoming state, we measure the transmission from port 2 to port 1 of a vector network analyzer (VNA). We denote

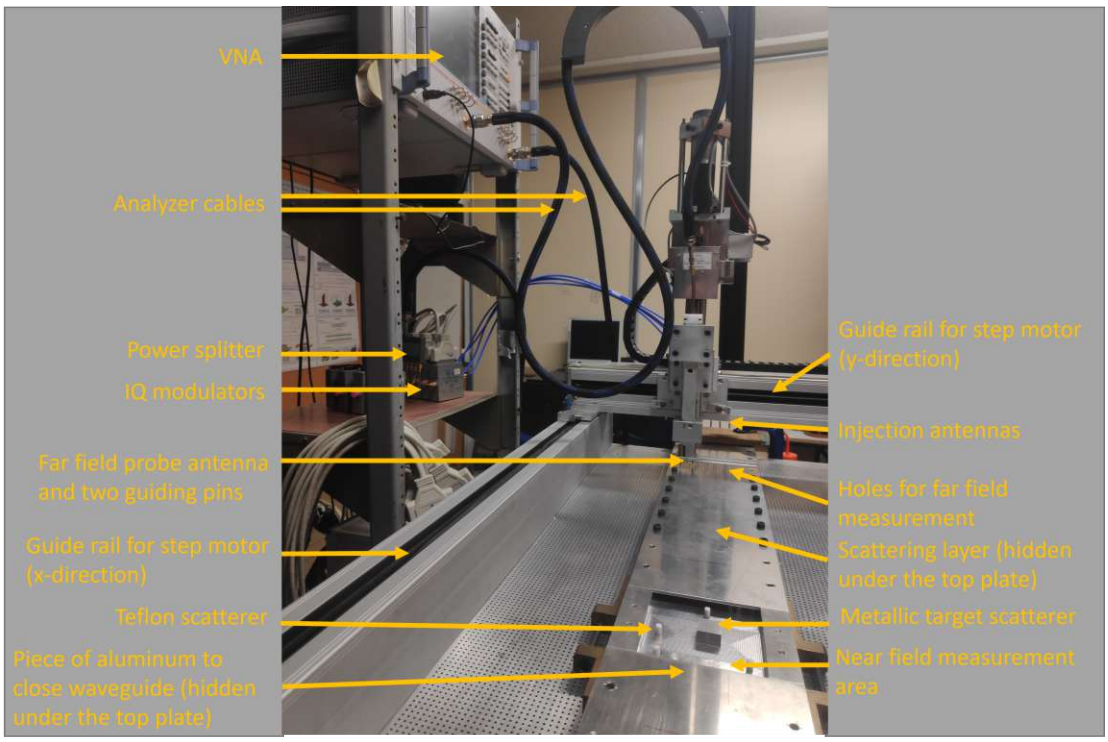

Figure 4.1.: Photo of the experimental setup with the top plate. Here, the far-field probe antenna is connected to the VNA. Before performing a measurement, we close the near field measurement area with a metal plate, which we press against the waveguide using weights. While the Teflon scatterers are white, we depict them in orange in Figs. 4.2 and 4.3 for better visibility.

the transmission spectra as $S_{12}(f)$, where f is the frequency.[1] Port 1 of the VNA is connected to a probe antenna, which we position using three step motors, see Fig. 4.1. Port 2 is connected to four injection antennas that reach 3 mm into the system via a power splitter and four IQ modulators, see Figs. 4.2 and 4.3. Both probe and injection antennas couple weakly to the system. Note that the calibration points of the VNA are at the end of the analyzer cables, i.e., the cables connecting the VNA and the power splitter/probe antenna (see Fig. 4.1). We control the incoming state by choosing the relative phase (0 to 2π) and the attenuation (0 to 40 dB) of the IQ modulators. The corresponding field can be measured in two different regions:

- About 20 cm away from the scattering region (i.e., 0 m $\leq x \leq$ 0.025 m), we can probe the field via 6×19 evenly spaced holes in the top plate of the waveguide (distance of 5 mm from center to center, see Fig. 4.2a). We use a probe antenna that reaches 4 mm into the waveguide. The latter is guided into the measurement holes with the help of two pins (not shown in

[1] Note that the transmission is a dimensionless quantity since it is always determined relative to what we send into the system at the calibration point.

the figures). We refer to the transmission spectra from this region as "far field" since we measure them far away from the scattering region. Here, all evanescent modes have died out, and the wave propagates freely. Figure 4.3a shows the cross section of the experimental setup during a far-field scan.

- In the left-most part of the scattering region (i.e., $x \geq 0.453$ m), the top plate does not cover the waveguide in an area of 10×10 cm^2, see Figs. 4.1 and 4.2a. Here, we measure the so-called "near field" using a 1 mm antenna that is integrated into a metal plate. While performing a measurement, we press this plate against the waveguide, thus closing the latter. As opposed to the far field, we can measure the near field at arbitrarily close points. The only limiting factor is the precision of the step motors that position the probe antenna. Figure 4.3b shows the cross section of the experimental setup during a near-field scan.

During the far-field measurement, we close the near-field measurement area with an aluminum plate, see Fig. 4.3a. Due to surface irregularities, some small slits can occur between the plate and the waveguide. We do not need to cover the holes for the far-field measurement since they are small (radius 2 mm), and the flux escaping through them is negligible.

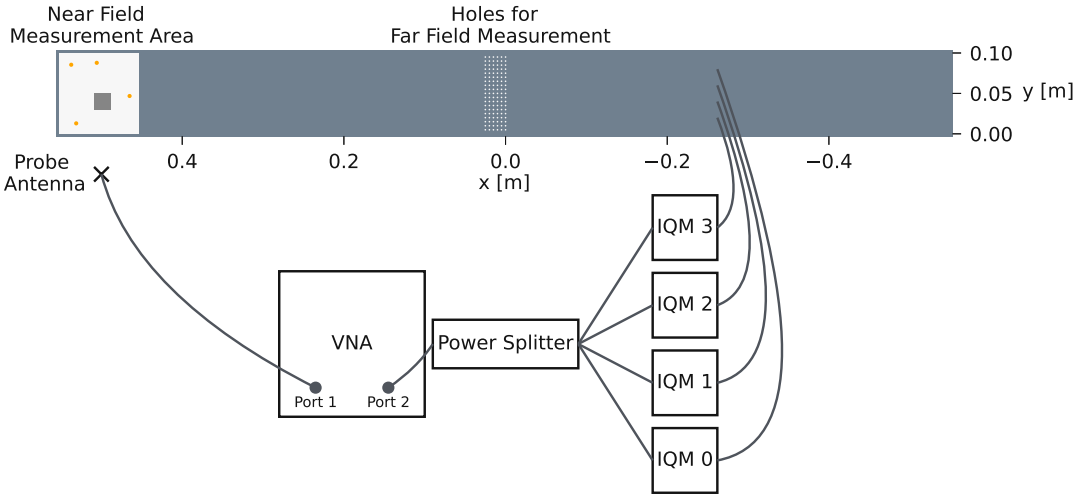

(a) Top view of the waveguide with top plate

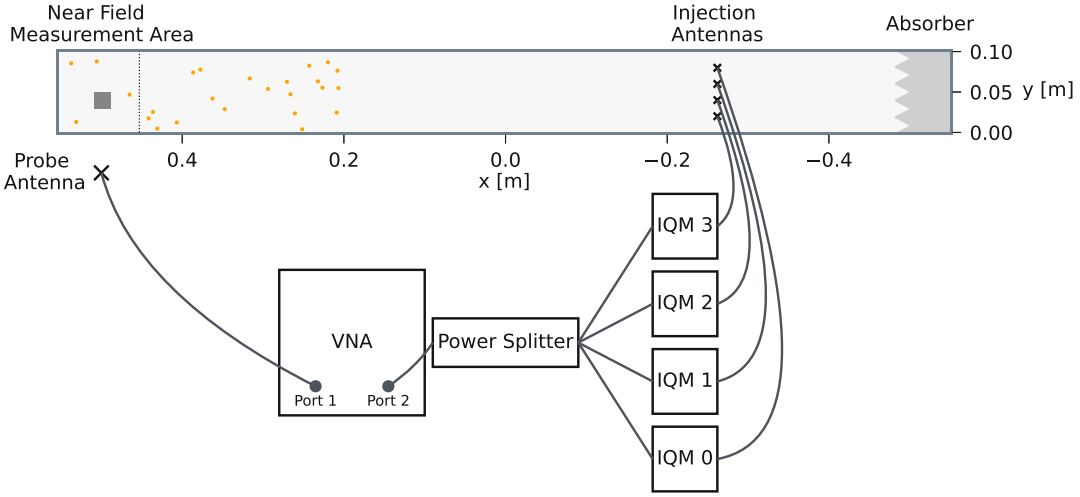

(b) Top view of the waveguide without top plate

Figure 4.2.: Top view of the waveguide with (a) and without (b) top plate. When the experiment runs, the top plate is fixed to the waveguide. Using Teflon (orange circles) and metallic (dark gray square) scatterers, we create a complex scattering environment on the left side. The system is closed on the left and we place an absorber on the right to imitate an infinitely long waveguide. We inject microwaves into the system via four weakly coupled injection antennas (depicted using the symbol x). The latter are connected to port 2 of a VNA via IQ modulators and a power splitter. The probe antenna, which is connected to port 1 of the VNA, is sketched as a slightly larger x and can be positioned using three step motors (not shown).

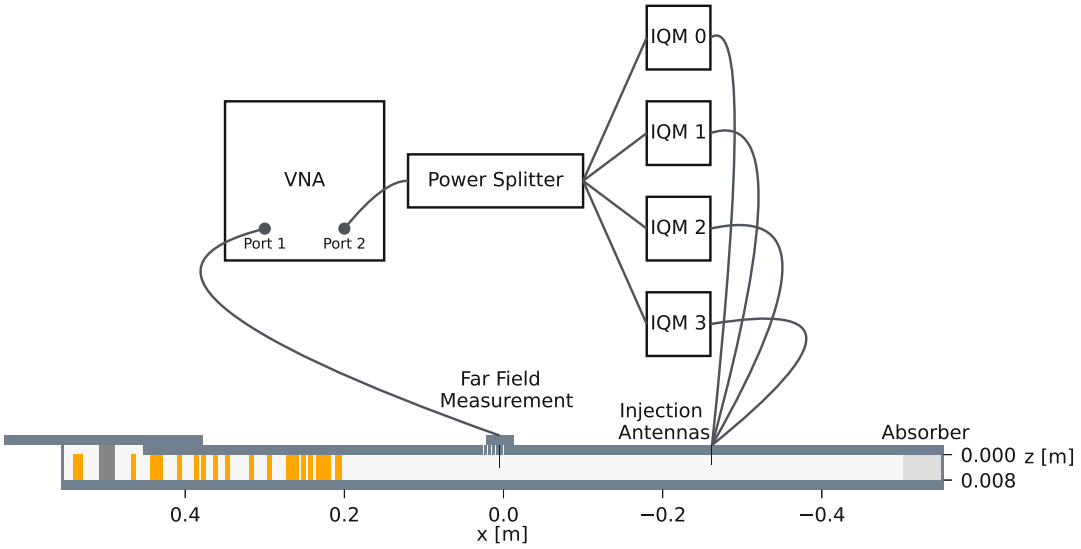

(a) Cross section of the waveguide during a far-field measurement

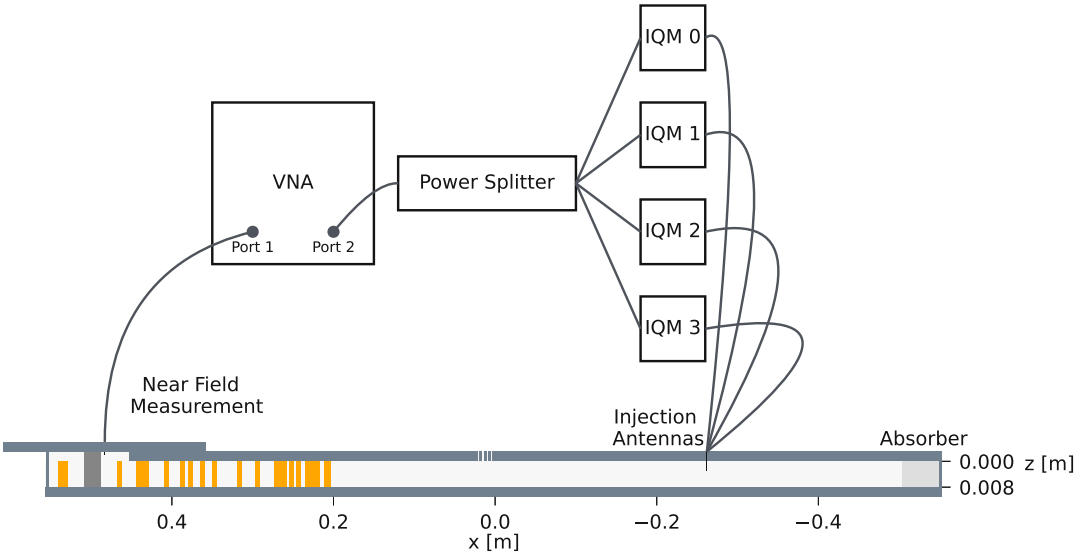

(b) Cross section of the waveguide during a near-field measurement

Figure 4.3.: Cross section of the experimental setup in the x-z-plane during a far-field (a) and a near-field measurement (b). We choose the aspect ratio of the axes scaling as 1:4 (x-scale:z-scale) for better visibility. To imitate an infinitely long system, we place an absorber on the right side. Using Teflon (orange rectangles, 8 mm high) and metallic (dark gray rectangle, 11 mm high) scatterers, we create a complex scattering environment on the left side. We connect the probe antenna to port 1 of the VNA and attach it to three step motors (not shown), which we use to position it. To port 2, we connect the four injection antennas via a power splitter and four IQ modulators. Note that the waveguide is higher in the near field measurement area (11 mm) than in the other regions (8 mm).

4.1.1. Choice of the Frequency Range

In Sec. 2.4, we showed that only $\mathrm{TE}_{m,n}$ and $\mathrm{TM}_{m,n}$ modes exist in rectangular waveguides. We further demonstrated that each TE/TM mode has a cut-off frequency, below which it only exists on length scales that are short compared to the corresponding $1/\Im\{k_x\}$. This behavior is useful when choosing a frequency range for our experiment, since we have the following two constraints:

- We cannot measure the z-dependence of the microwave field, since we cannot vary the probe antenna's z-position within the system.

  $\Longrightarrow$ We want to work at frequencies where $m = 0$.

- With the four injection antennas of the experimental setup, we can control up to four complex degrees of freedom when designing the state that we send into the system.

  $\Longrightarrow$ We want to work at frequencies where $n = 4$.

Following Eq. (2.41), we find that one should choose $f \in [6\ \mathrm{GHz},\ 7.5\ \mathrm{GHz}]$ to satisfy those constraints since:

$$\begin{aligned} f_{\text{cut-off}}(0,4) &= \frac{\omega_{\text{cut-off}}(0,4)}{2\pi} = \frac{4\pi \cdot c[m/s]}{2\pi \cdot 0.1[m]} \approx 6.0\ \mathrm{GHz}, \\ f_{\text{cut-off}}(0,5) &= \frac{\omega_{\text{cut-off}}(0,5)}{2\pi} = \frac{5\pi \cdot c[m/s]}{2\pi \cdot 0.1[m]} \approx 7.5\ \mathrm{GHz}, \\ f_{\text{cut-off}}(1,0) &= \frac{\omega_{\text{cut-off}}(1,0)}{2\pi} = \frac{1\pi \cdot c[m/s]}{2\pi \cdot 0.008[m]} \approx 18.7\ \mathrm{GHz}, \end{aligned} \tag{4.1}$$

where we set the waveguide width $d_y = 10$ cm, the waveguide height $d_z = 8$ mm, and used the refractive index of air $\sqrt{\epsilon\mu} = 1$. In the experiment, we measure the transmission spectra $S_{12}(f)$ for 2501 equally spaced frequency points in the interval $f \in [6\ \mathrm{GHz},\ 7.5\ \mathrm{GHz}]$, ensuring that $\mathrm{TE}_{0,n}, n \leq 4$ are the only propagating modes.[2]

[2] Remember that $\mathrm{TM}_{m,n}$ modes only exist for $m > 0$ and $n > 0$.

4.2. Data Processing

4.2.1. Smoothing over Frequency

To reduce the measurement noise, we apply a triangular filter to the transmission spectra for both near- and far-field measurements. We choose a filter function of width 7:

$$\begin{aligned} S_{12}^{\text{smoothed}}(n_f) = &\frac{1}{16}\left(S_{12}(n_f-3)+S_{12}(n_f+3)\right) \\ &+\frac{2}{16}\left(S_{12}(n_f-2)+S_{12}(n_f+2)\right) \\ &+\frac{3}{16}\left(S_{12}(n_f-1)+S_{12}(n_f+1)\right) \\ &+\frac{4}{16}S_{12}(n_f), \end{aligned}$$

where $n_f \in \{3,4,5,...,2497\}$ is the frequency index. Figure 4.4 shows the real part of a spectrum before and after the smoothing procedure. We measured the spectrum in the hole at position ($x = 1.5$ cm, $y = 5$ cm) using the far-field probe antenna and the following IQM settings:

$$\begin{aligned} \text{IQM}_0 &: \{\text{attenuation: 0 dB, phase: 0}\}, \\ \text{IQM}_{i\neq 0} &: \{\text{attenuation: 40 dB, phase: 0}\}, \end{aligned}$$

i.e., the 0th injection antenna is fully illuminated, while all other injection antennas are on maximal attenuation.

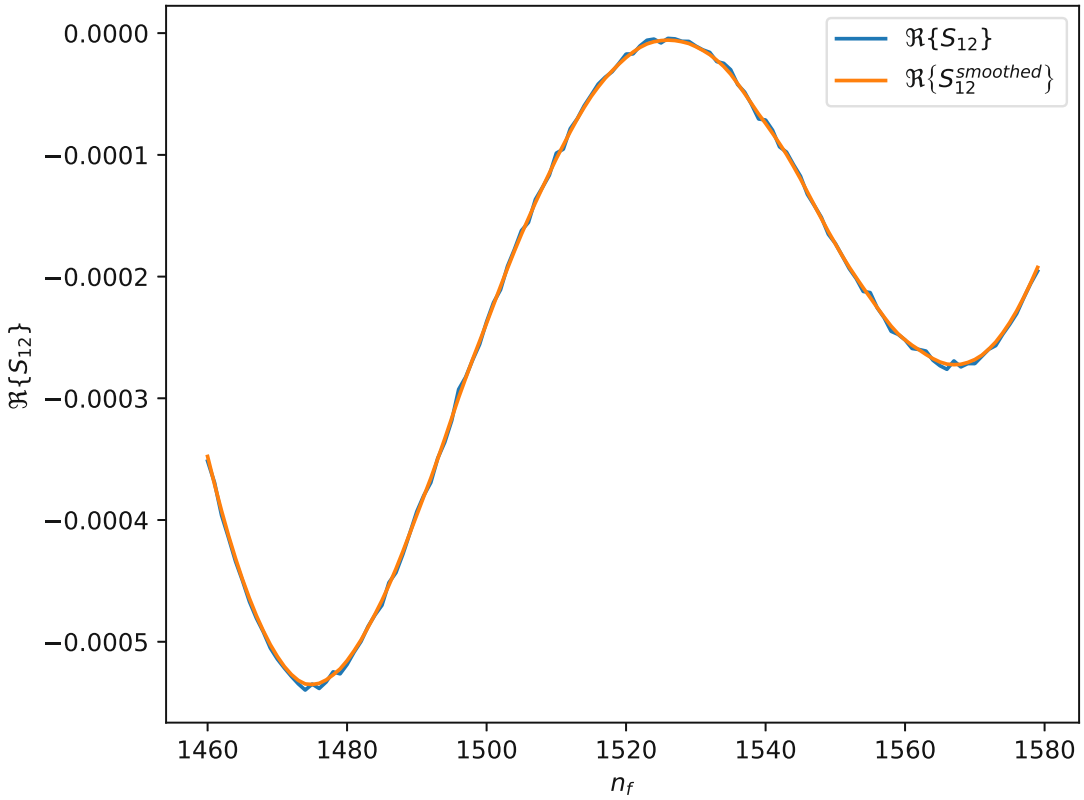

Figure 4.4.: Real part of a transmission spectrum $S_{12}(f) = S_{12}(n_f)$ before (blue) and after (orange) the smoothing procedure. We show only a small range of frequency indices.

4.2.2. Determining $\mathbf{c}^{\text{in}}$ and $\mathbf{c}^{\text{out}}$

In the far field, the wave propagates freely, and we can determine the $\mathbf{c}^{\text{in}}$ and $\mathbf{c}^{\text{out}}$ from Eq. (2.47) at a fixed frequency and for given IQ modulator settings using the following workflow:

Procedure 1.

1. Measure the far-field spectra on a grid of $n_x \times n_y$ positions. We discard all the frequencies from these spectra except one, such that we obtain a complex scalar function of $i \in \{1, 2, ..., n_x\}$ and $j \in \{1, 2, ..., n_y\}$.[3]

2. We can view this 2D function as n_x 1D functions of $j \in \{1, 2, ..., n_y\}$. For each of these 1D functions, we perform a fit to

$$\psi^{x^i}(y) = \sum_{n=1}^{4} \frac{1}{\sqrt{k_n^x}} \chi_n(y) c_n^{i,\text{meas}}, \tag{4.2}$$

by varying the real and the imaginary part of the $c_n^{i,\text{meas}}$. In Eq. (4.2), x^i denotes the ith x-coordinate at which we measured and

$$\mathbf{c}^{i,\text{meas}} = \begin{pmatrix} c_1^{i,\text{meas}} \\ c_2^{i,\text{meas}} \\ c_3^{i,\text{meas}} \\ c_4^{i,\text{meas}} \end{pmatrix}$$

is the corresponding transverse mode composition. Note that we need to measure the complex field at $n_y \geq 4$ y-positions to fix all four of the complex parameters in $\mathbf{c}^{i,\text{meas}}$.

3. c_n^{in} and c_n^{out}, i.e., the mode compositions of the incoming and outgoing wavefront, are related to $c_n^{i,\text{meas}}$ via:

$$c_n^{i,\text{meas}} = c_n^{\text{in}} \mathrm{e}^{\mathrm{i}k_n^x x^i} + c_n^{\text{out}} \mathrm{e}^{-\mathrm{i}k_n^x x^i},$$

This can be rewritten as a linear regression problem, i.e., find the vector $\boldsymbol{\alpha}_n$ such that

$$\sum_{j=1}^{2n_x} \|\boldsymbol{\alpha}_n^\top \mathbf{v}_n^j - w_n^j\|^2 \to \min,$$

[3] Note that we have one open lead ($M = 1$), and, unlike in Sec. 2.5, the index i does not denote the lead.

where we sum until $2n_x$ rather than until n_x since we need to fix the real and the imaginary part. We identify:

$$\boldsymbol{\alpha}_n = \begin{pmatrix} \Re\left\{c_n^{\text{in}}\right\} \\ \Im\left\{c_n^{\text{in}}\right\} \\ \Re\left\{c_n^{\text{out}}\right\} \\ \Im\left\{c_n^{\text{out}}\right\} \end{pmatrix},$$

$$w_n^j = \begin{cases} \Re\left\{c_n^{j,\text{meas}}\right\} \text{ if } j \leq n_x \\ \Im\left\{c_n^{j-n_x,\text{meas}}\right\} \text{ if } j > n_x \end{cases},$$

$$\mathbf{v}_n^j = \begin{cases} \begin{pmatrix} \Re\left\{\mathrm{e}^{\mathrm{i}k_n^x x_j}\right\} \\ -\Im\left\{\mathrm{e}^{\mathrm{i}k_n^x x_j}\right\} \\ \Re\left\{\mathrm{e}^{-\mathrm{i}k_n^x x_j}\right\} \\ -\Im\left\{\mathrm{e}^{-\mathrm{i}k_n^x x_j}\right\} \end{pmatrix} \text{ if } j \leq n_x \\ \begin{pmatrix} \Im\left\{\mathrm{e}^{\mathrm{i}k_n^x x_{j-n_x}}\right\} \\ \Re\left\{\mathrm{e}^{\mathrm{i}k_n^x x_{j-n_x}}\right\} \\ \Im\left\{\mathrm{e}^{-\mathrm{i}k_n^x x_{j-n_x}}\right\} \\ \Re\left\{\mathrm{e}^{-\mathrm{i}k_n^x x_{j-n_x}}\right\} \end{pmatrix} \text{ if } j > n_x \end{cases}.$$

Note that we perform the linear regression for each of the modes $n \in \{1, 2, 3, 4\}$. We need at least four equations to fix all parameters of $\boldsymbol{\alpha}_n$. Since the number of equations is $2n_x$, we find that $n_x \geq 2$.

In practice, we measure at all $n_x \times n_y = 6 \times 19$ possible positions in the far field to reduce the measurement noise. For the linear regression, we use the scikit-learn library [21].

Figure 4.5 shows the result of such a workflow for $f = 6.45$ GHz and the following IQM settings:

$$\text{IQM}_0 : \{\text{attenuation: 0 dB, phase: 0}\},$$
$$\text{IQM}_{i\neq 0} : \{\text{attenuation: 40 dB, phase: 0}\},$$

i.e., the 0th injection antenna is fully illuminated, while the remaining antennas are on maximal attenuation. We depict the real part of the measured transmission and the far-field wavefunction from Eq. (2.47), where we plug in the $\mathbf{c}^{\text{in}}$ and $\mathbf{c}^{\text{out}}$ we obtain using Proc. 1. Since the latter agree well, we conclude that the wave propagates freely in the far field and we can characterize it with the $\mathbf{c}^{\text{in}}$ and $\mathbf{c}^{\text{out}}$ from Proc. 1.

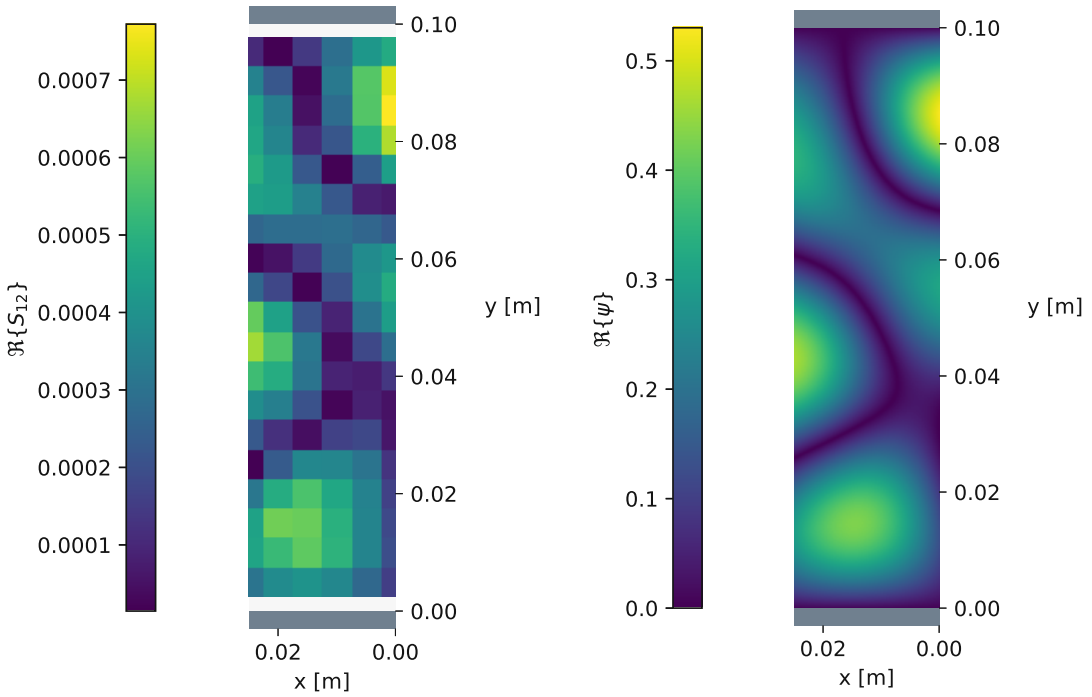

(a) Measured transmission

(b) Wavefunction

Figure 4.5.: Comparison of the measured transmission at $f = 6.45$ GHz (a) and the wavefunction from Eq. (2.47), where we plug in the $\mathbf{c}^{\text{in}}$ and $\mathbf{c}^{\text{out}}$ from Proc. 1 (b). We illuminate the 0th injection antenna fully while attenuating the remaining antennas maximally and show the real part of the transmission/wavefunction. Note that we normalized $\mathbf{c}^{\text{in}} \to \mathbf{c}^{\text{in}}/\|\mathbf{c}^{\text{in}}\|$ and $\mathbf{c}^{\text{out}} \to \mathbf{c}^{\text{out}}/\|\mathbf{c}^{\text{in}}\|$, which explains the different scales of the plots.

4.2.3. Scattering Matrix and Experimental Loss

Since we can extract $\mathbf{c}^{\text{in}}$ and $\mathbf{c}^{\text{out}}$ from a far-field measurement, we can also determine the scattering matrix $\mathbf{S}$, which relates them according to Eq. (2.49).[4] To find the latter, we require four linearly independent $\mathbf{c}^{\text{in}}$ and the corresponding $\mathbf{c}^{\text{out}}$. We obtain these vector pairs by choosing four inherently different IQM settings:

$$\begin{aligned} \text{IQM}_i &: \{\text{attenuation: 0 dB, phase: 0}\}, \\ \text{IQM}_{j\neq i} &: \{\text{attenuation: 40 dB, phase: 0}\}, \\ i &\in \{1,2,3,4\}, \end{aligned}$$

i.e., we fully illuminate one injection antenna after another, always maximally attenuating the remaining antennas. Indeed, we find that the $\mathbf{c}^{\text{in}}$ we obtain this way are linearly independent:

$$\frac{1}{\prod_i \|\mathbf{c}^{\text{in}}_{\text{IQM}_i}\|} \left| \det \begin{pmatrix} | & | & | & | \\ \mathbf{c}^{\text{in}}_{\text{IQM}_0} & \mathbf{c}^{\text{in}}_{\text{IQM}_1} & \mathbf{c}^{\text{in}}_{\text{IQM}_2} & \mathbf{c}^{\text{in}}_{\text{IQM}_3} \\ | & | & | & | \end{pmatrix} \right| \approx 0.86,$$

where we used the scattering geometry shown in Fig. 4.2 and $\mathbf{c}^{\text{in}}_{\text{IQM}_i}$ denotes the incoming state in mode basis when the ith injection antenna is illuminated. These vectors thus form a basis, which we call IQM basis. Consequently, we can obtain the scattering matrix by solving the following equation system for $\mathbf{S}$:

$$\begin{aligned} &\mathbf{S} \begin{pmatrix} | & | & | & | \\ \mathbf{c}^{\text{in}}_{\text{IQM}_0} & \mathbf{c}^{\text{in}}_{\text{IQM}_1} & \mathbf{c}^{\text{in}}_{\text{IQM}_2} & \mathbf{c}^{\text{in}}_{\text{IQM}_3} \\ | & | & | & | \end{pmatrix} \\ &\equiv \begin{pmatrix} S_{11} & \dots & S_{14} \\ \vdots & \ddots & \vdots \\ S_{41} & \dots & S_{44} \end{pmatrix} \begin{pmatrix} | & | & | & | \\ \mathbf{c}^{\text{in}}_{\text{IQM}_0} & \mathbf{c}^{\text{in}}_{\text{IQM}_1} & \mathbf{c}^{\text{in}}_{\text{IQM}_2} & \mathbf{c}^{\text{in}}_{\text{IQM}_3} \\ | & | & | & | \end{pmatrix} \\ &= \begin{pmatrix} | & | & | & | \\ \mathbf{c}^{\text{out}}_{\text{IQM}_0} & \mathbf{c}^{\text{out}}_{\text{IQM}_1} & \mathbf{c}^{\text{out}}_{\text{IQM}_2} & \mathbf{c}^{\text{out}}_{\text{IQM}_3} \\ | & | & | & | \end{pmatrix}. \end{aligned}$$

We show the result of the scattering matrix measurement for the geometry from Fig. 4.2b at $f = 6.45$ GHz in Fig. 4.6, where we depict both $|\mathbf{S}|$ and $|\mathbf{S}^\dagger\mathbf{S}|$. While $\mathbf{S}$ should be symmetric according to the Lorentz reciprocity theorem (see Ref. [22]), we observe a slight asymmetry due to the measurement noise. Furthermore, we see that the scattering matrix is not unitary. This can be explained by a weak global loss within the waveguide, which arises due to the skin effect.[5]

[4] In the experiment, we have one open lead, and thus $M = 1$.

[5] There are also local losses in the setup since some of the flux escapes through the holes in the top plate and the slits that occur when the near-field measurement area is not perfectly closed. Moreover, the probe antenna absorbs some of the radiation, which also leads to local losses. However, the contribution of these effects is small, and we neglect it in our discussion.

The nth diagonal element of $|\mathbf{S}^\dagger\mathbf{S}|$ constitutes a measure of the total intensity that returns to the asymptotic region if the nth mode is injected into the system. Consequently, we refer to this quantity as "mode attenuation coefficient" in the following. In Fig. 4.6b, we observe that the latter decreases for higher n, which means that higher modes are more strongly affected by the global loss. We can understand this qualitatively by remembering that for higher modes $k_y = \frac{n\pi}{b}$ increases and thus $k_x = \sqrt{k^2 - k_y^2}$ decreases. Consequently, the angle of propagation with respect to the x-axis, i.e., $\alpha = \arctan\left(\frac{k_y}{k_x}\right)$, increases, and high modes "bounce" up and down more often. Therefore, they travel a longer distance within the system and are more prone to absorption. Note that this discussion is only valid in regions where the wave propagates freely (i.e., in the far field).

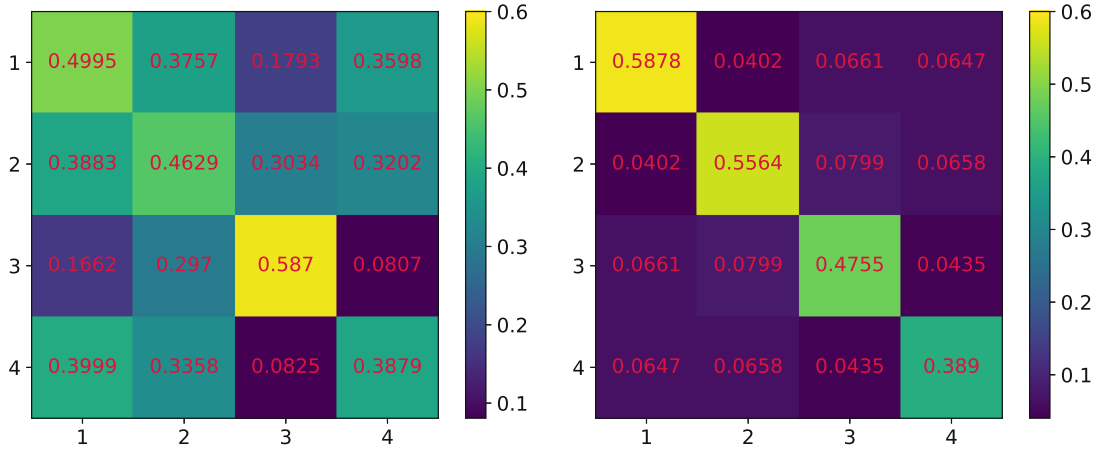

(a) $|\mathbf{S}|$ (b) $|\mathbf{S}^\dagger\mathbf{S}|$

Figure 4.6.: $|\mathbf{S}|$ (a) and $|\mathbf{S}^\dagger\mathbf{S}|$ (b) in mode basis, where we measured $\mathbf{S}$ at $f = 6.45$ GHz for the scattering geometry of Fig. 4.2. The ticks on the left and at the bottom show the mode number n (see Eq. (2.47)). While the colors indicate how large the matrix elements are, the exact values are denoted in each of the cells.

4.2.4. Tuning the Incoming State

Once we know the IQM basis, we can inject an arbitrary state $\mathbf{c}^{\text{in}}$ into the waveguide using the superposition principle. To describe this procedure, we introduce the transformation matrix from IQM to mode basis:

$$\mathbf{T}_{\text{mode}\leftarrow\text{IQM}} = \begin{pmatrix} | & | & | & | \\ \mathbf{c}^{\text{in}}_{\text{IQM}_0} & \mathbf{c}^{\text{in}}_{\text{IQM}_1} & \mathbf{c}^{\text{in}}_{\text{IQM}_2} & \mathbf{c}^{\text{in}}_{\text{IQM}_3} \\ | & | & | & | \end{pmatrix}. \tag{4.3}$$

Consider an easy example to motivate this definition: say, we fully illuminate the 0th and the 3rd IQ modulator with a relative phase of π. In IQM basis this

corresponds to

$$\begin{pmatrix} 1 \\ 0 \\ 0 \\ \mathrm{e}^{\mathrm{i}\pi} \end{pmatrix}.$$

In the mode basis, this corresponds to

$$\mathbf{c}^{\mathrm{in}}_{\mathrm{IQM}_0} + \mathrm{e}^{\mathrm{i}\pi}\mathbf{c}^{\mathrm{in}}_{\mathrm{IQM}_3},$$

which can be written as

$$\mathbf{T}_{\mathrm{mode}\leftarrow\mathrm{IQM}} \begin{pmatrix} 1 \\ 0 \\ 0 \\ \mathrm{e}^{\mathrm{i}\pi} \end{pmatrix}.$$

The transformation from mode to IQM basis is then just the inverse:

$$\mathbf{T}_{\mathrm{IQM}\leftarrow\mathrm{mode}} = \mathbf{T}^{-1}_{\mathrm{mode}\leftarrow\mathrm{IQM}}.$$

Therefore, we can obtain the IQM settings corresponding to the desired input state $\mathbf{c}^{\mathrm{in}}$ using the following procedure:

Procedure 2.

1. Perform the matrix multiplication
$$\mathbf{c}^{\mathrm{IQM}} := \mathbf{T}_{\mathrm{IQM}\leftarrow\mathrm{mode}}\mathbf{c}^{\mathrm{in}}.$$
2. Rescale $\mathbf{c}^{\mathrm{IQM}}$ such that one of the vector's entries has an absolute value of 1, ensuring that one injection antenna is fully illuminated. This practice reduces noise effects since it leads to the highest possible transmission.
3. Convert the complex numbers in each entry of $\mathbf{c}^{\mathrm{IQM}}$ into an attenuation in dB
$$\min\left(40,\ -20\log_{10}\left(\left|c_n^{\mathrm{IQM}}\right|\right)\right)$$
and a phase in radian
$$\arg\left(c_n^{\mathrm{IQM}}\right).$$

Fig. 4.7 shows the result of such a procedure when aiming to inject the maximum eigenstate of the Fisher information operator for $\theta = x_{\mathrm{scat}}$ and $f = 6.45$ GHz into the experimental setup from Fig. 4.2. We compare the mode composition and the transmission of the desired and the measured incoming state. While the mode compositions show some deviations due to the measurement noise, the transmissions have the same structure, and we conclude that we can use Proc. 2 to inject a desired wavefront into the waveguide.

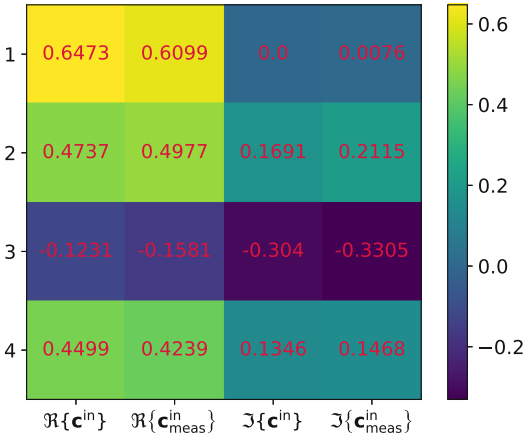

(a) Desired/measured mode composition

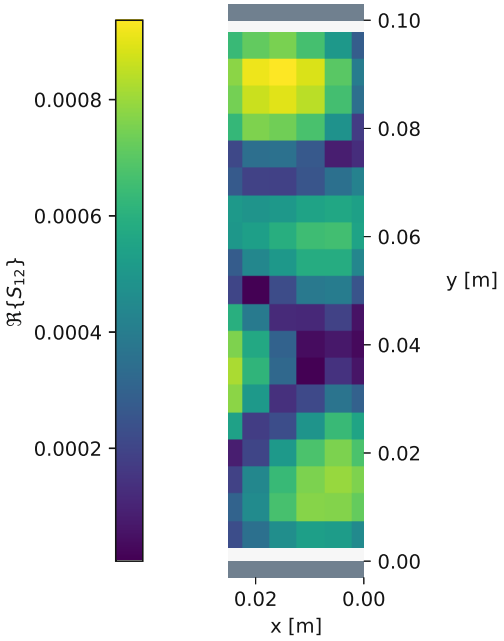

(b) Desired transmission (real part)

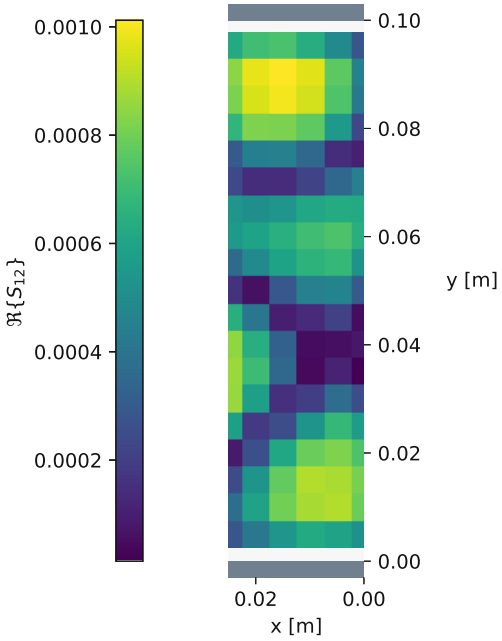

(c) Measured transmission (real part)

Figure 4.7.: Wavefront engineering, i.e., the injection of a desired incoming state. We used the setup from Fig. 4.2, chose $f = 6.45$ GHz, and aimed to inject the maximum eigenstate of the Fisher information operator for $\theta = x_{\text{scat}}$. (a) compares the real and imaginary part of the desired incoming state ($\mathbf{c}^{\text{in}}$) and the incoming state we measure when using the IQM settings found in Proc. 2 ($\mathbf{c}^{\text{in}}_{\text{meas}}$). The ticks on the left show the mode number n (see Eq. (2.47)). While the colors indicate how large the vector elements are, the exact values are denoted in each of the cells. (b) shows the desired transmission, which we obtain by superposing the IQM basis transmissions numerically with the coefficients $\mathbf{T}_{\text{IQM}\leftarrow\text{mode}}\mathbf{c}^{\text{in}}$. (c) shows the transmission we measured in situ when using the IQM settings from Proc. 2. Note that the scale of this transmission is larger due to the rescaling in step 2 of Proc. 2.

4.3. Workflow

Now that we have introduced all the necessary experimental/data processing techniques, let us discuss the workflow for measuring the Fisher information flow in the near and far field using the setup from Fig. 4.2.

Following Sec. 4.2.3, we determine the scattering matrix $\mathbf{S}$ from a far-field measurement. Then, we perturb the parameter of interest θ by shifting the target scatterer in either x- or y-direction for 4.5 mm and measure the perturbed S matrices, i.e., $\mathbf{S}^{x/y}_{\text{pert}}$, where the superscript denotes the type of the shift. Note that this corresponds to a non-infinitesimal perturbation of θ. We can execute the shift with inaccuracies of less than 0.1 mm by fixing the target scatterer's position with a pin in the bottom plate of the waveguide.

From these scattering matrices, we compute the finite-difference Fisher information operator in mode basis (see Eq. (2.52)):

$$\mathbf{F}^{x/y} = \left(\mathcal{D}^{x/y}\mathbf{S}\right)^{\dagger} \mathcal{D}^{x/y}\mathbf{S}, \tag{4.4}$$

where

$$\mathcal{D}^{x/y}\mathbf{S} = \frac{\left(\mathbf{S}^{x/y}_{\text{pert}} - \mathbf{S}\right)}{4.5\ \text{mm}}.$$

As discussed in Sec. 2.3.3, the properties of Fisher information do not change when replacing the derivatives with respect to θ with finite differences. Therefore, we sloppily refer to $\mathbf{F}^{x/y}$ as Fisher information operator in the following.

Since we always measure the transmission spectra at all 2501 frequency points, we could compute a Fisher information operator for each frequency. We choose $f = 6.45$ GHz and $f = 6.9$ GHz such that we have four Fisher information operators, one for each combination of perturbation and frequency. Following Proc. 2, we can compute the IQM settings corresponding to the four eigenstates of each of those four operators. We aim to measure the (finite-difference) Fisher information flow for these states, i.e. (see Eq. (2.24)):

$$\mathbf{j}^{x/y} = \Im\left\{\mathcal{D}^{x/y}\psi^{*}\nabla\mathcal{D}^{x/y}\psi\right\}, \tag{4.5}$$

where

$$\mathcal{D}^{x/y}\psi = \frac{\psi^{x/y}_{\text{pert}} - \psi}{4.5\ \text{mm}},$$

and $\psi^{x/y}_{\text{pert}}/\psi$ is the measured transmission in the perturbed/unperturbed system. We inject 20 states into the unperturbed system (4 eigenstates of $\mathbf{F}^{x}$ *and* $\mathbf{F}^{y}$ at both frequencies and 4 IQM basis states) and 12 states into each perturbed system (4 eigenstates of $\mathbf{F}^{x}$ *or* $\mathbf{F}^{y}$ at both frequencies and 4 IQM basis states) and scan the near and far field. Note that we measure the transmission for the linearly independent IQM basis states since we can construct any other wavefunction by superposing them numerically. The sequence of measurements is summed up in the following:

Procedure 3.

1. Measure the field corresponding to the IQM basis states in the far field for the unperturbed and the two perturbed systems. Calculate the Fisher information operators from those measurements.

2. Change the probe antenna and scan the near field for all three systems when injecting the Fisher information eigenstates and the IQM basis eigenstates.

3. Change the probe antenna again and do a far-field scan for all three systems when injecting the Fisher information eigenstates.

4. Repeat step 1. Comparing the Fisher information operators from this step with those from step 1 enables us to assess the measurement uncertainties (see Sec. 4.4).

Note that it would have been better to interchange the order of steps 2 and 3 since we would not have had to exchange the probe antenna before measuring the flows in the far field.[6] Since we achieved a good precision in the far-field flow measurement nonetheless (see Sec. 4.5.1) and due to temporal constraints (Proc. 3 takes several weeks), we did not repeat the procedure to see whether we could improve our results further.

[6] Unfortunately, we only had the idea of measuring the Fisher information flow in the far field while the near-field measurement was already running.

4.4. Measurement Uncertainties

Before we present the results from Proc. 3, let us discuss some sources of uncertainties in the experiment. Two main factors limit the precision of the measurements:

Uncertainties from the Setup Apart from the electronic noise in the VNA, we need to consider inaccuracies in the probe antenna placement. For near-field measurements, they are of order $\mathcal{O}(50\ \mu\text{m})$ in both x- and y-direction. During a far-field measurement, the probe antenna is guided into a hole in the top plate of the waveguide by two pins. Nonetheless, the antenna is not always perfectly positioned in the middle of the measurement hole, which influences the measured transmission spectrum.

Uncertainties from System Changes In the course of the workflow described in Proc. 3, the experimental setup is modified several times. The manipulations of the system include:

- Opening and closing the near-field measurement area to shift the target scatterer. The plate closing the near-field measurement area cannot be placed the same every time. Consequently, the (tiny) slits between the plate and the waveguide are not always the same, which influences the local absorption.
- Changing the probe antenna. As a result, the cables connecting the VNA and the probe antenna are arranged differently, which leads to different relative phases in the transmission spectra.

Furthermore, the measurements described in Proc. 3 take several weeks. During this time, the ambient temperature increased since the season changed from spring to summer. The higher temperature led to a higher absorption due to the Skin effect and to an expansion of the system[7], adding further uncertainties to the measurement process.

To get a feeling for the impact of the noise and the system changes, we remeasured the far-field transmissions corresponding to the IQM basis states in step 4 of Proc. 3 and compared them to the data from step 1, see Fig. 4.8. While we observe differences in both the transmission spectra and the Fisher information eigenstates, the general structure of the data remains similar. Interestingly, the deviations of the large eigenvalues are smaller, which suggests that the corresponding Fisher information flows are less prone to measurement uncertainties.

[7] Note that the definition of the transverse modes depends on the side length of the system, see Eq. (2.48).

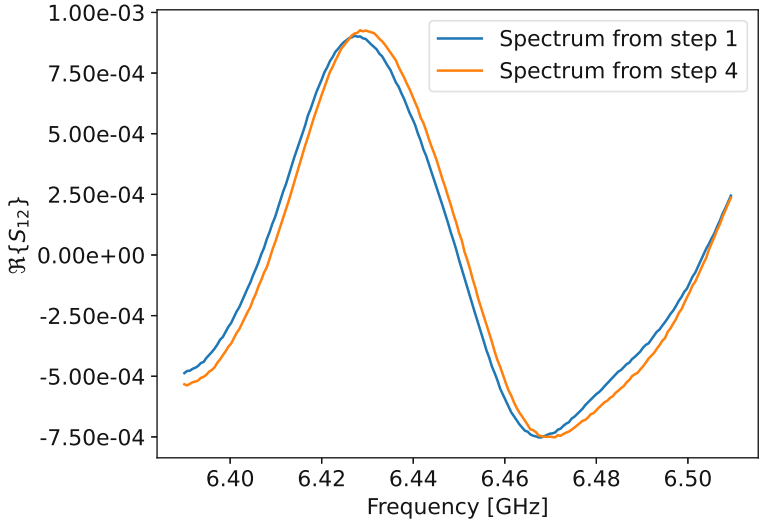

(a) Comparison of spectra from step 1 and 4

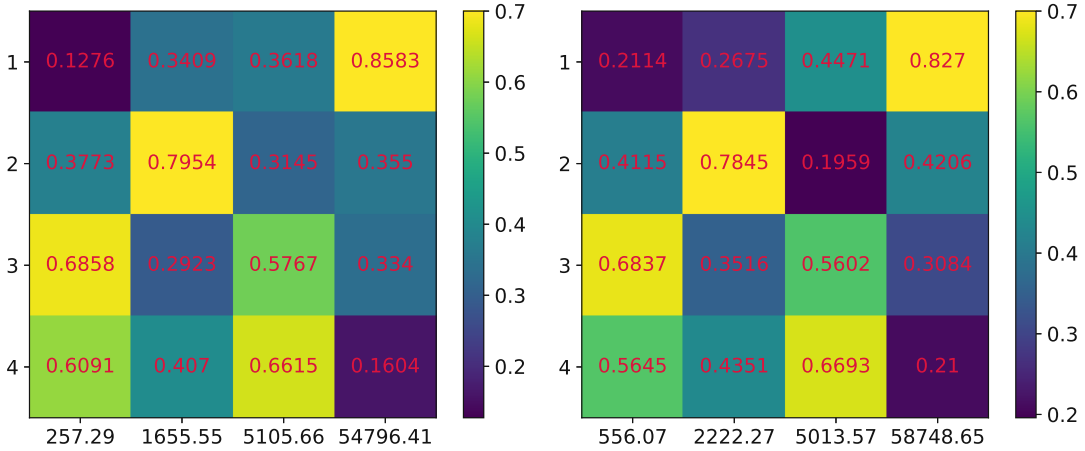

(b) $\mathbf{F}^y$ eigenvectors/-values from step 1 (c) $\mathbf{F}^y$ eigenvectors/-values from step 4

Figure 4.8.: Comparison of the far-field IQM basis state measurement in step 1 and step 4 of Proc. 3. Several weeks passed between the two measurements, in the course of which we opened and closed the near-field measurement area multiple times and changed the probe antenna twice. (a) compares the non-smoothed spectra we measured at $[x = 1.5\text{ cm}, y = 5\text{ cm}]$ when injecting the 0th IQM basis state. We only show a small range of frequencies around $f = 6.45$ GHz. (b)/(c) depicts the eigenvectors and eigenvalues of the Fisher information operator $\mathbf{F}^y$ at $f = 6.45$ GHz, which we computed from the measurements in step 1/4 of Proc. 3. Each column corresponds to the element-wise absolute value of an eigenvector in mode basis. The ticks on the left show the mode number n (see Eq. (2.47)). While the colors indicate how large the vector elements are, the exact values are denoted in each of the cells. The eigenvalues that correspond to the eigenstates are shown under the columns.

4.5. Results

To conclude this chapter, we present the Fisher information flow we observed experimentally in the far and near field. While the far-field measurements show that the flow is a local representation of Fisher information, the near-field data demonstrates how waves extract information and transport it through a complex scattering environment. For conciseness, we only present the measurements at $f = 6.45$ GHz; the measurements at $f = 6.9$ GHz are shown in the appendix.

4.5.1. Far-Field Fisher Information Flow

The measurement of the Fisher information flow in the far field is particularly interesting since we want to check whether the surface integral of the flow in the asymptotic region is equal to the eigenvalue of the injected state. This relation, which we derived in Sec. 2.5.3, is one of the main results of our work since it implies that the flow constitutes a local measure for Fisher information.

In the far field, we can only measure at positions that are 5 mm apart in x- and y-direction. On such a coarse grid, the direct computation of the flow from the measurement data would be error-prone since the spatial gradient could not be evaluated precisely. Moreover, the corresponding surface integral would be inexact due to the small number of data points. To avoid these problems, we calculate the $\mathbf{c}^{\text{in}}$ and $\mathbf{c}^{\text{out}}$ corresponding to the transmission spectra using Proc. 1. Then, we use the wavefunction from Eq. (2.47) to evaluate the Fisher information flow and its surface integral. For a comparison of the measured transmission and the corresponding wavefunction, see Fig. 4.5.

The far-field Fisher information flows when injecting the eigenstates of $\mathbf{F}^x$ (for $\theta = x_{\text{scat}}$) and $\mathbf{F}^y$ (for $\theta = y_{\text{scat}}$) at $f = 6.45$ GHz are shown in Figs. 4.9 and 4.10. We note that the scale of the vector plots decreases from the largest to the smallest eigenstate. This implies that the outgoing wavefronts corresponding to the larger eigenvalues carry more Fisher information.

In Fig. 4.11, we compare the surface integral of these flows to the corresponding eigenvalues of the Fisher information operator. To evaluate the integrals, we choose an integration path that encompasses the entire scattering region and passes through the waveguide parallel to the y-axis at $x = 0$ m. Despite the measurement uncertainties described in Sec. 4.4, we only observe relative deviations of $\mathcal{O}(5\%)$ between the maximal eigenvalues and the corresponding fluxes. For the smaller eigenstates, the discrepancies grow as the signal-to-noise ratio decreases.

The measurements at $f = 6.9$ GHz exhibit similar behavior, see Sec. B of the appendix.

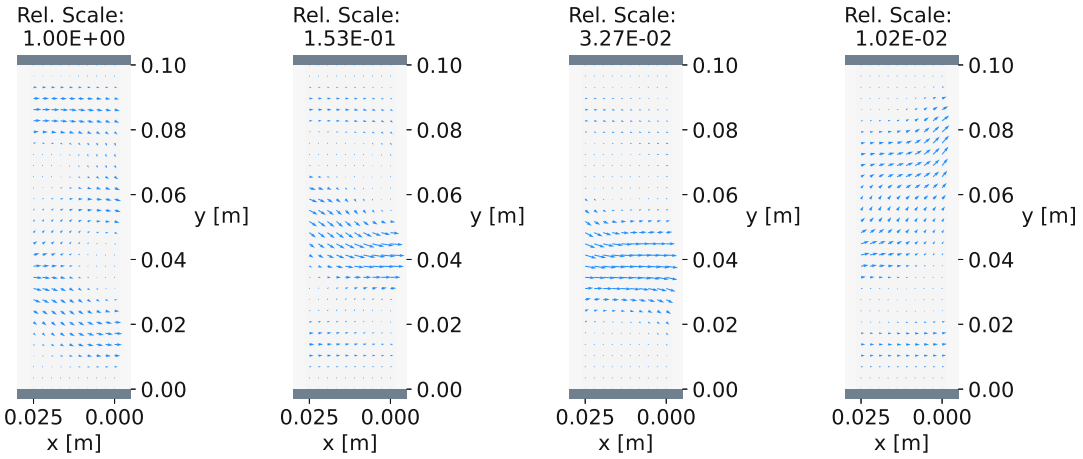

Figure 4.9.: Fisher information flows for $\theta = x_{\text{scat}}$ in the far-field measurement area when injecting the four eigenstates of $\mathbf{F}^x$ at 6.45 GHz. We arrange the flows according to the corresponding eigenvalues in decreasing order from left to right. The relative scales of the vector plots are denoted above the figures.

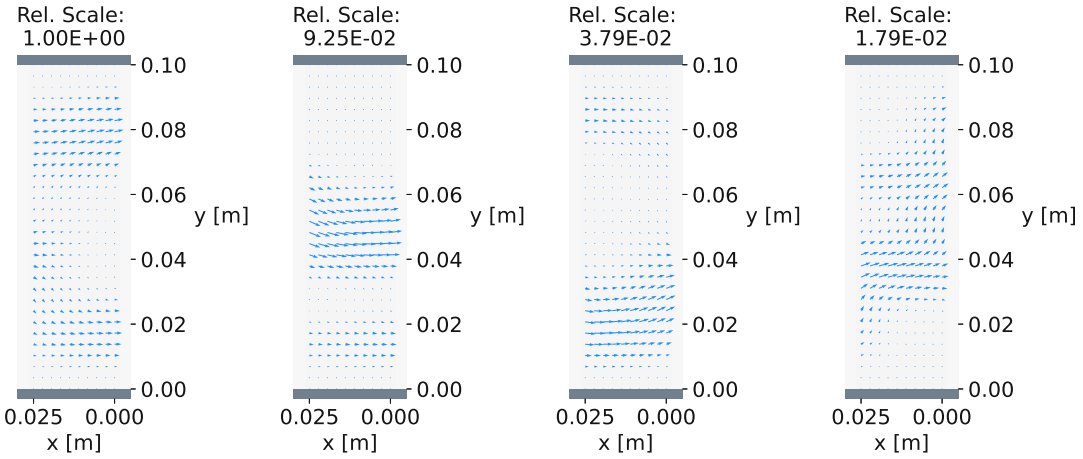

Figure 4.10.: Fisher information flows for $\theta = y_{\text{scat}}$ in the far-field measurement area when injecting the four eigenstates of $\mathbf{F}^y$ at 6.45 GHz. We arrange the flows according to the corresponding eigenvalues in decreasing order from left to right. The relative scales of the vector plots are denoted above the figures.

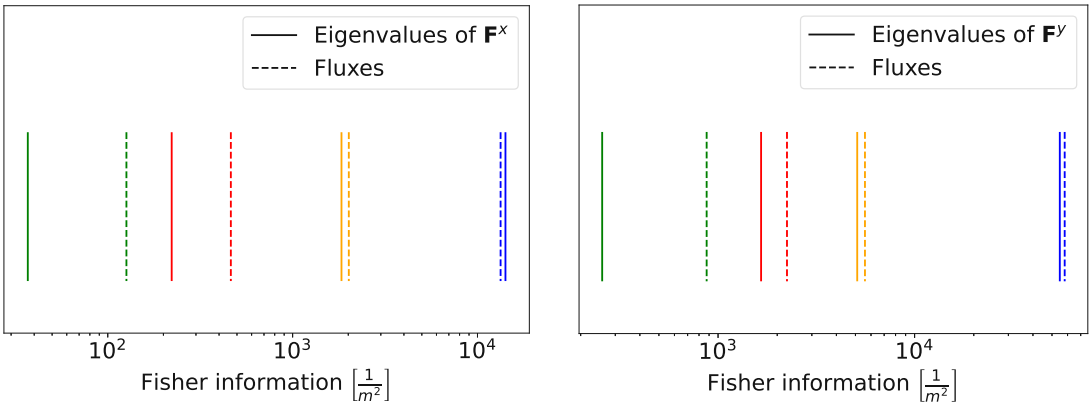

(a) (b)

Figure 4.11.: Comparison of the fluxes $\int_0^{0.1\text{ m}} \mathbf{j}^{x/y}(x=0,y)\cdot(-\hat{\mathbf{e}}_x)dy$ to the eigenvalues for $\theta = x_{\text{scat}}$ (a) and $\theta = y_{\text{scat}}$ (b) at $f = 6.45$ GHz. The dotted lines indicate the fluxes, and the solid lines indicate the eigenvalues. Each eigenstate is depicted using a different color: the largest eigenstate is shown in blue, the second-largest in yellow, the third-largest in red, and the smallest in green. Note that we show the Fisher information on a logarithmic x-axis. If there were no experimental uncertainties, the fluxes would be equal to the eigenvalues.

4.5.2. Near-Field Fisher Information Flow

The measurement of the Fisher information flow in the near field reveals where information originates and how it behaves when transported through a complex scattering system. Since the waves do not propagate freely in the vicinity of scatterers, we cannot perform a fit using Eq. (2.47) as we did for the far-field measurements. However, the near-field probe antenna allows us to measure the transmission spectra at arbitrarily close positions, enabling us to approximate the spatial derivatives in the expression for the Fisher information flow.[8] Therefore, we can compute the latter directly from the measured data. We choose to measure the spectra on a grid of 39×39 evenly spaced points that are 2.5 mm apart in x- and y-direction and use central finite differences to evaluate the spatial gradients. At the edges, we use forward/backward finite differences.

The near-field Fisher information flows when injecting the eigenstates of $\mathbf{F}^x$ (for $\theta = x_{\mathrm{scat}}$) and $\mathbf{F}^y$ (for $\theta = y_{\mathrm{scat}}$) at $f = 6.45$ GHz are shown in Figs. 4.12a and 4.13a. As predicted by the theory and the numerical simulations, we observe that information is created in regions where the refractive index changes with θ, i.e., on the left and right side of the target scatterer for $\theta = x_{\mathrm{scat}}$ and on its top and bottom side for $\theta = y_{\mathrm{scat}}$. While the large eigenstates feature a continuous flow picture, the flows corresponding to the smaller eigenstates are dominated by the noise. Note that the relative scale of the vector plots does not necessarily decrease from the largest to the lowest eigenstate since only a fraction of the produced information escapes the near field and contributes to the eigenvalue.[9]

Figs. 4.12b and 4.13b show the flows we obtain at $f = 6.45$ GHz when solving the 2D Helmholtz equation in the projection of the experimental scattering geometry on the x-y plane. Note that we inject the eigenstates of the simulated rather than of the measured Fisher information operators. To account for the experimental losses described in Sec. 4.2.3, we add a uniform imaginary part to the refractive index of the entire system, whose value we fix by comparing the average mode attenuation coefficient from the experiment and the simulation. We find:

$$f = 6.45 \text{ GHz}:$$

$$\frac{\mathrm{Tr}\left[\left(S_{\mathrm{sim}}^{\dagger} S_{\mathrm{sim}}\right)\Big|_{\Im\{n_{\mathrm{glob}}^{\mathrm{add}}\}=1.6\cdot10^{-3}}\right]}{4} \approx \frac{\mathrm{Tr}\left[S_{\mathrm{exp}}^{\dagger} S_{\mathrm{exp}}\right]}{4} \approx 0.50,$$

$$f = 6.9 \text{ GHz}:$$

$$\frac{\mathrm{Tr}\left[\left(S_{\mathrm{sim}}^{\dagger} S_{\mathrm{sim}}\right)\Big|_{\Im\{n_{\mathrm{glob}}^{\mathrm{add}}\}=1.1\cdot10^{-3}}\right]}{4} \approx \frac{\mathrm{Tr}\left[S_{\mathrm{exp}}^{\dagger} S_{\mathrm{exp}}\right]}{4} \approx 0.61,$$

[8] Note that the enhanced spatial resolution comes at the price of a higher waveguide in the near-field measurement area, see Fig. 4.3.

[9] Remember that the area where the refractive index changes with θ can act both as a source and a sink.

where $n_{\text{glob}}^{\text{add}}$ denotes the refractive index we add to the entire system. While the flows corresponding to the maximum eigenstates have the same structure in the experiment and the simulation, we observe deviations in the flows corresponding to the smaller eigenstates. This is another indicator of the maximum information state's robustness with respect to measurement uncertainties.

It is difficult to compare the surface integrals of the flows to the corresponding eigenvalues for the near-field measurement since we do not know the relative coupling strength of the two probe antennas. To properly normalize the near-field wavefunction, we would have to multiply by

$$\psi \to \frac{1}{\|\mathbf{c}^{\text{in}}\|} \frac{C_{\text{ff}}}{C_{\text{nf}}} \psi,$$

where $\mathbf{c}^{\text{in}}$ can be extracted from a far-field measurement with the same IQM settings, and $C_{\text{ff}}/C_{\text{nf}}$ is the coupling strength of the far-/near-field probe antenna. In theory, the coupling strengths could be determined from a reflection spectrum measurement when placing absorbing material around the probe antennas. However, we perform the calibration of the VNA at the end of the analyzer cables rather than at the tip of the probe antennas. Therefore, the absorption and the reflections in the components connecting the analyzer cable and the antenna lead to large uncertainties when determining the antenna's coupling strength.

In Fig. 4.14, we compare the experimental eigenvalues to the corresponding fluxes at different x-positions on the right of the target scatterer. Since we do not know C_{ff} and C_{nf}, we rescale the eigenvalues by a factor α such that the largest flux at the right-most x-coordinate lies on the largest eigenvalue. We find $\alpha \approx 3.26 \cdot 10^{-8}$ for the eigenstates of $\mathbf{F}^x$ in Fig. 4.14a and $\alpha \approx 3.87 \cdot 10^{-8}$ for the eigenstates of $\mathbf{F}^y$ in Fig. 4.14b. This rescaling accounts for the relative antenna coupling strength and the norm of the incoming state. We observe that the largest flux does not fluctuate around the corresponding eigenvalue but decreases towards it. For the smaller fluxes, this effect is hidden by the noise. Due to the short range of x-values and the drastic decrease of the flux, this phenomenon cannot be due to the weak global absorption alone. We believe that the surplus of Fisher information comes from the evanescent modes that arise as the height of the waveguide changes at $x = 0.453$ m, see Fig. 4.3. Further research will be necessary to confirm this interpretation.

The flows and the corresponding surface integrals at $f = 6.9$ GHz exhibit a similar behavior, see Sec. C of the appendix.

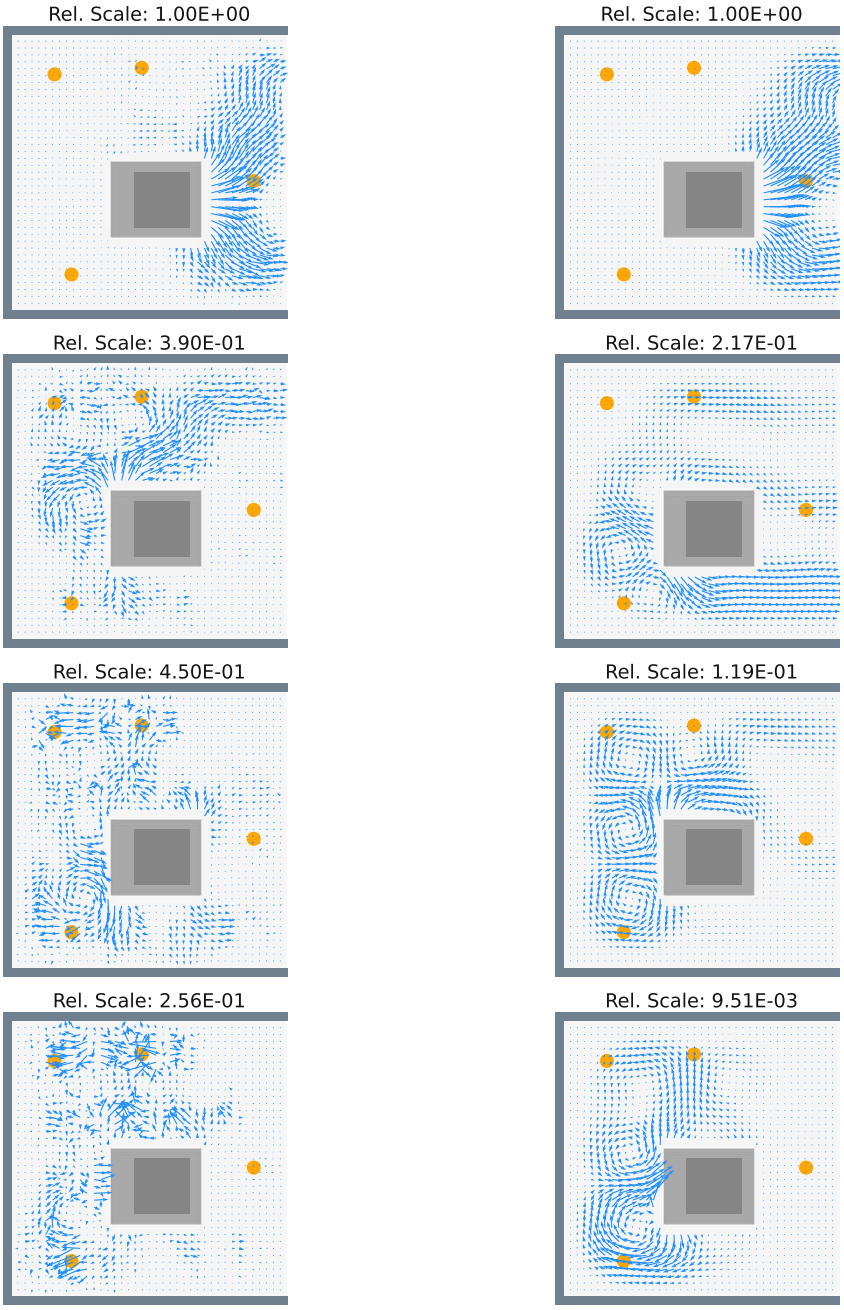

Figure 4.12.: Fisher information flows for $\theta = x_{\text{scat}}$ in the near-field measurement area when injecting the four eigenstates of $\mathbf{F}^x$ at 6.45 GHz. The experimentally measured/simulated flows are shown in (a)/(b) ordered from the largest (top) until the smallest (bottom) corresponding eigenvalue. We depict the Teflon scatterers as orange circles and the metallic target scatterer as a dark gray square. The gray rectangle around the target scatterer corresponds to the region where we could not measure since it is too close to the latter in either the unperturbed or the perturbed system. We denote the relative scales of the vector plots above the figures and do not show the axes ticks/labels to save space.

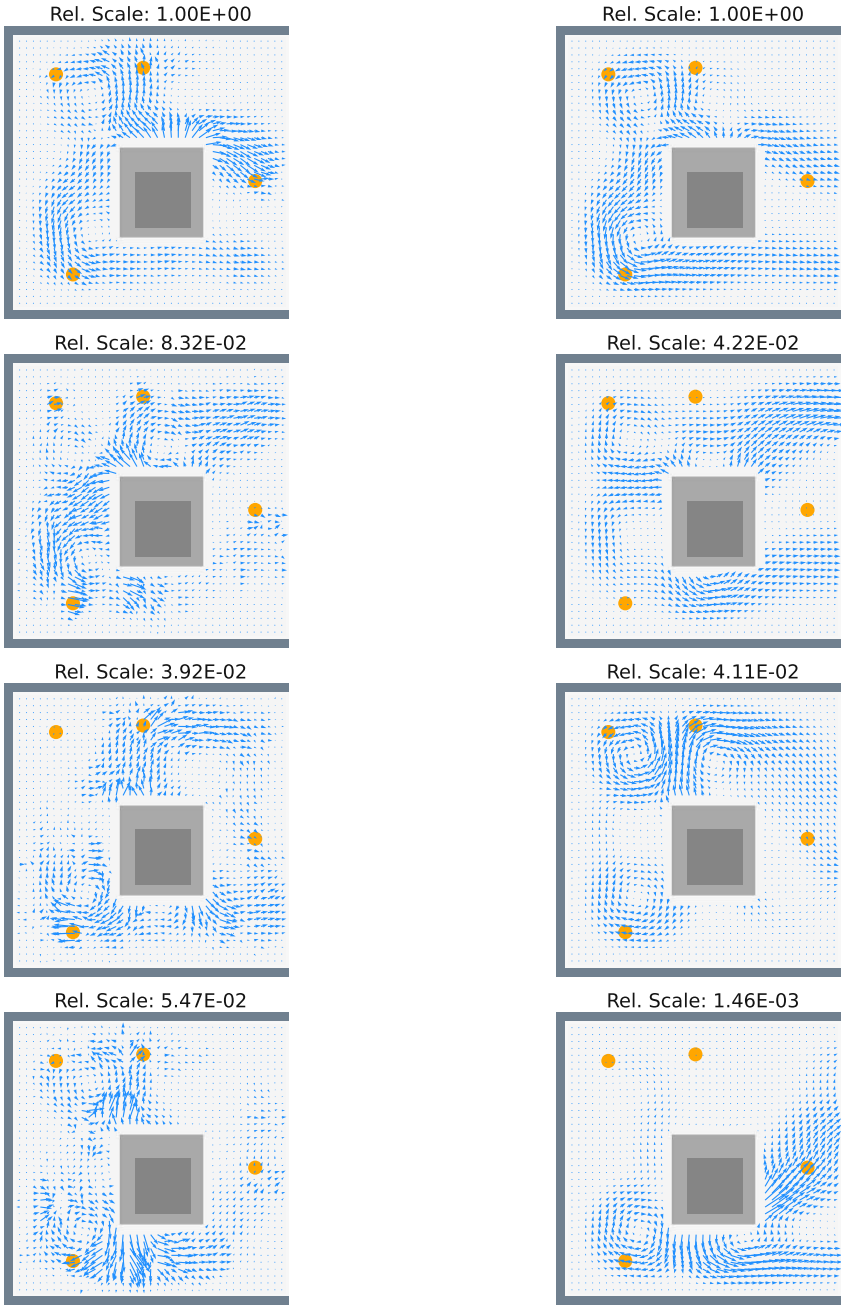

Figure 4.13.: Fisher information flows for $\theta = y_{\text{scat}}$ in the near-field measurement area when injecting the four eigenstates of $\mathbf{F}^y$ at 6.45 GHz. The experimentally measured/simulated flows are shown in (a)/(b) ordered from the largest (top) until the smallest (bottom) corresponding eigenvalue. We depict the Teflon scatterers as orange circles and the metallic target scatterer as a dark gray square. The gray rectangle around the target scatterer corresponds to the region where we could not measure since it is too close to the latter in either the unperturbed or the perturbed system. We denote the relative scales of the vector plots above the figures and do not show the axes ticks/labels to save space.

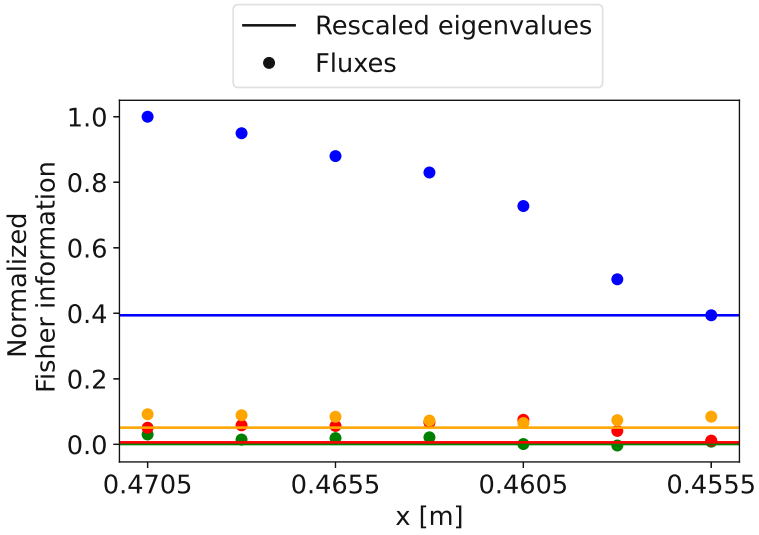

(a)

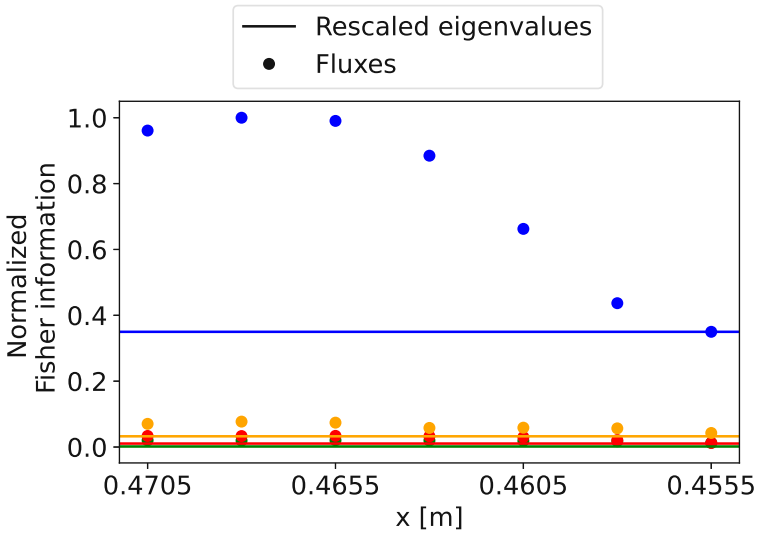

(b)

Figure 4.14.: Comparison of the fluxes $\int_0^{0.1\text{ m}} \mathbf{j}^{x/y}(x,y) \cdot (-\hat{\mathbf{e}}_x) dy$ at different x-positions on the right of the target scatterer to the eigenvalues for $\theta = x_{\text{scat}}$ (a) and $\theta = y_{\text{scat}}$ (b) at $f = 6.45$ GHz. The round markers indicate the measured fluxes, and the solid lines indicate the eigenvalues. Each Fisher information eigenstate is depicted using a different color: the largest eigenstate is shown in blue, the second-largest in yellow, the third-largest in red, and the smallest in green. To account for the relative antenna coupling strength and the norm of the incoming state, we rescale the eigenvalues by a factor α such that the largest flux at the right-most x-coordinate lies on the largest eigenvalue.

5. Conclusion

Recently, information-theoretical concepts were introduced in the field of scattering metrology in the form of the Fisher information operator. This novel quantity, which can be computed solely from far-field measurements, made it possible to quantify the amount of information that a coherent state can extract from an arbitrary complex scattering environment. Moreover, it allowed the identification of the optimal coherent probe state.

In this work, we aimed to understand Fisher information in wave scattering on a more fundamental level by introducing a means to describe its local behavior: the Fisher information flow. We discussed the theoretical framework underlying this quantity and investigated its properties both numerically and experimentally.

First, we derived the Fisher information flow and the corresponding source term for stationary scalar waves and showed that these quantities satisfy the continuity equation. We focused on (quasi-)2D slab geometries to prove that the flow is a local representation of Fisher information. Moreover, we discussed how to control the structure of the flow by tuning the incoming wavefront.

By performing numerical simulations, we then showed where information originates and how electromagnetic waves transport it through a complex scattering environment. We further investigated how global and local loss terms influence the Fisher information flow, implemented the techniques to control its structure, and confirmed that it constitutes an entirely new quantity by comparing it to the Poynting vector. Our numerical analysis validated all theoretical predictions and showed that the Fisher information flow provides a potent and intuitive tool to visualize the complex concept of information.

Finally, we measured the Fisher information flow in a microwave experiment, achieving remarkable precision despite considerable noise effects. Our results show that this quantity is not only of theoretical interest but also constitutes a fundamental feature of electromagnetic waves in practical applications.

All in all, we demonstrated that the Fisher information flow is a valuable complement to the Poynting vector. Since information and energy are equally important concepts in our modern-day world, we hope that the impact of the Fisher information flow will be comparable to the one of the Poynting vector. Future research might investigate the Fisher information flow for vector-valued waves in the time-dependent case to reveal even more of its intriguing properties.

Contributions[1]

The idea for the Fisher information flow came from Stefan Rotter. Jakob Hüpfl provided the theoretical framework with contributions from Lukas Rachbauer. Felix Russo carried out the simulations with input from Jakob Hüpfl, Lukas Rachbauer, and Stefan Rotter. Junjie Lu and Felix Russo performed the experiments under the supervision of Ulrich Kuhl. Felix Russo processed the experimental data with the help of Junjie Lu and under the supervision of Ulrich Kuhl. Felix Russo produced the plots and wrote this manuscript with feedback from Ulrich Kuhl, Lukas Rachbauer, and Stefan Rotter.

[1] All names are listed in alphabetical order.

Acknowledgments[1]

First and foremost, I would like to thank my supervisors Jakob Hüpfl, Ulrich Kuhl, Lukas Rachbauer, and Stefan Rotter, without whom this endeavor would not have been possible. I am especially grateful for all the time you took to discuss with me and for your support, which went beyond anything a master's student could expect.

Many thanks to Junjie Lu, with whom I had the pleasure of collaborating during the experimental part of this work, and to Kevin Pichler, who shared his experience with microwave technology in fruitful discussions.

I would be remiss without mentioning my colleagues Helmut Hörner and Michael Horodynski, who helped me on several occasions this last year.

Furthermore, I am thankful to TU Wien, which enabled me to visit Université Côte d'Azur in Nice by awarding me the KUWI scholarship. Special thanks to Diana Tsenova and Shuhei Yoshida, who provided additional support during the application process.

Moreover, I thank my classmates Nikolaus Becker, Tomas Da Costa, Fulvia Montandon, Alexander Sing, David Weichselbaum, Benjamin Wöckinger, and many others. I hope you will continue to enrich my life with your friendship, wit, and advice.

Words cannot express my gratitude to my mother, father, and little brother, whose emotional support carried me through my studies.

[1] All names are listed in alphabetical order.

Appendix

A. Square Roots of Operators and POVMs

In this section, we review some concepts of linear algebra, functional analysis, and quantum mechanics, which we require in Ch. 2 of this work. Our discussion follows Refs. [23–26].

Definition. *A Hilbert space $\mathcal{H}$ is a complete vector space endorsed with an inner product. Completeness means that every Cauchy sequence in $\mathcal{H}$ converges to an element of $\mathcal{H}$. We use the bra-ket notation and the Riesz representation theorem to denote elements of the Hilbert space $\mathcal{H}$ and its dual space $\mathcal{H}^*$: $|\psi\rangle \in \mathcal{H}$, $\langle\phi| \equiv f_\phi \in \mathcal{H}^*$. Consequently, we write the inner product as $f_\phi(\psi) = (\psi, \phi) =: \langle\phi|\psi\rangle$.*[1]

Definition. *For our purposes, a linear operator (or just operator for short) O is a linear mapping $\mathcal{H} \to \mathcal{H}$, i.e.,*

$$\forall\, |\psi_i\rangle \in \mathcal{H}\ \forall c_i \in \mathbb{C}:\ O\left(\sum_i c_i\, |\psi_i\rangle\right) = \sum_i c_i O\, |\psi_i\rangle\,.$$

Definition. *We call an operator O bounded if*

$$\exists M > 0\ \forall\, |\psi\rangle \in \mathcal{H}:\ \sqrt{\langle O\psi|O\psi\rangle} \leq M\sqrt{\langle\psi|\psi\rangle}.$$

Definition. *The adjoint operator $O^\dagger$ of a bounded operator O is defined via the relation*

$$\forall\, |\psi\rangle\,, |\phi\rangle \in \mathcal{H}:\ \langle\psi|O\phi\rangle = \langle O^\dagger\psi|\phi\rangle\,.$$

If $O^\dagger = O$, we call the operator Hermitian. If $O^\dagger = O$ and the domains of O and $O^\dagger$ are the same, we call the operator self-adjoint. We will not distinguish between the two terms since we only work with operators that map $\mathcal{H} \to \mathcal{H}$. Hermitian operators have real eigenvalues, and the corresponding eigenstates form an orthonormal basis of $\mathcal{H}$.

Definition. *A non-negative operator is a Hermitian operator O that fulfills*

$$\forall\, |\psi\rangle \in \mathcal{H}:\ \langle\psi|O|\psi\rangle \geq 0.$$

[1] Keep in mind that the scalar product in mathematics, which we denote as $(\cdot,\cdot)$, is linear in its first argument, while the scalar product in physics, which we denote as $\langle\cdot|\cdot\rangle$, is linear in its second argument.

Definition. *Let O be non-negative operator on a complex Hilbert space. We call a Hermitian operator A the square root of O if*

$$A^2 = O.$$

Theorem 1. *Every non-negative operator O on a complex Hilbert space has a unique non-negative square root $A \coloneqq \sqrt{O}$. See Ref. [25] for a proof.*

Definition. *The density operator ρ is a non-negative operator that describes any quantum mechanical system, including those in a non-pure state. Consider an ensemble, i.e., a set of pure states $|y\rangle$ that occur with a probability of $w(y)$. We can describe such a system using the following density operator*

$$\rho = \int dy\ w(y)\, |y\rangle \langle y| \,,$$

where

$$\int dy\ w(y) = 1.$$

We can use the density operator to calculate the expectation value of other operators

$$\begin{aligned}
\langle O \rangle &= \int dy\ w(y)\, \langle y|O|y\rangle \\
&= \int dy \int db\ w(y)\, \langle y|O|b\rangle \langle b|y\rangle \\
&= \int db\ \langle b| \int dy\ w(y)\, |y\rangle \langle y|O|b\rangle \\
&= \mathrm{Tr}\left[\rho O\right],
\end{aligned}$$

and it fulfills the normalization condition

$$\begin{aligned}
\mathrm{Tr}\left[\rho\right] &= \int db\ \langle b| \int dy\ w(y)\, |y\rangle \langle y|b\rangle \\
&= \int dy\ w(y) \int db\ \langle y|b\rangle \langle b|y\rangle \\
&= \int dy\ w(y)\, \langle y|y\rangle \\
&= \int dy\ w(y) \\
&= 1,
\end{aligned}$$

where we used an orthonormal basis $\{|b\rangle\}$ of $\mathcal{H}$ in both calculations.

Definition. *One can describe a measurement of a quantum mechanical system by choosing a positive operator-valued measure (POVM), i.e., a set of non-negative operators* $\{\Pi_X\}$ *that sum up to the identity operator:*

$$\int \Pi_X dX = \mathbb{1}.$$

The Born rule gives the probability of observing a measurement outcome X*, i.e.,*

$$p(X) = \mathrm{Tr}\left[\Pi_X \rho\right].$$

A common and simple choice of a POVM is $\Pi_X = |X\rangle\langle X|$*, where* $|X\rangle$ *is the quantum state that corresponds to the measurement outcome* X*.*

B. Far-Field Fisher Information Flow at 6.9 GHz

In this section, we present the far-field measurement of the Fisher information flow at $f = 6.9$ GHz. Figures B.1 and B.2 show the flows corresponding to the eigenstates of $\mathbf{F}^x$ (for $\theta = x_{\mathrm{scat}}$) and $\mathbf{F}^y$ (for $\theta = y_{\mathrm{scat}}$). As for the measurement at $f = 6.45$ GHz, we see that the scale of the vector plots decreases from the largest to the smallest eigenstate. This confirms that the outgoing wavefronts corresponding to the larger eigenvalues carry more Fisher information. Figure B.3 compares the surface integral of the flows to the eigenvalues of the Fisher information operator. We observe an even better agreement than at $f = 6.45$ GHz: the relative deviations are of $\mathcal{O}(2\%)$ for the maximum eigenstates. For the smaller eigenstates, the discrepancies increase due to the smaller signal-to-noise ratio.

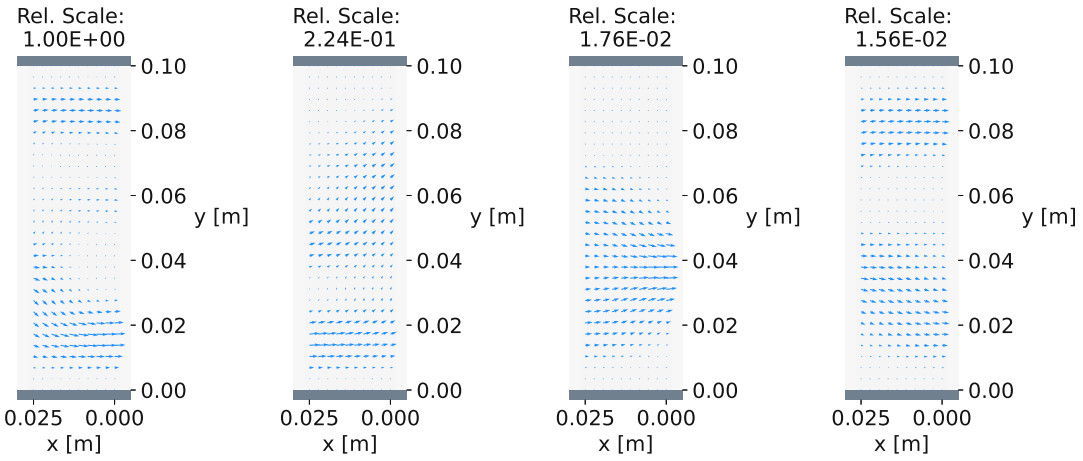

Figure B.1.: Fisher information flows for $\theta = x_{\mathrm{scat}}$ in the far-field measurement area when injecting the four eigenstates of $\mathbf{F}^x$ at 6.9 GHz. We arrange the flows according to the corresponding eigenvalues in decreasing order from left to right. The relative scales of the vector plots are denoted above the figures.

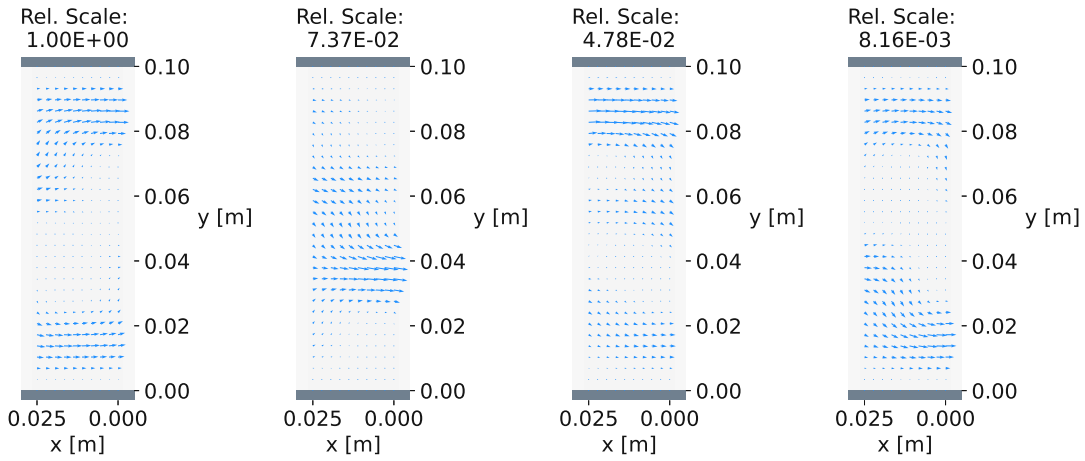

Figure B.2.: Fisher information flows for $\theta = y_{\text{scat}}$ in the far-field measurement area when injecting the four eigenstates of $\mathbf{F}^y$ at 6.9 GHz. We arrange the flows according to the corresponding eigenvalues in decreasing order from left to right. The relative scales of the vector plots are denoted above the figures.

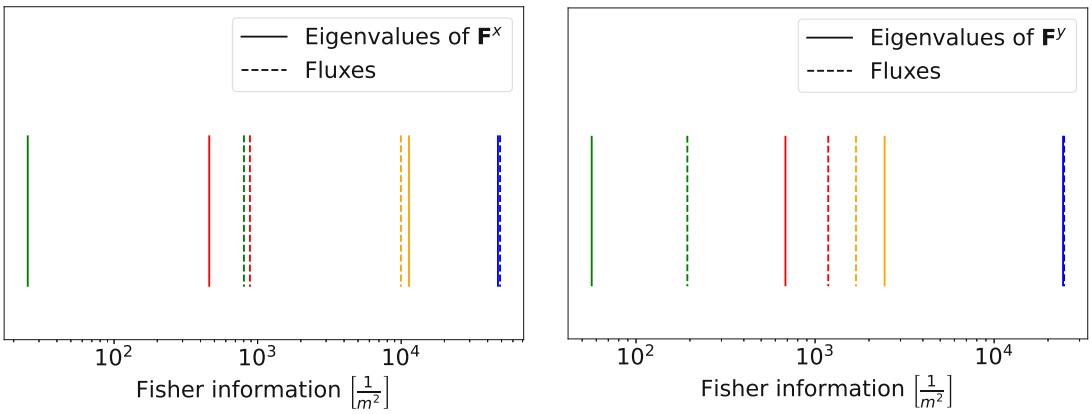

(a) (b)

Figure B.3.: Comparison of the fluxes $\int_0^{0.1\text{ m}} \mathbf{j}^{x/y}(x=0,y)\cdot(-\hat{\mathbf{e}}_x)dy$ to the eigenvalues for $\theta = x_{\text{scat}}$ (a) and $\theta = y_{\text{scat}}$ (b) at $f = 6.9$ GHz. The dotted lines indicate the fluxes, and the solid lines indicate the eigenvalues. Each eigenstate is depicted using a different color: the largest eigenstate is shown in blue, the second-largest in yellow, the third-largest in red, and the smallest in green. Note that we show the Fisher information on a logarithmic x-axis. If there were no experimental uncertainties, the fluxes would be equal to the eigenvalues.

C. Near-Field Fisher Information Flow at 6.9 GHz

In this section, we present the near-field measurement of the Fisher information flow at $f = 6.9$ GHz. Figures C.4a and C.5a show the measured flows when injecting the eigenstates of $\mathbf{F}^x$ (for $\theta = x_{\text{scat}}$) and $\mathbf{F}^y$ (for $\theta = x_{\text{scat}}$) in the near-field measurement area. The corresponding simulated flows are depicted in Figs. C.4b and C.5b. As for the measurement at $f = 6.45$ GHz, we observe that the highest eigenstate features a continuous flow structure that is similar to the simulation. The smaller eigenstates, on the other hand, produce a noisy flow, which deviates from the numerical data.

In Fig. C.6, we compare the experimental eigenvalues to the corresponding fluxes at different x-positions on the right of the target scatterer. Since we do not know the antenna coupling strengths, we rescale the eigenvalues by a factor α such that the largest flux at the right-most x-coordinate lies on the largest eigenvalue. We find $\alpha \approx 1.12 \cdot 10^{-7}$ for the eigenstates of $\mathbf{F}^x$ in Fig. C.6a and $\alpha \approx 1.90 \cdot 10^{-7}$ for the eigenstates of $\mathbf{F}^y$ in Fig. C.6b. In addition to the decrease of the largest flux towards its eigenvalue, which we already saw at $f = 6.45$ GHz, we observe a bump in its curve, which could be a resonance effect due to the change of the waveguide height at $x = 0.453$ m.

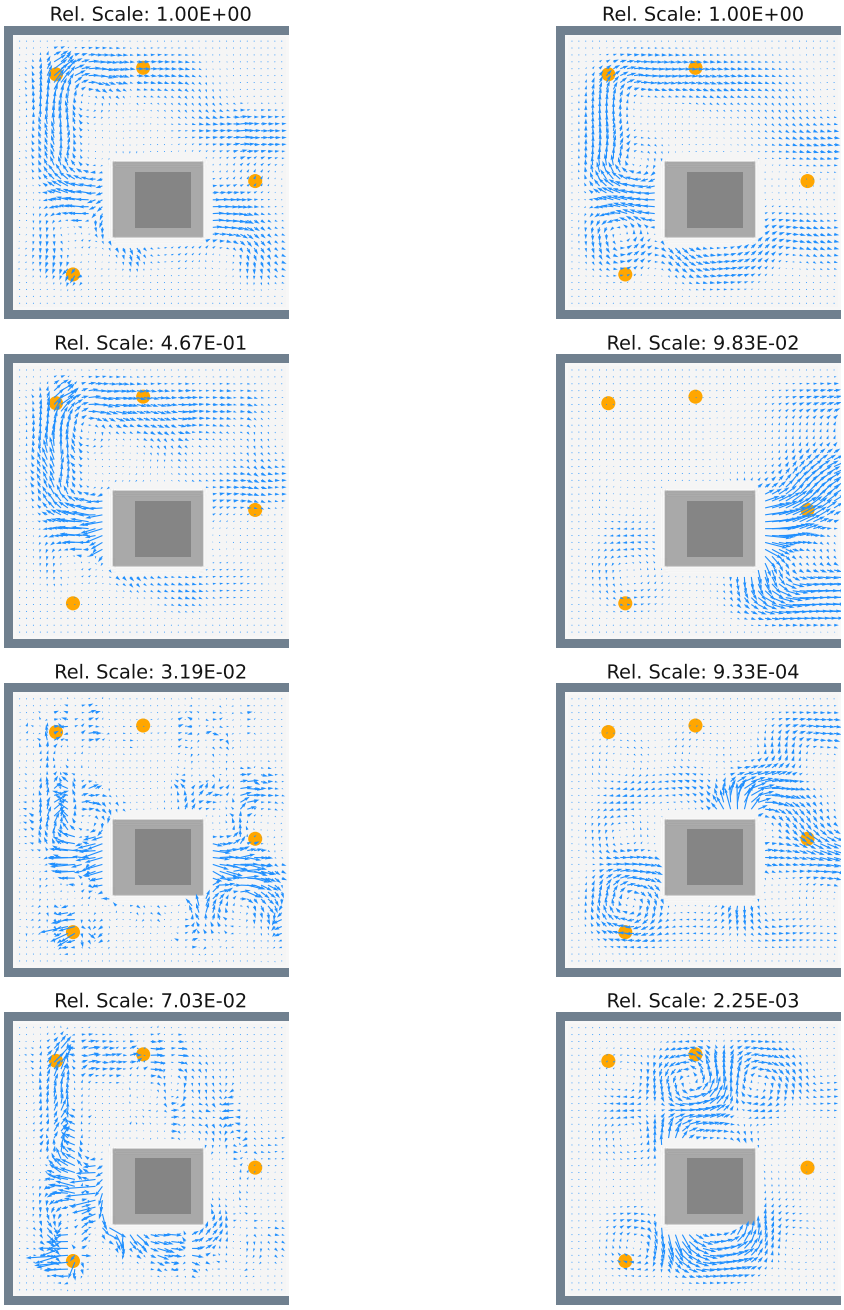

Figure C.4.: Fisher information flows for $\theta = x_{\text{scat}}$ in the near-field measurement area when injecting the four eigenstates of $\mathbf{F}^x$ at 6.9 GHz. The experimentally measured/simulated flows are shown in (a)/(b) ordered from the largest (top) until the smallest (bottom) corresponding eigenvalue. We depict the Teflon scatterers as orange circles and the metallic target scatterer as a dark gray square. The gray rectangle around the target scatterer corresponds to the region where we could not measure since it is too close to the latter in either the unperturbed or the perturbed system. We denote the relative scales of the vector plots above the figures and do not show the axes ticks/labels to save space.

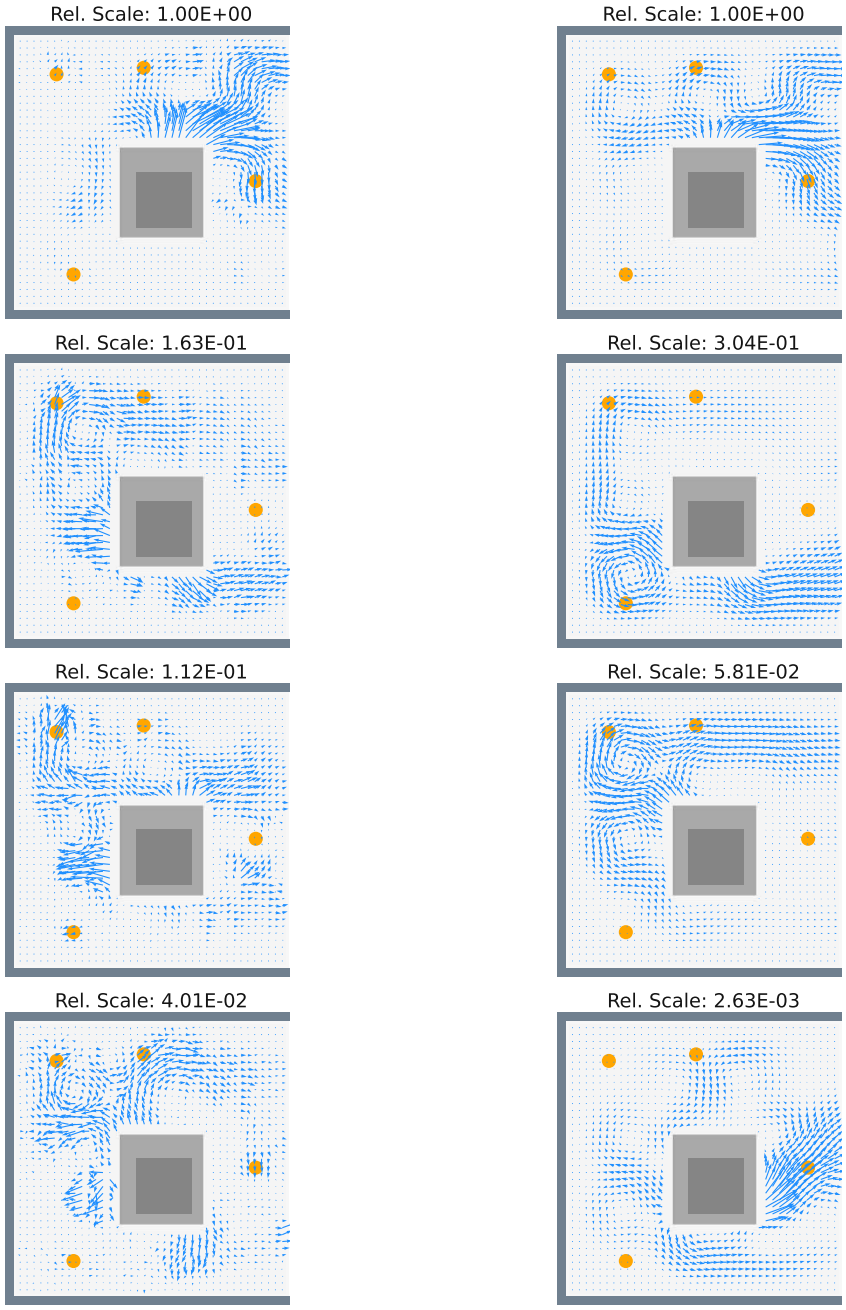

Figure C.5.: Fisher information flows for $\theta = y_{\text{scat}}$ in the near-field measurement area when injecting the four eigenstates of $\mathbf{F}^y$ at 6.9 GHz. The experimentally measured/simulated flows are shown in (a)/(b) ordered from the largest (top) until the smallest (bottom) corresponding eigenvalue. We depict the Teflon scatterers as orange circles, and the metallic target scatterer as a dark gray square. The gray rectangle around the target scatterer corresponds to the region where we could not measure since it is too close to the latter in either the unperturbed or the perturbed system. We denote the relative scales of the vector plots above the figures and do not show the axes ticks/labels to save space.

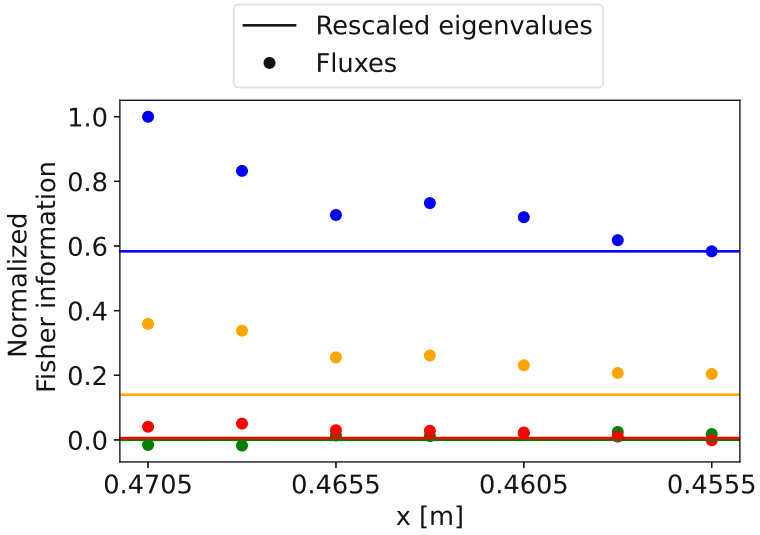

(a)

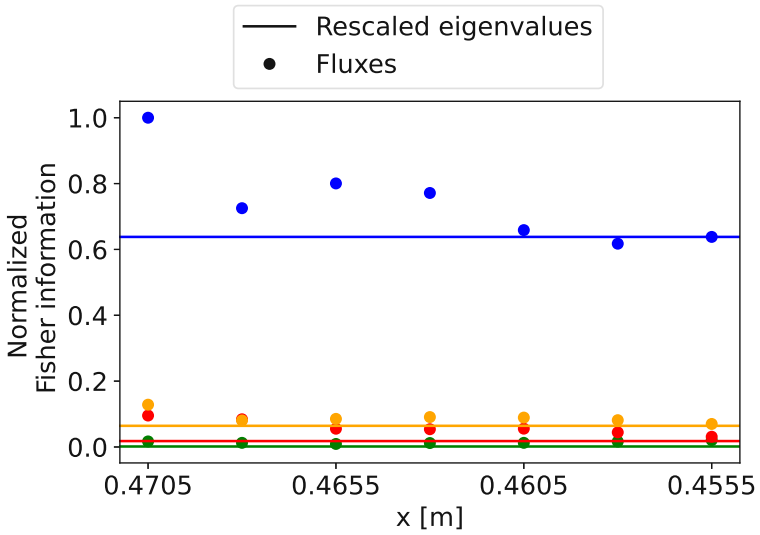

(b)

Figure C.6.: Comparison of the fluxes $\int_0^{0.1\text{ m}} \mathbf{j}^{x/y}(x,y) \cdot (-\hat{\mathbf{e}}_x) dy$ at different x-positions on the right of the target scatterer to the eigenvalues for $\theta = x_{\text{scat}}$ (a) and $\theta = y_{\text{scat}}$ (b) at $f = 6.9$ GHz. The round markers indicate the measured fluxes, and the solid lines indicate the eigenvalues. Each Fisher information eigenstate is depicted using a different color: the largest eigenstate is shown in blue, the second-largest in yellow, the third-largest in red, and the smallest in green. To account for the relative antenna coupling strength and the norm of the incoming state, we rescale the eigenvalues by a factor α such that the largest flux at the right-most x-coordinate lies on the largest eigenvalue.

List of Figures

Bibliography

[1] D. Bouchet, S. Rotter, and A. P. Mosk. *Maximum information states for coherent scattering measurements.* Nature Physics **17**, 564 (2021).

[2] D. Bouchet, L. M. Rachbauer, S. Rotter, A. P. Mosk, and E. Bossy. *Optimal control of coherent light scattering for binary decision problems.* Physical Review Letters **127**, 253902 (2021).

[3] N. G. Orji, M. Badaroglu, B. M. Barnes, C. Beitia, B. D. Bunday, U. Celano, R. J. Kline, M. Neisser, Y. Obeng, and A. Vladar. *Metrology for the next generation of semiconductor devices.* Nature electronics **1**, 532 (2018).

[4] K. A. Brown, S. Brittman, N. Maccaferri, D. Jariwala, and U. Celano. *Machine learning in nanoscience: big data at small scales.* Nano Letters **20**, 2 (2019).

[5] R. W. Taylor and V. Sandoghdar. *Interferometric scattering microscopy: seeing single nanoparticles and molecules via Rayleigh scattering.* Nano letters **19**, 4827 (2019).

[6] Y. Park, C. Depeursinge, and G. Popescu. *Quantitative phase imaging in biomedicine.* Nature photonics **12**, 578 (2018).

[7] M. J. Schervish and M. H. DeGroot. *Probability and statistics.* Pearson Education London, UK: (2014).

[8] M. J. Schervish. *Theory of statistics.* Springer Science & Business Media (2012).

[9] J. P. Santos. *Quantum estimation theory.*

[10] J. Shao. *Mathematical statistics.* Springer Science & Business Media (2003).

[11] M. G. Paris. *Quantum estimation for quantum technology.* International Journal of Quantum Information **7**, 125 (2009).

[12] L. Mandel and E. Wolf. *Optical coherence and quantum optics.* Cambridge university press (1995).

[13] M. Bartelmann, B. Feuerbacher, T. Krüger, D. Lüst, A. Rebhan, and A. Wipf. *Theoretische Physik.* Springer (2015).

[14] J. D. Jackson. *Classical electrodynamics* (1999).

[15] S. Rotter and S. Gigan. *Light fields in complex media: Mesoscopic scattering meets wave control.* Reviews of Modern Physics **89**, 015005 (2017).

[16] W. Lambert, L. A. Cobus, M. Couade, M. Fink, and A. Aubry. *Reflection matrix approach for quantitative imaging of scattering media.* Physical Review X **10**, 021048 (2020).

[17] M. Kühmayer. *Optimal Wave Fields in Complex Scattering Environments.* Ph.D. thesis, TU Wien (2022).

[18] J. Schöberl *et al.* *NGSolve finite element library.* URL: http://sourceforge.net/projects/ngsolve (2019).

[19] A. Taflove, S. C. Hagness, and M. Piket-May. *Computational electromagnetics: the finite-difference time-domain method.* The Electrical Engineering Handbook **3**, 629 (2005).

[20] K. Pichler, M. Kühmayer, J. Böhm, A. Brandstötter, P. Ambichl, U. Kuhl, and S. Rotter. *Random anti-lasing through coherent perfect absorption in a disordered medium.* Nature **567**, 351 (2019).

[21] F. Pedregosa, G. Varoquaux, A. Gramfort, V. Michel, B. Thirion, O. Grisel, M. Blondel, P. Prettenhofer, R. Weiss, V. Dubourg, J. Vanderplas, A. Passos, D. Cournapeau, M. Brucher, M. Perrot, and E. Duchesnay. *Scikit-learn: Machine Learning in Python.* Journal of Machine Learning Research **12**, 2825 (2011).

[22] D. Jalas, A. Petrov, M. Eich, W. Freude, S. Fan, Z. Yu, R. Baets, M. Popović, A. Melloni, J. D. Joannopoulos *et al.* *What is—and what is not—an optical isolator.* Nature Photonics **7**, 579 (2013).

[23] D. J. Griffiths and D. F. Schroeter. *Introduction to quantum mechanics.* Cambridge University Press (2018).

[24] J. J. Sakurai and E. D. Commins. *Modern quantum mechanics, revised edition* (1995).

[25] E. Kreyszig. *Introductory functional analysis with applications*, vol. 17. John Wiley & Sons (1991).

[26] H. E. Brandt. *Positive operator valued measure in quantum information processing.* American Journal of Physics **67**, 434 (1999).